JUSTUS-LIEBIG-
UNIVERSITÄT
GIESSEN

Fachbereich 07 –
Mathematik und Informatik,
Physik, Geographie

Direct Mass Measurements of Neutron-Deficient Lanthanides for Nuclear Structure Studies at the Proton Dripline

Inaugural-Dissertation zur Erlangung des
Doktorgrades der Naturwissenschaftlichen
Fakultät der Justus-Liebig-Universität Gießen

vorgelegt von

Sönke Till Beck

Juni 2023

Erstgutachter: Prof. Dr. Christoph Scheidenberger
Zweitgutachter: Dr. Moritz P. Reiter

Motivation

Since every isotope contains its own characteristic nucleus, the separation of isotopes is very important for nuclear physics. The most complete separation is achieved in the mass spectrograph;
Bethe and Bacher, 1936

Experimental and theoretical studies of exotic nuclei, *i. e.*, very short-lived nuclei far away from the valley of stability in the chart of nuclides, present a unique and important way to gain general understanding of the atomic nucleus and the governing interactions of its constituents. There is an intriguing interplay of strong, weak, and Coulomb interaction, yet the contributions from all fundamental forces (except gravitation) are integrated in the mass of a nucleus. This makes the mass one of its key properties, allowing to study nuclear structure and basic interactions. While the Coulomb force is textbook knowledge and nowadays unified with the weak force in the electroweak interaction, there is no analytical description yet for the strong force, only models covering different aspects in which it manifests. Thus, the path to describe nature from basic interactions is obscured, and data of more exotic nuclei can be used for unraveling different features of the strong force.

Studying exotic nuclei is challenging since they need to be produced first, they are short-lived (many of them have half-lives of only few seconds or even far below), they can only be produced in small quantities, and often the interesting ones are accompanied by a full zoo of other, less exotic and more abundantly produced nuclei. Therefore, powerful separation methods are needed to deal with huge amounts of non-interesting "by-products" and simultaneously obtain reliable results even for the few nuclei of interest. Moreover, the goal to extract information on basic interactions and nuclear structure requires high accuracies despite low statistics.

In this work, the stage is set for pushing the border of the known nuclear landscape. Existing accelerator facilities are used, and existing devices are improved, to reach and study exotic nuclei with high accuracy.

Contents

Chapter 1

Basics of Nuclear Physics and Mass Measurements

1.1 Nuclear Masses and Nuclear Structure

The importance of measuring nuclear masses for investigating nuclear structure and related fields as well as for benchmarking and improving nuclear and mass models will be shortly described. For more details, see *e. g.* the reviews by Lunney *et al.* [2003] and Scheidenberger [2005], a historic overview is given in Audi [2006].

Aston [1920] found that masses of nuclei are multiples of the mass of hydrogen. Later, through more precise measurements, a deviation was found which is nowadays called the mass defect. After Chadwick [1932a,b] discovered the neutron, it became clear that the mass defect reflects the binding energy BE of the nucleus via Einstein's mass–energy equivalence principle:

$$m(Z,N) = Z \cdot m_p + N \cdot m_\mathrm{n} - \mathrm{BE}(Z,N)/c_0^2\,. \tag{1.1}$$

Here and further on, Z and N are the number of protons and neutrons, respectively, m_p and m_n are the masses of the proton and neutron, and c_0 is the speed of light in vacuum. The mass of nuclei hence give access to their binding energies, which can in turn be used to investigate the forces acting in the nucleus. This is a challenging field firstly since the Coulomb, the weak and the strong force are acting inside the nucleus, secondly since the strong force is not entirely understood, and finally since the nucleus is a mesoscopic many-body quantum system. As such it is beyond the reach of a complete analytical or numerical treatment based on individual constituents and can not be fully treated with statistical physics. In response to these challenges, different experimental and theoretical techniques have been developed. On the experimental side for

instance, there is laser spectroscopy to determine charge radii, nuclear deformation via the electric quadrupole moment, and nuclear spins via hyperfine splitting; γ-spectroscopy to investigate nuclear energy levels and isomer excitation energies; scattering experiments to *e. g.* measure single nucleonic wave functions; and mass spectrometry to access all that can be expressed by the binding energy, see below. The impact of mass measurements on understanding nuclear structure dates back about 100 years. For example the pattern in the differences between measured masses of light nuclei and a smooth interpolation of the masses lead to the discovery of shells in nuclei [Elsasser, 1933, 1934; sec. 1.1.1]. Theoretical contributions include different models to investigate all of the above measured quantities and trace them down to microscopic and bulk properties like single particle energies and the deformation energy. These models are usually fitted to known data and needed to get estimates in regions of currently inaccessible nuclei, like for nuclear astrophysics calculations for the rapid neutron capture process [Burbidge *et al.*, 1957]. To get meaningful results from derived quantities, *i. e.* with realistic error estimates, once fitted models need to be tested with new data, especially data far from the nuclei where the model parameters have been fitted [Dedes and Dudek, 2019]. Much focus is put on measuring masses of exotic nuclei, which are short-lived, far from the valley of stability in the chart of nuclides —interpolated by the line of β-stability (Fig. 1.1) towards which they will eventually decay—, *i. e.* they have an unusual proton to neutron ratio, and they usually do not exist on Earth. In consequence, they need to be produced artificially (sec. 1.3). As a rule of thumb, nuclei farther away from the line of β-stability are harder to produce, with yields dropping exponentially with exoticity[1]. The interest in exotic nuclei is both about improving of nuclear models, and to investigate new effects which may arise there. Moreover, while exotic nuclei do not exist on Earth, they are produced in stellar environments, and thus their masses are a key to understand element abundances in the Solar System.

1.1.1 Nuclear and Mass Models

One of the earliest successful attempts to describe the binding energies and thus the masses of nuclei is the liquid drop model of Gamow [Gamow, 1930], put into an analytical form by the Bethe-Weizsäcker mass formula [Bethe and Bacher, 1936; von Weizäcker, 1935]. The liquid drop model was good at predicting the average trend of binding energies and for fission studies. It could not explain increased binding energies at some nucleon numbers and increased amount of stable isotopes or isotones at certain proton or neutron numbers, which were

[1] We use the term "exoticity" as a measure of the distance from the line of β-stability.

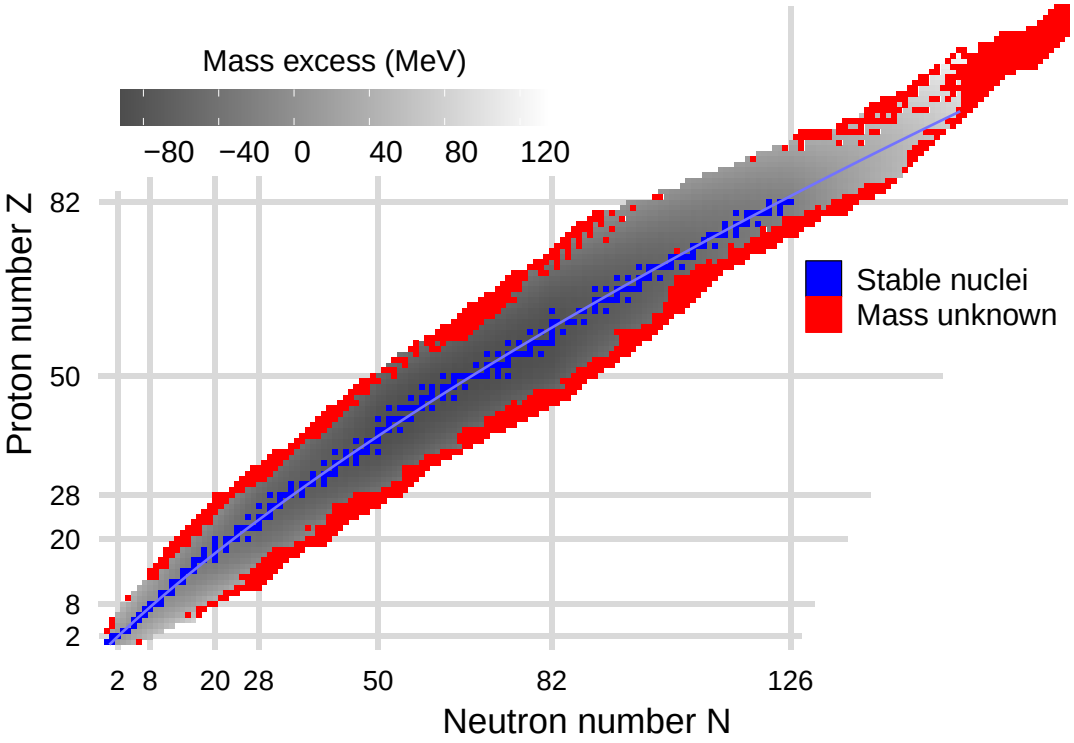

Figure 1.1: The chart of nuclides with stable nuclei colored in blue, nuclei with unknown masses in red and all other nuclei according to their mass excess [Wang *et al.*, 2021]. The light blue line is a parametrization of the line of β-stability [Kodama, 1971].

observed [Elsasser, 1933, 1934; Mayer, 1948]. These experimental findings concentrated the interest there and led to the nuclear shell model, studying the nucleons using a single particle Hamiltonian $\hat{\mathcal{H}}_{\text{shell model}}$. It explained the stronger binding by closed shells, similar to the electronic configurations in atoms where noble gases are much less likely to chemically react and harder to ionize. The nucleon numbers where this effect was observed were termed 'magic' – at that time the liquid drop model was favored and it was surprising that shell effects could arise without a central potential like it is given by the atom's core for electrons. Magic numbers for a kind of nucleons occur where the respective orbitals are filled and there is a comparatively large energy gap to the next orbital. Nuclei with magic neutron- and proton-number are called doubly-magic. Predictions from the shell model could be matched to experimental observations first in light and later also in medium heavy nuclei once it was recognized that there is strong spin-orbit coupling [Haxel *et al.*, 1949; Mayer, 1949]. For a nucleus composed of nucleons index by i, the shell model Hamiltonian can be

written

$$\hat{\mathcal{H}}_{\text{shell model}} = \sum_i \left(\hat{\mathcal{T}}_i + \hat{\mathcal{V}}_i + \hat{\mathcal{V}}_{LS;i} \vec{L}_i \cdot \vec{S}_i \right), \tag{1.2}$$

with the single particle kinetic energies $\hat{\mathcal{T}}_i$, central potential $\hat{\mathcal{V}}_i$, and the spin-orbit potential $\hat{\mathcal{V}}_{LS;i}$. Compared to the full Hamiltonian of the nuclear many-body system, a residual interaction is missing. The shell model yields more realistic predictions when the residual interactions is small, which for instance holds for nuclei neighboring doubly-magic nuclei.

Besides *ab initio* approaches aiming to describe properties of nuclei from interactions reconstructed from nuclei with two or three nucleons, nuclear mass models can be coarsely classified in purely microscopic and macroscopic-microscopic models. The former calculate the binding energy from single particle effective interactions [*e. g.* Goriely *et al.*, 2010], while the latter employ a macroscopic model for the smooth trend E_{macro} and a means to calculate the microscopic, *i. e.*, shell- and pairing-corrections ΔE_{shell} and $\Delta E_{\text{pairing}}$[*e. g.* Möller *et al.*, 2016]. The total nuclear energy in macroscopic-microscopic models is

$$E = E_{\text{macro}} + \Delta E_{\text{shell}} + \Delta E_{\text{pairing}} \,. \tag{1.3}$$

All contributions to the total nuclear energy –macroscopic and microscopic– depend on the nucleon numbers N and Z, the macroscopic energy and the shell-correction depend on the shape of the nucleus as well. The microscopic contributions are calculated independently for protons and neutrons.

For the shell-correction, the Strutinsky method [Strutinsky, 1967] is widely used. Here an average potential acting on the single particles, given by the nuclear mean field, is assumed and single particle energies are calculated according to this model. The terms nuclear mean field and average potential are somewhat equivalent in that they define each other. Describing the dynamics as single particles in the mean field is neglecting two-body interactions, which is a sound approach if the mean free path is much longer than the diameter of the nucleus, which in turn is estimated to be valid up to about 10 MeV per nucleon [Negele, 1982]. Then the shell-correction ΔE_{shell} is calculated subtracting from the sum of single particle energies $\varepsilon_i^{\text{s. p.}}$ in that mean potential the smoothed out single particle energies obtained using a smoothing function f and a smoothing width γ on the order of distance between shells, $\gamma \sim \hbar\omega$ [see *e. g.* review article Brack *et al.*, 1972].

$$\Delta E_{\text{shell}} = \sum_i n_i \varepsilon_i^{\text{s. p.}} - \int_{-\infty}^{\tilde{\lambda}} \sum_i n_i E f\left(\tfrac{E-\varepsilon_i^{\text{s. p.}}}{\gamma}\right) \mathrm{d}E \,. \tag{1.4}$$

The n_i are occupation numbers of the level with energy $\varepsilon_i^{\text{s. p.}}$, for non-degenerate levels $n_i \in \{1, 2\}$. For the smoothing function as a standard choice a Gaussian,

$f(x) = \exp(-x^2/2)/\sqrt{2\pi}$ may be used. $\tilde{\lambda}$ is the Fermi energy, determined from particle number conservation,

$$\int_{-\infty}^{\tilde{\lambda}} \sum_i n_i f\left(\tfrac{E-\varepsilon_i^{\text{s. p.}}}{\gamma}\right) \mathrm{d}E = \sum_i n_i \,. \tag{1.5}$$

The shell correction has to be calculated for both protons and neutrons. The latter part in (1.4), varying slow in nucleon numbers, is assumed to be already part of the macroscopic model. The mean field corresponds to the central potential and spin-orbit parts of a Hamiltonian of the form given in eq. (1.2).

For the pairing correction, a similar approach as for the shell correction can be used: Pairing correlation energies, *i. e.* energy differences between paired and unpaired configurations, are calculated once for a nucleus with (sharp) single particle levels in a mean field potential and once for a smoothed out level density. The difference of the respective values E_{pc} and $\overline{E_{\text{pc}}}$ is then used as pairing correction. In contrast to the shell-corrections, now the Hamiltonian given in eq. (1.2) is not sufficient, since the pairing correlations arise from two-body interactions, *i. e.*, from residual interactions. In the framework of pairing-correlations, the operator representing the residual interactions is usually denoted $\hat{\mathcal{G}}$. For calculating the pairing correlations, the Bardeen–Cooper–Schrieffer (BCS) approximation can be used. The following outline follows [Ogle *et al.*, 1971; Bolsterli *et al.*, 1972]. The BCS wavefunction is

$$|\psi^{\text{BCS}}\rangle = \prod_k (u_k + s v_k a^\dagger_{sk} a^\dagger_{-sk})|0\rangle \,. \tag{1.6}$$

Here the parameter $s \in \{\pm 1\}$ indicates time-reversal of orbits with otherwise same quantum numbers, k is the label of the single-particle level and $a^\dagger_{\pm sk}$ are creation operators for the nucleon in that level, possibly on a time-reversed orbit. u_k and v_k are amplitudes, v_k^2 is thus the probability to find the two orbitals $\pm sk$ occupied. The pairing correlation is then

$$E_{\text{pc}} = \underbrace{\sum_{k=1}^{N_{\text{pairs}}} \left(2\varepsilon_k^{\text{s. p.}} v_k^2 - G v_k^4\right) - \frac{\Delta^2}{G}}_{\text{BCS energy “paired”}} - \underbrace{\sum_{k=1}^{N_{\text{pairs}}/2} \left(2\varepsilon_k^{\text{s. p.}} - G\right)}_{\text{“unpaired” } \Delta=0} \,. \tag{1.7}$$

N_{pairs} is the number of pairs considered, usually half of the pairs are located below and above the Fermi energy, respectively. The pairing strength G is the matrix element of the residual interaction operator $\hat{\mathcal{G}}$ responsible for pairing,

$$G = \sum_{s,s'} \langle s'k', -s', k'|\hat{\mathcal{G}}|sk, -sk\rangle \,, \tag{1.8}$$

and Δ is the correlation parameter or pairing gap,

$$\Delta = G \sum_k u_k v_k \,. \tag{1.9}$$

The single particle pairing correlation energy E_{pc} and its smoothed-out counterpart $\overline{E_{\mathrm{pc}}}$ are calculated by solving a set of nonlinear equations involving sums over the single particle energies or integrals over the smooth level distribution, respectively. For the smoothed-out pairing correlation energy $\overline{E_{\mathrm{pc}}}$, the respective pairing gap $\overline{\Delta}$ is obtained from experimental data, see below.

The so-defined microscopic corrections approximate the difference between the macroscopic model and the real binding energy including quantum effects. Macroscopic models are usually improvements of the liquid drop model. The mean field can have different forms with parameters fitted to experimental data, like the folded Yukawa potential used by Möller *et al.* [2016] or the Woods-Saxon (WS) potential used *e. g.* by Dudek and Werner [1978a]; Dudek *et al.* [1979a, 1980a].

1.1.2 Nuclear Structure Effects and Nuclear Masses

The nuclear binding energy is one of the key properties of the nucleus. With the binding energies, isomer excitation energies, particle separation energies, proton-neutron interaction strengths and more quantities can be calculated, which contribute to understanding the nucleus.

Isomer excitation E_{exc} energies are the differences of the isomeric and the ground state (i.s., g.s.) binding energies,

$$E_{\mathrm{exc}} = \mathrm{BE}(N, Z, J^{\pi}_{\mathrm{i.s.}}) - \mathrm{BE}(N, Z, J^{\pi}_{\mathrm{g.s.}}) \,. \tag{1.10}$$

Here the different states were indicated by different spin-parity J^{π}. For longer lived isomers and isomers where the internal transition (IT) ratio is small, a mass measurement may be the only feasible way to derive the excitation energy.

Particle separation energies involve binding energies of ground states of a nucleus and its neighbors. Quantities involving ground state binding energies of several distinct nuclei are also called mass filters, a few which will be used in this work shall be introduced here. The one- and two-neutron separation energies, S_{n} and $S_{2\mathrm{n}}$, are defined as

$$S_{\mathrm{n}}(N, Z) = \mathrm{BE}(N, Z) - \mathrm{BE}(N-1, Z) \,, \tag{1.11}$$

$$S_{2\mathrm{n}}(N, Z) = \mathrm{BE}(N, Z) - \mathrm{BE}(N-2, Z) \,. \tag{1.12}$$

From pure bulk-property models like the liquid-drop model, these are expected to steadily decrease with increasing neutron number, modulated by an odd-even staggering due to pairing contributions in case of S_{n}. Any deviation from

this behavior has to be due to microscopic, *i. e.* quantum effects. Figure 1.2 shows these mass filters for tin isotopes. The most striking feature in $S_{2\mathrm{n}}$ is the steep decrease at $N = 50$ and $N = 82$, two nuclear shell closures. To quantify this decrease, often the empirical two-neutron-shell gap,

$$\begin{aligned}\Delta_{2n}(Z,N) &= S_{2\mathrm{n}}(N,Z) - S_{2\mathrm{n}}(N+2,Z) \\ &= 2\,\mathrm{BE}(Z,N) - \mathrm{BE}(Z,N-2) - \mathrm{BE}(Z,N+2)\,.\end{aligned} \tag{1.13}$$

is used. While the two-neutron separation energy shows steep decreases at closed shells, the two-neutron-shell gap shows pronounced maxima *vs* the neutron number N, when crossing closed shells. Nuclei are unbound with respect to particle emission if the respective separation energy is negative, the boundary between bound and unbound nuclei is called (one-)neutron or (one-)proton drip line in the case of neutron- and proton-unbound nuclei, respectively. Similarly, the two-neutron and two-proton drip lines are defined as the boundary between nuclei with positive and nuclei with negative two-neutron or two-proton separation energy. The data in Fig. 1.2 shows how systematic mass measurements can be used to find unbound nuclei and investigate pairing energies via the odd-even staggering of $S_{1\mathrm{n}}$ encoded in $|\Delta_{1n}|$ with

$$\begin{aligned}\Delta_{1n}(Z,N) &= S_{1\mathrm{n}}(N,Z) - S_{1\mathrm{n}}(N+1,Z) \\ &= 2\,\mathrm{BE}(Z,N) - \mathrm{BE}(Z,N-1) - \mathrm{BE}(Z,N+1)\end{aligned} \tag{1.14}$$

and shell gaps as differences of $S_{2\mathrm{n}}$ values. For proton separation energies, analog quantities S_{p}, $S_{2\mathrm{p}}$, and so on, are defined by subtracting binding energies with different proton numbers.

$$S_{\mathrm{p}}(N,Z) = \mathrm{BE}(N,Z) - \mathrm{BE}(N,Z-1)\,, \tag{1.15}$$

$$S_{2\mathrm{p}}(N,Z) = \mathrm{BE}(N,Z) - \mathrm{BE}(N,Z-2)\,, \tag{1.16}$$

$$\begin{aligned}\Delta_{2p}(Z,N) &= S_{2\mathrm{p}}(N,Z) - S_{2\mathrm{p}}(N,Z+2) \\ &= 2\,\mathrm{BE}(Z,N) - \mathrm{BE}(Z-2,N) - \mathrm{BE}(Z+2,N)\,.\end{aligned} \tag{1.17}$$

$$\begin{aligned}\Delta_{1p}(Z,N) &= S_{1\mathrm{p}}(N,Z) - S_{1\mathrm{p}}(N,Z+1) \\ &= 2\,\mathrm{BE}(Z,N) - \mathrm{BE}(Z-1,N) - \mathrm{BE}(Z+1,N)\,.\end{aligned} \tag{1.18}$$

Absolute values of Δ_{1n} and Δ_{1p} can be used to determine the pairing gap in the smoothed-out pairing correlation energy.

Mass filters do not need to involve only binding energies with the same number of protons or neutrons. A notable mass filter using binding energies of

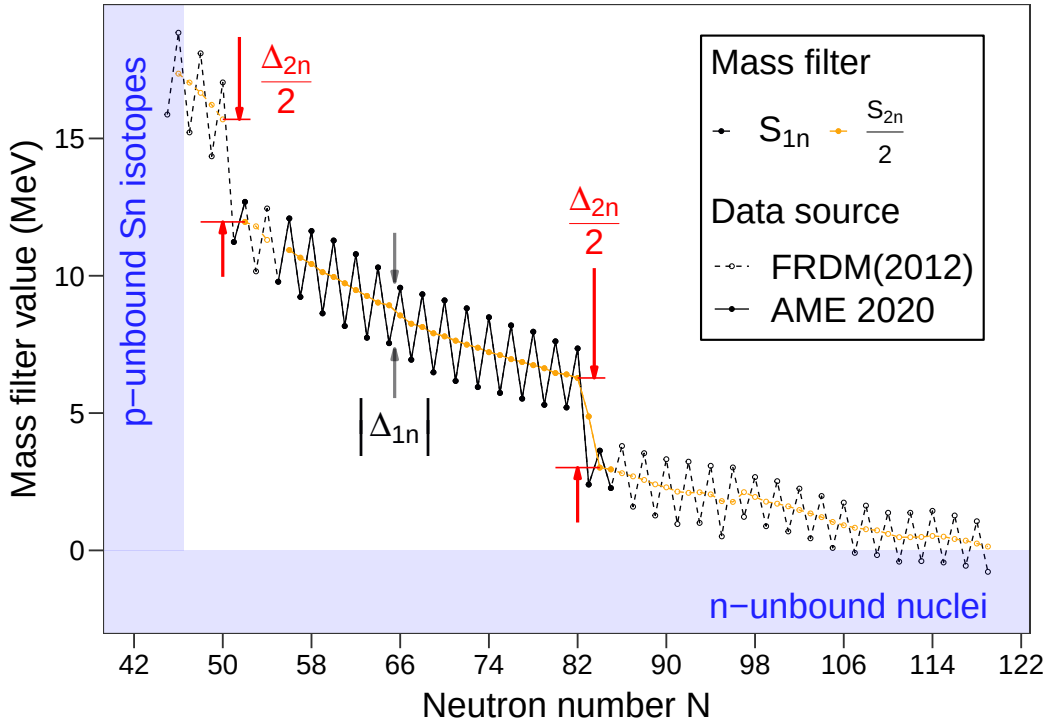

Figure 1.2: Neutron and scaled two-neutron separation energies of tin isotopes, experimental data [Wang *et al.*, 2021] and FRDM (2012) predictions [Möller *et al.*, 2016]. The predictions are only plotted where no experimental data are available. The region of proton-unbound Sn isotopes can not be read from the shown data but were obtained from proton and two-proton separation energies with FRDM(2012) values. For details on the revealed nuclear structure properties see text.

four nuclei with different proton and neutron numbers is δV_{pn}, defined by

$$\begin{aligned}\delta V_{\mathrm{pn}}(Z,N) &= S_{\mathrm{n}}(N,Z) - S_{\mathrm{n}}(N,Z-1) \\ &= S_{\mathrm{p}}(N,Z) - S_{\mathrm{p}}(N-1,Z) \\ &= \Big[\mathrm{BE}(N,Z) - \mathrm{BE}(N-1,Z)\Big] - \\ &\quad \Big[\mathrm{BE}(N,Z-1) - \mathrm{BE}(N-1,Z-1)\Big]\,.\end{aligned} \tag{1.19}$$

This quantity is a measure for the interaction strength of the last valence nucleon in a nucleus.

1.1.3 Nuclear Deformation

Nuclear deformations alter the binding energies through the different contributing terms, both macroscopic and microscopic. A macroscopic contribution is the change in Coulomb energy with deformation, microscopic contributions are rooted in the re-ordering of nuclear levels, which is changing the shell correction. The deformation can be expressed quantitatively by describing the nucleus' surface Σ, defined as the manifold $R = R(\vartheta, \varphi)$ where the nuclear density is 50% of its maximum. For a spherical nucleus, R does not depend on the angles, *i. e.* $R = R_0$. The angular dependence can be expanded in terms of spherical harmonics $Y_{\lambda,\mu}(\vartheta, \varphi)$ (Fig. 1.3 for some visualizations), since they form a complete set of orthonormal functions on the unit sphere $\{(\vartheta, \varphi) : 0 < \vartheta < \pi, 0 < \varphi < 2\pi\}$:

$$R(\vartheta,\varphi) = R_0\left(1 + \sum_{\lambda,\mu>0} \alpha_{\lambda,\mu} Y_{\lambda,\mu}(\vartheta,\varphi)\right). \tag{1.20}$$

Terms with $\lambda = 2$ are associated with general quadrupole deformations. α_{20} is the conventional quadrupole deformation parameter for axially symmetric deformation, often denoted as β [Neugart and Neyens, 2006].

Nuclear deformations can be quantified experimentally by measuring the electric quadrupole moment via hyperfine structure splitting using laser spectroscopic methods or from moments of inertia determined by γ-spectroscopy. In the neutron rich region around $A = 100$, there are isotopes for which the two-neutron separation energy is increasing with the neutron number [Wang *et al.*, 2021]. This can neither be explained by macroscopic trends for spherical shapes nor by shell effects, since both imply a reduction of $S_{2\mathrm{n}}$ with increasing neutron number. Here, the behavior is explained by nuclear deformation, experimentally observed, *e. g.*, by Thibault *et al.* [1981] using high resolution laser spectroscopic methods. The added neutrons change the ground state

shape such that they become stronger bound and increase the separation energy. Mass measurements thus also open a way to search for deformed nuclei, through similar patterns of separation energies as observed for S_{2n} in regions of known non-spherical ground states.

1.2 Masses of Exotic Nuclei

As previously mentioned, much interest is concentrated in exotic nuclei, far from the line of β-stability. Exotic nuclei reveal novel properties, unknown in more stable nuclei, such as nuclear halos and skins [Riisager, 1994], and exotic decay modes [Pfützner *et al.*, 2012] like two-proton decay. Since even nuclei are stronger bound than odd nuclei, the one-proton drip line is reached earlier than the two-proton drip line. However, in some even-Z nuclei the one-proton decay is energetically forbidden, while the two-proton decay is allowed. The location of the one- and two-proton drip lines is known up to $Z = 91$ with an uncertainty of about two neutrons above xenon ($Z = 54$) [Erler *et al.*, 2012; Neufcourt *et al.*, 2020]. Since the emission of a charged particle is hindered by the Coulomb barrier, direct observation can be challenging and mass measurements are needed to find energetically possible candidates for studying these decays. This can also be extended by indirect determination of masses: In the $A \gtrsim 150$ region, several α-decay chains are located above the $N = 82$ shell

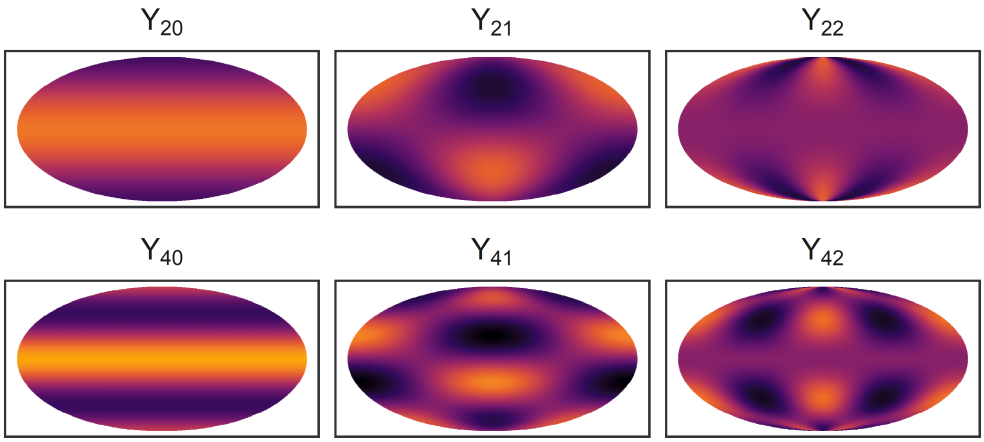

Figure 1.3: Values of some spherical harmonics projected from the sphere to a flat surface in color code for visualization. Values with negative μ, *e. g.* $Y_{2,-1}$ and $Y_{2,-2}$, are obtained by rotating by a quarter period (like exchanging a sine and cosine with fixed argument) in the 'east-west' direction. Higher order μ plots for $\lambda = 4$ will have more oscillations in the 'east-west' direction.

closure, close to the proton drip line. The last nucleus in these chains is on the $N = 82$ shell or one neutron above. High accuracy mass measurements of these anchors can decrease the mass uncertainty of all nuclei in the decay chain, or even determine their masses, when no mass in the chain was known before. This allows more accurate prediction of two-proton decaying nuclei.

Another striking effect, which may occur in exotic nuclei, is a change in the nuclear shell structure towards the proton or neutron drip lines; shells can weaken or disappear, and new shell closures can appear [Sorlin and Porquet, 2008; Kanungo, 2013]. On the neutron-rich side of the nuclear chart, shell closures have been shown to vanish far from stability for the neutron numbers $N = 20$ and $N = 28$ [Thibault *et al.*, 1975; Sarazin *et al.*, 2000], and new shell closures have been found for $N = 32$ and $N = 34$ [Gallant *et al.*, 2012; Wienholtz *et al.*, 2013; Rosenbusch *et al.*, 2015; Xu *et al.*, 2015; Leistenschneider *et al.*, 2018; Steppenbeck *et al.*, 2013; Michimasa *et al.*, 2018; Leistenschneider *et al.*, 2021]. The $N = 82$ shell closure has been studied from neutron deficient ${}_{68}$Er to neutron-rich ${}_{48}$Cd [Manea *et al.*, 2020].

Series of nuclear isomers are known to occur near shell closures [Jain *et al.*, 2021]. A unique sequence of isomers exists in the odd $N = 81$ isotones, ranging from ${}^{131}_{50}$Sn to ${}^{149}_{68}$Er [Kondev *et al.*, 2021; ENSDF]. These isomers have spin and parity $J^\pi = {}^{11}/_{2}^{-}$ and the respective ground states change from $J^\pi = {}^{3}/_{2}^{+}$ to $J^\pi = {}^{1}/_{2}^{+}$ between ${}^{143}_{62}$Sm and ${}^{145}_{64}$Gd. In ${}^{129}_{48}$Er, the ground and isomeric states are inverted, *i. e.* the ground state has $J^\pi = {}^{11}/_{2}^{-}$ and the isomeric state $J^\pi = {}^{3}/_{2}^{+}$ [Manea *et al.*, 2020]. The series is unique in the sense that the isomeric excitation energies stay approximately constant between ${}^{139}_{58}$Ce and ${}^{149}_{68}$Er, over a range of eleven isotones. Measuring masses of nuclear ground and isomeric states far from stability gives access to the evolution of the isomeric excitation energies.

1.3 Production of Exotic Nuclei

Exotic nuclei decay towards the line of β-stability (Fig. 1.1) and thus they are naturally existing on Earth only in the long-lived case or when produced from decay of long-lived radionuclides, like ${}^{238}_{92}$U. Yet there is strong interest in these nuclides from basic research to application, *i. e.* radionuclides used for medical purposes. Exotic nuclei are produced through nuclear reactions. Spontaneous fission of long-lived radionuclides, like the before-mentioned ${}^{238}_{92}$U, yields certain neutron-rich exotic nuclei. In accelerator laboratories, production of exotic nuclei is achieved mainly by the two types termed Isotope-Separation On-Line (ISOL) and In-Flight separation, which will be described briefly in the following. Techniques not described here include the IGISOL technique, fusion,

neutron capture in nuclear reactors, or similar.

In-flight separation usually uses a heavy beam at relativistic energy impinging on a light element target. The production mechanisms are mainly fragmentation and Coulomb- and abrasion-fission of the projectile. Primary beam and reaction products loose energy but still leave the target with relativistic energy and are separated afterwards. There is no element-dependency and highly clean beams are possible, down to a single isotope. Due to the relativistic velocities, shortest half-lives are accessible with the In-Flight method.

ISOL usually uses a proton beam impinging on a heavy element target. The production mechanisms are spallation and fission of the target nuclei. The reaction products are stopped in the target and have to diffuse through and effuse out of it. They may need to be ionized, introducing a strong element dependency in the method. Accessible ions are limited in their half-life by the diffusion and effusion time which depends on the actual target geometry and temperature, and the chemistry of target and product. The ions are then re-accelerated to energies typically several 10 keV or up to a few MeV/u in case so-called post-accelerators are used. The re-accelerated beam is separated according to the mass-to-charge ratio. The term "on-line" signifies the simultaneous operation of production and separation. ISOL usually gives high rates, but also high isobaric contamination depending on chemical properties of elements in the region, especially species with lower ionization potentials are coming out of the target being surface ionized while for instance refractory elements are hard or impossible to even leave the target in any state.

To face the challenge of isobaric contaminants at ISOL facilities, isobar separators have so far been realized as large double-stage magnetic separators [Wollnik and Becker, 1985] or Penning traps [Savard *et al.*, 1991]. The mass resolving power of magnetic separators is typically not sufficient to cleanly resolve nuclear isobars, and Penning traps are limited because of their cycle time and ion capacity, which are on the order of one second and 1000 ions per cycle, respectively. Recently, MR-TOF mass spectrometers [Wollnik and Przewloka, 1990; Plaß *et al.*, 2013b] have been established as isobar separators [Plaß *et al.*, 2008; Wolf *et al.*, 2013a; Hirsh *et al.*, 2016], also offering additional benefits (sec. 1.4.1 below and chapter 4). An MR-TOF-MS has been used in the present work for improved tuning of the upstream ISOL beamline and ion source, separation of the isobaric beam in the cases where the magnetic separator was not sufficient, and subsequent mass measurements.

1.3.1 In-flight Separation at GSI: The FRS

At the GSI Helmholtzzentrum für Schwerionenforschung GmbH (GSI), the Universal Linear Accelerator (UNLIAC), the Schwerionensynchrotron SIS18 (SIS)

and the Fragment Separator (FRS) [GSI Helmholtzzentrum für Schwerionenforschung, 2021; Geissel *et al.*, 1992] combine to an In-flight facility. The UNILAC can deliver all ions up to uranium with energies up to 11.4 MeV/u as bunched beam. The bunches are injected into the SIS, and accelerated up relativistic speeds, ∼90% speed of light, *e. g.* 1 GeV/u for uranium. Intensities for uranium are up to $\gtrsim 2 \times 10^9$/spill. The ions at relativistic speeds are extracted from the SIS towards the FRS, where they impinge on a target for the creation of a relativistic secondary beam. This beam can be separated using the $B\rho$–ΔE–$B\rho$ method and slits at the focal planes such that several nuclei or even only a single isotope is delivered to the final focal plane for experiments [Geissel *et al.*, 1992].

Currently the new underground ring accelerator SIS100 and the new super fragment separator (Super-FRS) and more experimental and storage rings are constructed at the Facility for Antiproton and Ion Research (FAIR), extending the existing GSI facilities (Fig. 1.4). SIS100 will be using ion bunches from SIS18 and accelerate them up to ∼99% speed of light. The Super-FRS has two separator stages and higher acceptances than the existing FRS. It delivers the separated beam to different experiments. In the present work, developments have been done at the FRS ion catcher (FRS-IC), which slows down and stops the relativistic beam delivered by the FRS. (see chapter 2). These developments also serve for the experiments planned at the Super-FRS.

1.3.2 ISOL at TRIUMF: ISAC

At the Tri University Meson Factory (TRIUMF), a cyclotron and the Isotope Separator and Accelerator (ISAC) [Dombsky *et al.*, 2000; Dilling *et al.*, 2014] beamline form an ISOL facility. In the TRIUMF cyclotron [Bylinskii and Craddock, 2014], H^- ions are accelerated to 480 MeV, and the electrons are removed with stripper foils for extracting a proton beam. TRIUMF is using the proton beam with the highest intensity among ISOL facilities world-wide. The ISAC targets can handle proton currents up to about 100 µA [Bricault *et al.*, 2002]. (Re-)Ionization for the subsequent acceleration and separation is achieved by different sources [Bricault *et al.*, 2012], depending on the elements which are studied. To enhance ionization in an element-specific way and even suppress surface ionized species, for instance the TRIUMF resonant ionization laser ion source TRILIS [Raeder *et al.*, 2014] can be used. The ISAC mass separator has a maximum mass resolving power of about 2 000. The beam can be attenuated without changing the proton current (which may be needed to get the ions under study out of the target) by adjusting slits or by inserting attenuator grids in the ISAC beamline.

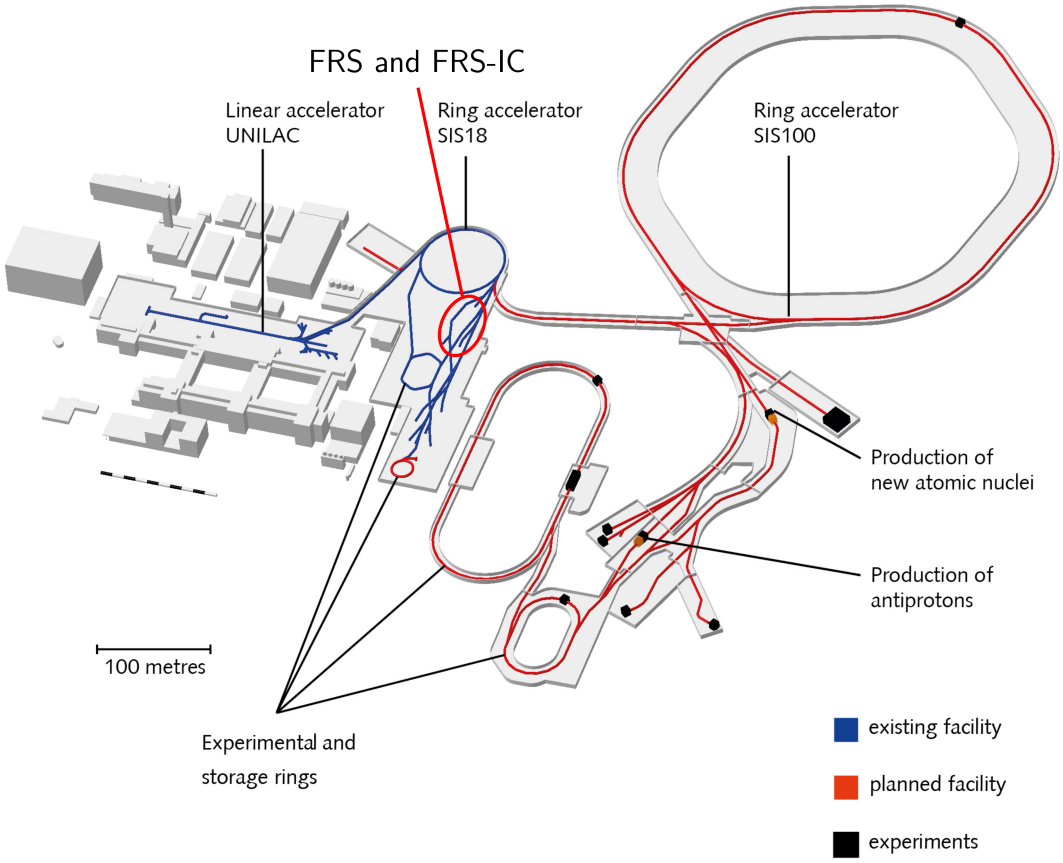

Figure 1.4: Drawing of existing and planned facilities at GSI/FAIR, with FRS and FRS-IC (see chapter 2) indicated. In the present work, developments have been done at the FRS-IC, serving also for future experiments at the Super-FRS. Figure adapted from `https://www.gsi.de/fileadmin/oeffentlichkeitsarbeit/bilddatenbank/fair/FAIR-beschriftet_MSV_EN_Aug_2021.jpg`.

1.4 Mass Spectrometry

The mass of exotic nuclei is a key property for progress in nuclear physics. Different techniques for measuring masses in various instances have thus emerged, each suitable best for certain nuclei. Challenges are half-lifes, production rates, sensitivity, dynamic range or accuracy. Masses of nuclei can be measured directly as described below or by indirect methods, *i. e.* via decay energies or through reactions using energy conservation and the masses of all reactants. Indirect methods will not be treated here but it is important to note that the knowledge of a single mass allows the determination of all masses in a decay chain, as this single mass provides an anchor point for the complete chain.

Besides obtaining the actual mass values, mass spectrometry can be used for identifying and quantifying constituents of the beam. Applications include mass analysis in life sciences [Ambiprobe; Dickel *et al.*, 2013], nuclear reaction studies and cross section measurements, and beam diagnostics and development at accelerator facilities [Purushothaman *et al.*, 2013; Wolf *et al.*, 2013b; Reiter *et al.*, 2020].

Direct mass measurement techniques are based on the interaction of charged particles with electromagnetic fields governed by Maxwell's laws. Measured quantities include detection positions after or whole trajectories of particles being exposed to magnetic fields; Oscillation frequencies of particles in combined electric and magnetic fields (*e. g.* in storage rings and Penning traps); and flight-times of particles in electrostatic or combined magnetic and electric fields. For state-of the art examples and the basic principle of the techniques exceeding mass resolving powers of 100 000 are given in the following, Multiple-Reflection Time-of-Flight Mass Spectrometry (MR-TOF-MS) is described in more detail from the next subsection on since it is the method which was employed in this work.

There are two main storage ring mass measurement techniques, isochronous mass spectrometry (IMS) and schottky mass spectrometry (SMS). They rely on measuring the revolution time or frequency of ions in the storage ring. The relative accuracies of the frequency f, $\frac{\Delta f}{f}$, the mass-to-charge ratio m/q, $\frac{\Delta(m/q)}{m/q}$ and the ions velocity v, $\frac{\Delta v}{v}$ are connected by the relation

$$\frac{\Delta f}{f} = -\frac{1}{\gamma_t^2}\frac{\Delta(m/q)}{(m/q)} + \left(1 - \frac{\gamma^2}{\gamma_t^2}\right)\frac{\Delta v}{v}\,. \tag{1.21}$$

The parameter γ_t is called the transition-γ and γ is the relativistic Lorentz factor, $\gamma = (1-\beta^2)^{-1/2}$ with $\beta = v/c$ and c the speed of light. Both techniques were for instance used at the experimental storage ring (ESR) located behind the FRS (Fig. 1.4). A recent review on storage rings including the two techniques is [Steck and Litvinov, 2020].

In *IMS*, a high accuracy in the mass-to-charge ratio obtained from the measured frequency is achieved by tuning the storage ring isochronous, *i. e.* for nuclei of interest $\gamma_t = \gamma$. This is only valid for one species, but it results in short measurement ($\approx 10\,\mu s$ to $100\,\mu s$) times with high resolving power up to 2×10^5 and accuracy down to 2×10^{-6}. A measurement was also reported with only 2 ions, in this case with an relative uncertainty of $\approx 7 \times 10^{-6}$ (900 keV at mass number $A = 130$) [Knöbel *et al.*, 2016].
In *SMS*, high accuracy in the mass-to-charge ratio obtained from the measured frequency is achieved by cooling the ions, resulting in $\frac{\Delta v}{v} \to 0$. This applies to all species in the ring, yields higher resolving power (up to 2×10^6 for heavy elements due to the almost mass-independent error [Litvinov *et al.*, 2005]) and better accuracy (down to 1.5×10^{-7}) than IMS, but is considerably slower, the measurement time is in the range of several to several ten seconds. The accuracy around 2×10^{-7} could also be reached with single ions [Litvinov *et al.*, 2005].

There are two main Penning trap mass measurement techniques for exotic nuclei based on measuring the ion's cyclotron frequency $\omega_c = \frac{qB}{m}$ in a homogeneous magnetic field of strength B, the Time-of-Flight Ion Cyclotron Resonance (TOF-ICR) and Phase-Imaging Ion Cyclotron Resonance (PI-ICR) methods. They are extracting the mass-to-charge ratio from the ion cyclotron resonance (ICR) frequency. The actual motion in Penning traps has three independent modes due to a homogeneous magnetic and an additional axially confining electric field. The modes have the three eigenfrequencies

$$\omega_z \approx \sqrt{q/m} \qquad \omega_\pm = \frac{\omega_c}{2} \pm \sqrt{\frac{\omega_c^2}{4} - \frac{\omega_z^2}{2}}\,. \tag{1.22}$$

The radial ion motion modes can be excited by applying dipolar RF pulses with the respective eigenfrequencies $\omega_\pm$. They can be converted by applying quadrupolar RF pulses with the sum of the eigenfrequencies, *i. e.* the cyclotron frequency ω_c.
In *TOF-ICR*, ions start at a low-energy magnetron-orbit, which is converted to a high energy cyclotron orbit. The frequency used for the conversion pulse is scanned (with a fixed conversion pulse duration) to find the ICR, at which the conversion is optimal. The cyclotron mode is associated with a higher magnetic moment. To measure the conversion, the ions are ejected from the trap in axial direction, drift through a magnetic field gradient, and their TOF is detected. The magnetic moment leads to acceleration, reducing the TOF to the detector accordingly and hence according to the mode conversion efficiency which is determined by closeness to the ICR frequency which in turn is given by the mass. The width of the recorded resonance curve is related to the length of the

conversion pulse and thus Fourier-limited. Resolving powers of about 1×10^6 and accuracy in the high 1×10^{-8} range is achievable with about 100 ions and measurements times of about 1 s [Blaum *et al.*, 2013].
In *PI-ICR*, the phase of the ion's motion is detected with a position sensitive detector. This approach is not Fourier-limited and no parameter is scanned, which increases resolving power and sensitivity, about ten ions are enough for a mass measurement. Highest accuracy mass measurements nowadays are obtained with PI-ICR. The method is more wide-band than TOF-ICR but very narrow-band compared to Multiple-Reflection Time-of-Flight Mass Spectrometer (MR-TOF-MS).

Besides measuring masses, Penning traps can be and are used for low energy beam preparation like (mass-selective) buffer gas cooling. An overview of Penning trap techniques (without PI-ICR), IMS, SMS and related topics is given by [Blaum, 2006]. A recent review on mass measurements with Penning traps including PI-ICR is [Dilling *et al.*, 2018].

1.4.1 (Multiple-Reflection) Time-of-Flight Mass Spectrometry

In low-energy time of flight (TOF) mass spectrometry, an ion sample is prepared, flies through a drift region of length l, the TOF analyzer, and the TOF t is detected for instance by measuring the current of a secondary electron multiplier (linear TOF mass spectrometer (MS), compare Fig. 1.5a). The mass resolving power R can be expressed by the TOF and the respective peak width Δt (FWHM)

$$R = \frac{m}{\Delta m} = \frac{t}{2\Delta t}\,. \tag{1.23}$$

Here only the case where the ion sample is prepared by bunching and cooling in a buffer-gas filled radio-frequency (RF) ion trap (injection trap) and extracted with a homogeneous field of strength E_{extr} is considered. In a linear TOF-MS with the time-focus tuned onto the detector, the peak width is dominated by the turnaround time in the injection trap,

$$\Delta t_{\mathrm{ta}} = \frac{\sqrt{8 \ln 2 m k_B T}}{q E_{\mathrm{extr}}}\,. \tag{1.24}$$

Here m and q are the ions mass and charge, k_B is the Boltzmann constant, and T the temperature. The extraction field strength also determines the energy spread of the sample and thus the time-focus length. This coupling limits the resolving power of a linear TOF-MS, as an increase in drift length requires a reduction of the extraction field strength, which can not be done arbitrarily. Employing an electrostatic reflector [Alikhanov, 1957] decouples the time-focussing

from the extraction field strength, which can now be increased to reduce the turnaround time. The reflector can technically also be implemented by using a coaxial design with two switchable electrostatic mirrors as shown in Fig. 1.5b and described below, here a gridless design is strongly favourable. However this increase is limited in practice by the energy focussing properties of the reflector, which is limited in range, leaving the turnaround time a limitation of the resolving power of this reflectron TOF-MS.

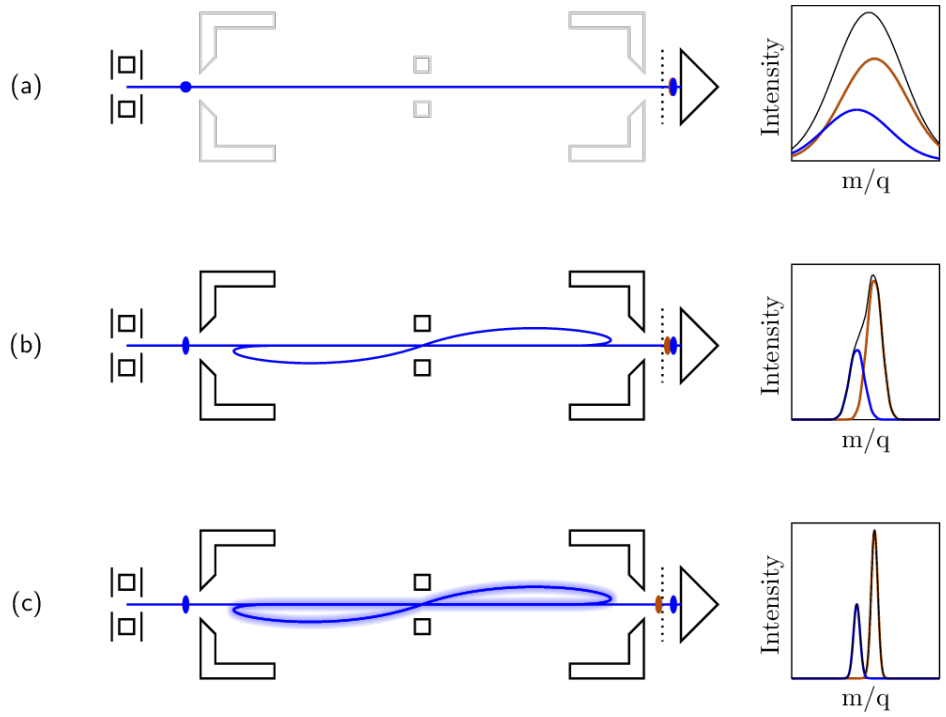

Figure 1.5: A sketch of (a) a linear TOF mass spectrometer, a linear TOF mass spectrometer with one time-focus shift turn (TFST) and (c) a Multiple reflection TOF mass spectrometer and respective mock-up mass-to-charge spectra. Components from left to right are the injection trap, the TOF analyzer with deflection electrodes in its center for in-analyzer cleaning of the beam (grayed out in case of the linear TOF-MS), a Bradbury-Nielsen gate, and the detector. In (a), the time-focus is set onto the detector by tuning the injection trap, whereas in (b,c) the injection trap is tuned to reduce the turnaround time and the primary time focus is shifted onto the detector by the TFST. The ions' trajectory is sketched in blue, in (b) it is folded once for the TFST, and in (c) it is folded multiple times inside the analyzer, corresponding to one TFST and multiple isochronous turn (IT). The spectra show a sample with two close lying species (blue and brown) after converting TOF to mass-to-charge, the observable sum spectrum is added in black. The ions, indicated by ellipses at or close to time-foci and dots elsewhere, are not (completely) separated in TOF-MS (with TFST), whereas in MR-TOF-MS they are, thus increasing the mass resolving power and separating the peaks in the spectrum.

To overcome these limitations, MR-TOF-MS have been proposed, build, and recently started to produced scientific results. Here, the flight path is extended by storing the ions inside the analyzer between two electrostatic mirrors. Injection and storage can be achieved by (i) switching the entrance mirror to a low potential during injection and subsequently switching it high, both with respect to the kinetic energy of the ions or by (ii) having the ions fly with a kinetic energy high enough to pass the entrance mirror and pulsing the drift tube from high to low potential while the ions are in that region. Ejection from the analyzer for detection or further processing of the mass-separated beam can be similarly done by switching the exit mirror or the drift tube. In the first case, care has to be take that ions trajectories are not affected by switching fields to, *e. g.*, avoid deterioration of mass accuracy in measurements. In the second case, the same applies and in addition only ions which are traveling towards the exit detector are ejected.

During storage in the analyzer, the ions repeatedly pass the drift region, multiplying the length of the flight path, and consequently disperse in TOF according to their mass-to-charge ratios, see Fig. 1.5c. Here two passes of the drift region are called one turn. With increasing number of turns, often several hundred, the accumulated peak-broadening due to aberrations per turn will dominate the overall peak width and the turnaround time becomes less limiting. The analyzer therefore needs to be carefully designed to achieve high order time focusing with respect to energy and spatial spread, for instance accelerating lenses are needed to ensure 2^{nd} order energy focusing.

The potentials of the mirrors and the lenses inside the analyzer are usually tuned to have a time focus length equal to one full turn. These turns are called ITs and their number will be abbreviated N_{it}. To obtain a narrow TOF distribution for a single species or equivalently a high mass resolving power, the time-energy focus is usually shifted to the detector. There are several ways to do this, summarized and extended in [Dickel *et al.*, 2017a]. These methods are (i) shifting the time focus by tuning the ion source, usually with different ejection field strengths, (ii) shifting it by tuning the potentials of the TOF analyzer which will then only be valid for one fixed number of turns since this deviates from the isochronicity condition, (iii) shifting it by using an additional reflector between ion source and TOF analyzer or between TOF analyzer and detector, called time-focus shift (TFS) reflector, and finally (iv) shifting it by changing the potentials of the TOF analyzer only in a few –typical one– turns. The latter method is the one which was introduced in the above cited paper and is called dynamical time focus shift (in contrast to the static time focus shift by changing the TOF analyzer voltage for a fixed turn number) the additional turn is called TFST. The flight-time of a reference ion from the trap to the detector without

doing any isochronous turns will be denoted t_{tfs}, which includes typically one TFST in case (iv) above. Similarly, the flight path will be denoted l_{tfs}, and for the isochronous turns the index "it" will be used. In an MR-TOF-MS the total flight path and time for a given ion are thus

$$l_{\mathrm{total}} = l_{\mathrm{tfs}} + N_{\mathrm{it}} l_{\mathrm{it}} \tag{1.25}$$

$$t_{\mathrm{total}} = t_{\mathrm{tfs}} + N_{\mathrm{it}} t_{\mathrm{it}} \,. \tag{1.26}$$

In MR-TOF-MS, the width Δt (FWHM) of the TOF-peak and the *total* flight time determine the mass resolving power,

$$R = \frac{t_{\mathrm{total}}}{2\Delta t} \,. \tag{1.27}$$

The peak width is given by the initial width (*i. e.* the turnaround time width Δt_a), the width due to aberrations without isochronous turns Δt_{tfs}, and the width due to aberrations during the isochronous turns Δt_{it}. The widths due to the aberrations depend on the phase space and all non-vanishing aberration coefficients. Assuming independent Gaussian distributions, the widths can be quadratically added[2],

$$\Delta t^2 = \Delta t_a^2 + \Delta t_{\mathrm{tfs}}^2 + N_{\mathrm{it}}^2 \Delta t_{\mathrm{it}}^2 \,. \tag{1.28}$$

The width Δt_a can be calculated from physical properties [Dickel, 2010] and the combined width in zero turns ("pass-through") $\Delta t_{0\mathrm{t}}^2 = \Delta t^2(N_{\mathrm{it}} = 0) = \Delta t_a^2 + \Delta t_{\mathrm{tfs}}^2$ can be measured. The resolving power evolves with the turn number according to

$$R = \frac{t_{\mathrm{tfs}} + N_{\mathrm{it}} t_{\mathrm{it}}}{2\sqrt{\Delta t_a^2 + \Delta t_{\mathrm{tfs}}^2 + N_{\mathrm{it}}^2 \Delta t_{\mathrm{it}}^2}} \,. \tag{1.29}$$

With the substitution $R_\infty = \frac{t_{\mathrm{it}}}{2\Delta t_{\mathrm{it}}}$, this becomes

$$R = \frac{N_{\mathrm{it}} + \frac{t_{\mathrm{tfs}}}{t_{\mathrm{it}}}}{\sqrt{N_{\mathrm{it}}^2 + \frac{\Delta t_a^2}{\Delta t_{\mathrm{it}}^2} + \frac{\Delta t_{\mathrm{tfs}}^2}{\Delta t_{\mathrm{it}}^2}}} R_\infty \,. \tag{1.30}$$

The TOF-dispersed beam can then be ejected as described above for mass measurements or further processing. Spatial mass separation can be achieved by

[2]This is generally true for independent contributions when adding standard deviations σ, but for the FWHM only if σ and FWHM are linearly dependent. This holds for Gaussian distributed random variables. Furthermore these contributions are all functions of the same initial phase space, and as such not strictly independent, but the approximation has shown to be sufficiently accurate.

removal of the unwanted ions using a fast-switching deflector after ejection, such as a Bradbury-Nielsen gate (BNG) [Plaß *et al.*, 2008]. Other convenient but less powerful methods are a dedicated timing of the pulsed drift tube [Wienholtz *et al.*, 2017] or one of the exit mirrors [Johnson *et al.*, 2019]. These methods are well suited if a different kind of experiment or detection is to be performed afterwards, *i. e.*, when disturbances of the phase space of the extracted ion sample due to the influence of the switched fields is not important. This can be α-spectroscopy, where nuclear isomers could be separated with a BNG after the TOF dispersion [Dickel *et al.*, 2015a] or, *e. g.*, any experiment where the ions are recaptured in-between for a new sample preparation. Furthermore the TOF-dispersed ions can also be separated prior to ejection with dedicated switched electrodes (Fig. 1.5), which can be used for mass range selection as well [Toker *et al.*, 2009]. The novel method of mass selectively re-trapping the ions in the injection trap after TOF dispersion was for the first time applied with exotic nuclei in this work and will be treated in chapter 4.

In addition to direct mass measurements of exotic nuclei [Wienholtz *et al.*, 2013; Ito *et al.*, 2018; Ayet San Andrés *et al.*, 2019a] and mass separation, MR-TOF-MS can be used for diagnostics purposes [Purushothaman *et al.*, 2013; Wolf *et al.*, 2013b] and for development of Rare isotope beams (RIB) [Reiter *et al.*, 2020].

MR-TOF-MS feature very high mass resolving powers of several 10^5 and short cycle times. This enables the access to very short-lived ($\approx$ ms) ions, and for a given ion capacity per cycle it translates to a high overall ion capacity. At the same time, MR-TOF-MS is a sensitive method allowing measurements with ten ions only [Hornung *et al.*, 2020] and it is possible to measure several mass units at once.

1.4.2 Multiple-Reflection Time-of-Flight Mass Spectrometry Data Analysis

The experimentally measured quantities are flight times of ions. The TOF data can be converted to mass data by calibration with known species and then analyzed further. In this work, the analysis procedure for MR-TOF-MS data developed at the Justus-Liebig-Universität Gießen is used. It was published by Ayet San Andrés *et al.* [2019a] and is shortly summarized in the following for the purpose of this work.

The underlying basics is the relation between total TOF t_{total} and flight path l_{total} (eqs. 1.25, 1.26), effective voltage along this path U_{eff} and the ions mass-to-charge ratio m/q,

$$\frac{m}{q} = \frac{2U_{\text{eff}}\, t_{\text{total}}^2}{l_{\text{total}}^2}\,. \tag{1.31}$$

Experimentally, a time offset needs to be accounted for due to electronic delays, such that the total TOF is not the measured one,

$$t_{\mathrm{exp}} = t_{\mathrm{total}} + t_0 \,. \tag{1.32}$$

This offset can be measured in a preliminary calibration step at the experimentally setups used in this work. Introducing the calibration parameters $b = l_{\mathrm{it}}/l_{\mathrm{tfs}}$ and $c = 2U_{\mathrm{eff}}/l_{\mathrm{tfs}}^2$, the calibration formula is

$$\frac{m}{q} = \frac{c(t_{\mathrm{exp}} - t_0)^2}{(1 + N_{\mathrm{it}}b)^2} \,. \tag{1.33}$$

As the parameter b includes the path length for isochronous turns, it is more sensitive to temporal drifts of the analyzer length than c. The parameter c is for the pass-through mode and thus almost time-independent. In practice this is exploited by putting all time-dependence into b when a calibration of a long-term mesurement is made, see below.

For the evaluation of the mass data, MAc [Pikhtelev, 2010-2015; Bergmann] and R [R Core Team, 2021] are used. MAc is also used for the data acquisition. The data acquisition and evaluation procedure is the following:

1. Calibrate the spectra for on-line and preliminary identification in MAc:

   - Measure t_0 by recording a spectrum with several known ion species in a pass-through mode, *i. e.* without doing turns. This corresponds to $N_{\mathrm{it}} = 0$, so the parameter c can while b can not be determined in this step.
   - Calculate b by recording a spectrum with at least one known ion in a multi-turn mode, *i. e.* $N_{\mathrm{it}} > 0$, typically a few hundred. If there are several known ions performing a different number of turns, a more accurate determination of c can be obtained as well.

2. Fine calibration for more precise preliminary and further analysis in MAc: Temporal drifts are accounted for by calculating b in a time resolved way, *i. e.* by splitting the spectrum in several blocks and calculating b for each of these blocks.

3. Precision mass value determination: Export the time-resolved calibrated data in list mode from MAc and fit the calibrant and the ions of interest with a weighted maximum likelihood estimation (wMLE) in R. For these fits, the peak shape will first be determined with a high statistics peak and then the masses of exotic ions will be fitted with a wMLE fit to this peak shape. The peak shape which is used is the hyper-exponentially modified

Gaussian (hyper-EMG) [Purushothaman *et al.*, 2017], which incorporates exponential tails from ion-optical aberrations in a phenomenological way.

4. Uncertainty determination: For the estimation of the uncertainty of the mass value, several components are added quadratically. These are the statistical uncertainties of the calibrant and ion of interest, the mass uncertainty of the calibrant, uncertainties due to the fitting procedure (peak shape parameter uncertainties), due to the calibration (uncertainties of c, b and t_0 and of the TRC interpolation of b), due to known systematic errors (time of flight shifts caused by switched fields), and due to estimated but unknown systematic contributions.

To get atomic mass values, the determined mass-to-charge values of ions have to be corrected according to their charge state and the respective number of electron masses (or proton masses in case the atom/molecule of interest has been protonated or deprotonated to get a charged ion) has to be added or subtracted. Atomic mass values of isotopes ${}^{\mathrm{A}}_{\mathrm{Z}}\mathrm{X}$ are often tabulated in units of keV/c_0^2 as mass excess (ME) values,

$$\mathrm{ME}({}^{\mathrm{A}}_{\mathrm{Z}}\mathrm{X}) = m({}^{\mathrm{A}}_{\mathrm{Z}}\mathrm{X}) - A\,\mathrm{u}\,. \tag{1.34}$$

$1\,\mathrm{u} = m({}^{12}_{6}\mathrm{C})/12$ is the atomic mass unit, defined as $\frac{1}{12}$ of the atomic mass of ${}^{12}_{6}\mathrm{C}$.

Chapter 2

Developments at the FRS Ion Catcher

2.1 The FRS Ion Catcher Setup

The FRS ion catcher (FRS-IC) [Plaß *et al.*, 2013a] is a setup located at the final focus of the main branch of the FRS [Geissel *et al.*, 1992] at GSI/FAIR. The FRS-IC is designed for universal stopping and preparation of relativistic secondary beams, to be used for its own measurements or for delivering a low energy secondary beam to other experiments. It consists of a Cryogenic Stopping Cell (CSC) [Ranjan *et al.*, 2011; Purushothaman *et al.*, 2013], a recently extended RF quadrupole (RFQ) beamline [Reiter, 2015; Hornung, 2018] including diagnostics, calibration sources and detectors, and an MR-TOF-MS for ultra-high-precision mass measurements [Plaß *et al.*, 2008; Dickel *et al.*, 2015b]. The present work includes developments for the whole setup, but focuses on the MR-TOF-MS, which is in detail described in Dickel [2010]; Yavor *et al.* [2015]; Plaß *et al.* [2015]. Recent development before this work are described in Ayet San Andrés [2018]. In short, the FRS-IC MR-TOF-MS consists of an RFQ beamline filled with helium, including an RFQ switchyard (RFQ SY), an RF trap system, a coaxial TOF analyzer using two switched electrostatic reflectors and an accelerating lens, a drift tube on ground potential, a Mass Range Selector (MRS), a TFS reflector and a movable detector sled. The RFQ beamline and the RFQ SY transport the slowed-down exotic ions from the CSC either to diagnostics detectors or to the trap system and can mix it with ions from the internal ion source of the MR-TOF-MS for calibration. In the trap system, the ions are bunched, cooled and injected into the analyzer. The MRS selects a certain mass range to facilitate identification of peaks in the folded TOF spectrum [Dickel, 2010; Plaß *et al.*, 2013b]. After ejection from the ana-

lyzer, the TFS reflector guides the ions such that the time-focus is obtained on the detector, which can be chosen from one of the three slots on the detector sled. An overview drawing is shown in Fig. 2.1.

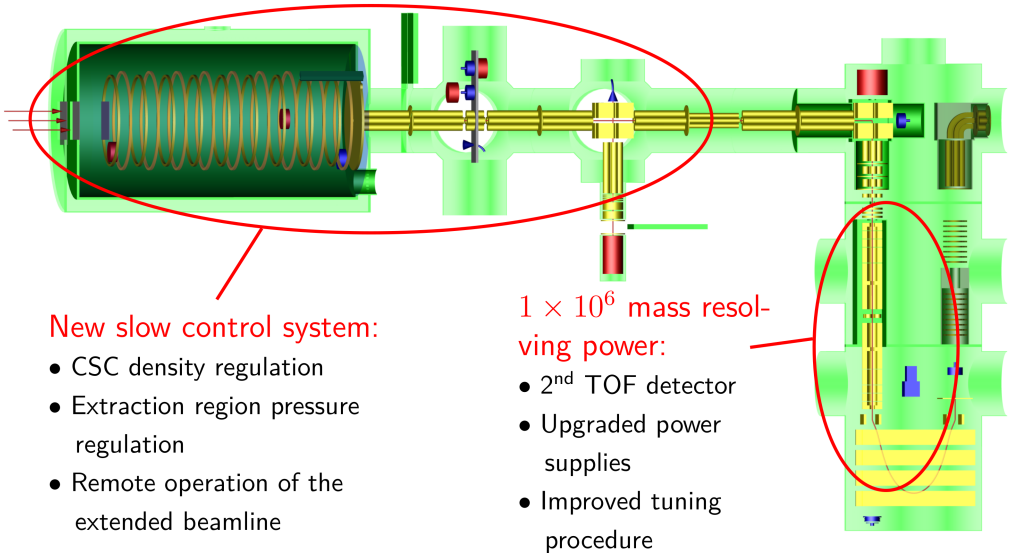

Figure 2.1: Schematic view of the FRS-IC with indicators which improvements were made in this work, for details see text. The FRS beam enters the CSC from the left. For mass or abundance measurements, the ions are transported through the RFQ beamline into the MR-TOF-MS RFQs where they are routed downwards by the RFQ SY and into the trap system. They are then injected into the TOF analyzer for mass analysis and after ejection and TFS reflection impinge on one of the detectors at the detector sled.

A main part of the science program at the FRS-IC [Plaß *et al.*, 2019] is mass measurements of very exotic nuclei. The detector setup characteristics allow determining masses of nuclei with half-lifes down to a few ms with about ten events only. Measuring unknown masses of exotic nuclei gets more challenging with every nucleon further away from the line of β-stability: On average, half-lives get shorter and production yields drop exponentially with exoticity. In consequence, experiments need to be able to provide accurate results with few events and/or more time needs to be spent for accumulating data. At the FRS-IC, both approaches are combined: The increase in mass resolving power described later enables more accurate measurements with few events, and a stable system makes long measurements —usually of several nuclei in parallel— possible. Stability is achieved through different means on different time scales. Typical time scales at the FRS-IC MR-TOF-MS are few ten ms for the time that the ions spend in the analyzer per turn t_{it}, hence a few up to about 40 ms

total TOF in the analyzer for 100 to 1000 IT. Data of several measurement cycles, on the order of one to a few seconds in total, are usually accumulated into TOF spectra. Variations on time scales larger than that can be corrected for by a time-resolved calibration, while variations on smaller time scales should be minimized by stabilizing *e. g.* the power supplies.

In this work, a new slow-control software for the overall setup was developed focusing on stability, and reliable and easy operation. Detectors were upgraded for improved tuning and diagnostics capabilities. Analyzer power supplies and electronics for beam alignment were upgraded and a systematic special tuning procedure was developed to finally achieve mass resolving powers beyond 1×10^6 (chapter 3), which were so far not achieved with any MR-TOF-MS world-wide.

2.2 FRS Ion Catcher Slow Control System

To ensure a proper time-resolved calibration, ions with well-known mass (calibrant ions) need to be supplied in a well controlled way, *i. e.* there should neither be any space charge nor should the calibrant ion rate be lower than that of the exotic nuclei (down to about 2 per hour); it should rather be higher and as stable as possible to provide enough total statistics for a good peak shape determination if overlapping peaks need to be treated and to have small enough calibration block size to minimize the respective uncertainty contributions [Ayet San Andrés *et al.*, 2019a].

Overlapping with the beginning of this work, an extension of the RFQ beamline of the FRS-IC was finished [Hornung, 2018]. The main motivation for this extension was a new, universal calibration source. Besides, the extension provides another stage of differential pumping between the CSC and the MR-TOF-MS and the CSC can thus be operated at higher densities while keeping the MR-TOF-MS analyzer pressure low. Furthermore, the extended beamline includes an RFQ mass filter for improved removal of molecular ions through the three-step process Isolation–Dissociation–Isolation [Greiner *et al.*, 2020]. In addition, there were hardware changes at the established FRS-IC setup, like the addition of multichannel analog-to-digital converters (ADCs) for reading various analog outputs and a change of vacuum transducers to a different model which for instance includes hardware relays which are planned to be used for safety functionality, and the power supply upgrade for the MR-TOF-MS analyzer electrodes (described below). For use in RIB experiments, the extended beamline and the new devices need to be controlled remotely.

A new slow control system for the complete FRS-IC was developed based on LabVIEWs actor-oriented framework, using the GSI in-house developed add-on classes collected in the Control System ++ (CSPP) [Brand and Neidherr, 2021].

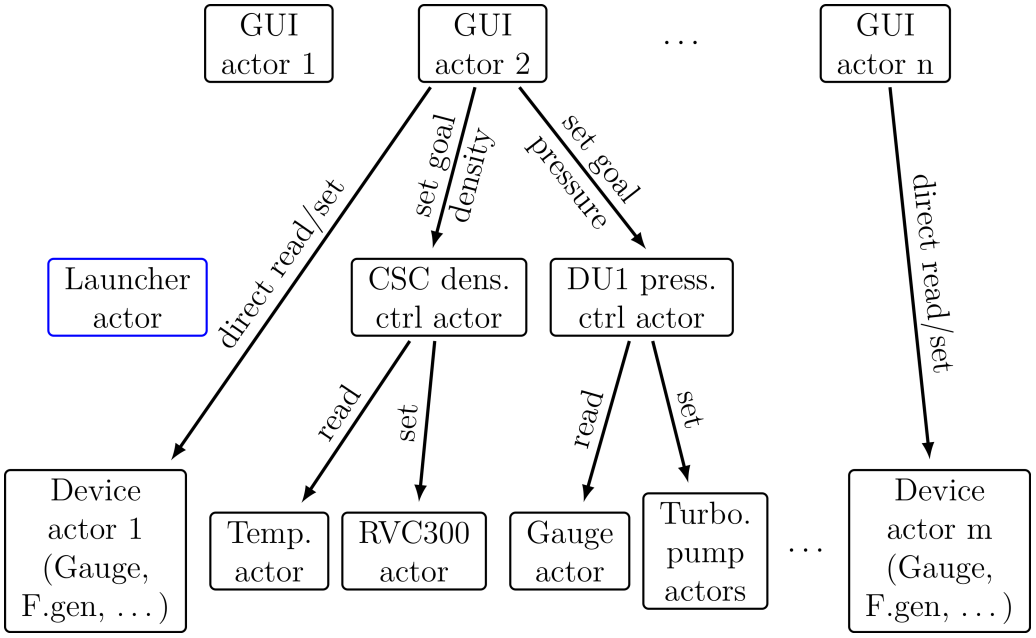

Figure 2.2: Scheme of the slow control structure with GUI layer at the top, control layer at the middle and device layer at the bottom. The launcher actor acts as a server, it starts and restarts device actors. The GUI actors serve to display read values (*e. g.* pressures) and let the user directly set device parameters (*e. g.* function generator frequencies) or define goal values for control actors. The control actors then set device parameters based on read values, *e. g.* set a pressure based on a read temperature and desired density.

The paradigm behind actor models is, similar to object-oriented programming, *everything is an actor*. Hence the term actor describes what may elsewhere be called a module, subroutine, function, or —in the case of LabVIEW— subVI. In practice subVIs still exist for code readability. Actors are inherently running in parallel, their interaction is governed by messages, a key concept of the actor model. Actors can receive messages and upon receipt react in different ways, including the creation of other actors and sending messages of their own. The structure of the new slow control is that of a layered software system using a graphical user interface (GUI) layer, a control layer and a device layer [Fig. 2.2]. The main actor is the Launcher actor, which runs on a dedicated slow control server. As client, the main GUI actor [Fig. 2.3] can be started on several computers in the network, giving users of the subsystems access to the respective device or control actors. Apart from the CSPP libraries and general help, the Launcher actor was written by Holger Brandt (GSI, EE)

[Brandt (Private communication)]. Much continuous development was done by Alexandru State and first results are published in [State *et al.*, 2022]. Part of this work was the overall design, driver and user interface development and testing and debugging in connection with the hardware.

A major technical improvement due to this framework was modularization, *i. e.* failing device actors can be independently restarted while the main actor keeps running. This reduces downtime and possible issues in case of a complete system restart or crash. Moreover, device actors are automatically restarted for a definable amount of times, such that the user only needs to interact when there is a probable hardware problem. The control layer was equipped with actors for improved experiment stability, namely by regulating the density in the CSC and the pressure in the extraction part of the beamline (DU1).

Since the new slow control combined devices from the two separate old control applications and new devices in one GUI, about three times as much controls and indicators needed to be placed per screen area. A small focus was hence put on making it easy to distinguish different device types, quickly spot problems and find readout values [Fig. 2.3]. Furthermore, the slow control can be adapted to small changes in the hardware (like using a different serial port) with a simple text editor. Adding devices without control via the main GUI can also be done in a textfile, this is for instance sufficient for adding another gauge or ADC and log the data to a database. For adding device to the operators main GUI, care was taken to program the actors subVIs in a way that an extension can be done by a person with some LabVIEW background, without the need to learn about the specialties of the actor framework or CSPP (see Appendix A).

The software is ready to read values of the ADCs present in the setup, *e. g.* to read the actual values at the MR-TOF-MS analyzer electrode behind low-pass filtered power supplies (see below) or currents from readout boards attached to apertures in the system. The voltage at the analyzer electrodes can differ from the supplied voltage when the low-pass filtered input is switched during the MR-TOF-MS cycle due to loading and unloading of the capacitors. The magnitude of the effect depends on the repetition rate and consequently a continuous reading facilitates changes of the repetition rate on the short timescale and serves for reliably establishing the same analyzer tune in the long term. Current readouts from internal source on apertures give an independent way to quantify efficiencies when tuning parts of the beamline, trap system or analyzer.

With the new slow control system, the FRS-IC setup works more reliable, such that several months up-time are possible. This is important for experiments where extremely rare events are investigated. Furthermore, the new

regulation makes the system more stable, for instance ion transport is less sensitive to environmental parameters, as demonstrated in [State *et al.*, 2022] by the stable rate of calibrant ions from the CSC.

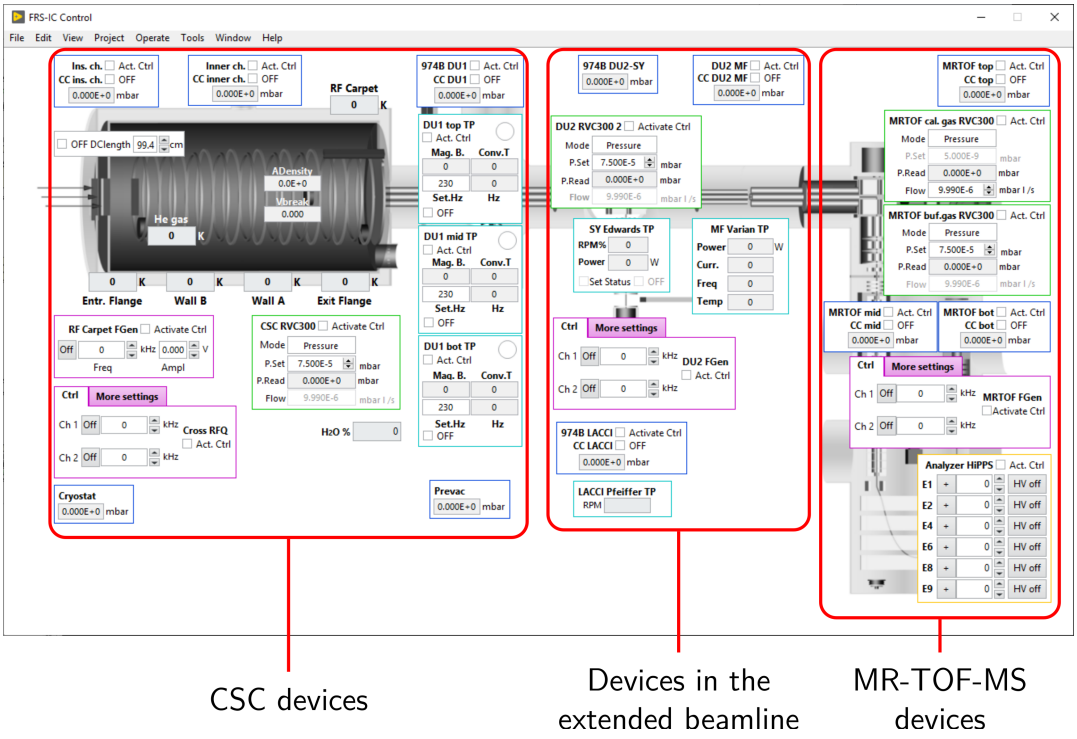

Figure 2.3: Screenshot of the main graphical user interface (GUI) of the new slow control system. The controls are arranged according to which part of the FRS-IC they belong to (red frames) and colored by device type (gas inlet, pressure measurement, pump, function generators, DC voltage). Some CSC devices can be controlled indirectly by setting the desired CSC density and the desired pressure for the extraction region of the beamline (DU1). In that case, control layer actors for the CSC density and the DU1 pressure set parameters for the device actors based on the read temperature and pressure and the user-supplied desired density and pressure. The control actors can be configured in additional GUIs, the values which are set by them are shown on the main GUI. Also values changed by other users running the main GUI on different computers are automatically updated.

2.3 Installation of a Second TOF Detector with Large Aperture

The MR-TOF-MS detector sled was overworked to support two isochronous secondary electron multiplier ETP MagneTOF detectors (Fig. 2.4) with the goal to increase reliability and avoid downtime during beamtime periods in case of failure of one of the detectors, and to improve tuning capabilities of the system. Apertures with different diameters were machined for a high transmission mode for an initially misaligned beam and a high resolution mode for accurate mass measurements after beam alignment. The new large aperture is used for the systematic beam alignment presented below; the small aperture for precision mass measurements. This is necessary, *e. g.*, for separating close lying peaks with strongly differing abundances since it reduces the background from scattered ions by a factor of about 3 [Will, 2019]. The different aperture areas also provide a means of coarsely measuring beam diameter and/or position and can thus serve for identification of severe problems[1].

At the FRS-IC, tuning is typically done with α-emitting isotopes. The decay of the implanted ions leads to random background in the spectra. Now, systematic tuning of beamline and MR-TOF-MS is possible on larger scale using the second detector, without contaminating the detector to be used for the precision mass measurements of nuclei with low yields.

2.4 Analyzer Power Supply Upgrades

In the high-resolution measurement mode of MR-TOF mass spectrometers, ions turn around in the mirror fields and pass lens fields several hundred times. The ions' time of flight is most sensitive to the voltages at the two outermost electrodes, and about a factor 3 less to the voltages at the next ("lens") electrodes [Dickel, 2010]. The most sensitive mirror voltages were already supplied by highly stable analog low-noise power supplies mounted in a temperature stabilized cabinet and additionally low-pass-filtered [Ayet San Andrés, 2018]. The remaining analyzer voltages were already low-pass-filtered, though the lens voltages have a lower order low pass filter due to the higher voltage and limitations of the available passive electronic components. To improve the stability

[1]For example, after the initial commissioning of the detectors, the count rate behind the large aperture was a factor 3 larger compared to behind the small aperture after about 100 IT, indicating that the beam diameter was much larger than expected. At that time, no mass resolving powers higher than 1×10^5 could be achieved. The observed count rate discrepancy led to finding an electrode disconnected inside the vacuum chamber, and the following repair enabled higher mass resolving powers again.

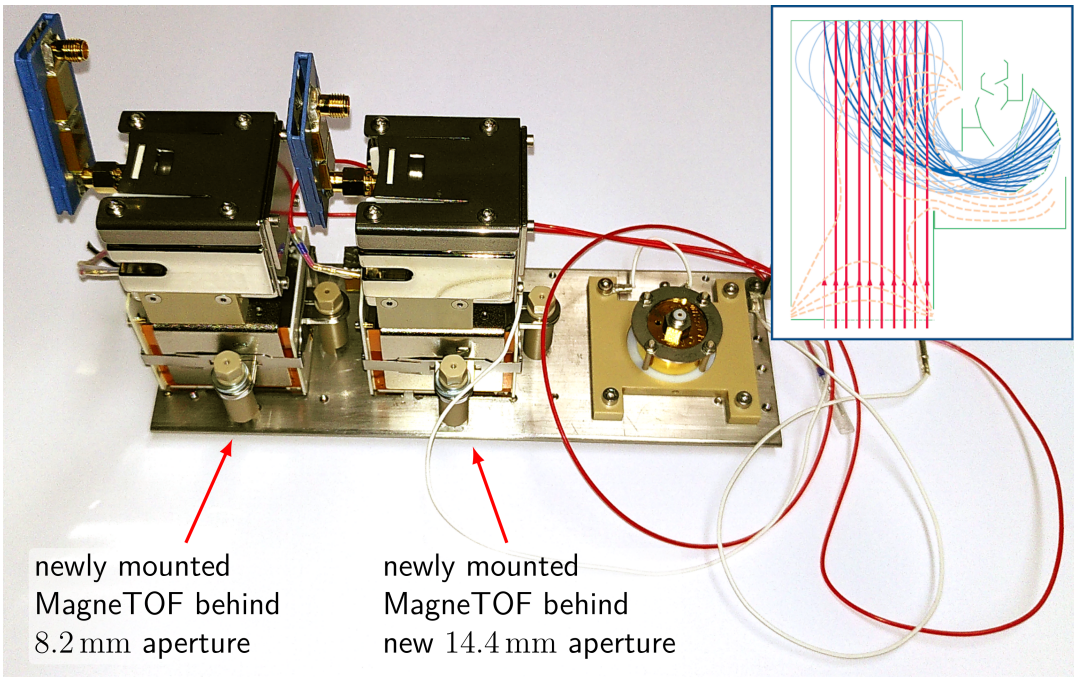

Figure 2.4: Photograph of the two MagneTOF detectors and the Si detector mounted on the overworked detector sled. The MagneTOF detector with the 8.2 mm aperture and the Si detector have been mounted before. For this work the aperture in the center was increased to a diameter of 14.4 mm, appropriate mounting threads were added, and an additional MagneTOF detector was mounted there. The inset shows a part of the electron-multiplying dynode structure of the MagneTOF detector in green, ion trajectories incoming from below in red, electrons guided from the impact plate to the first dynode by crossed electric and magnetic fields in blue, and dashed equipotential lines. The figure is taken from [Stresau and Hunter, 1999].

of the lens fields on short time scales, two more of the highly stable analog low-noise power supplies were mounted in the temperature stabilized cabinet, and the interior of the cabinet was rearranged and upgraded accordingly.

2.5 MR-TOF-MS Beam Alignment

High resolving power in MR-TOF-MS is achieved by first minimizing the turn-around time while keeping the time focus on the detector and subsequently extending the flight path. Since the latter is done by folding the path with electrostatic mirrors, the stability of the voltages at these mirrors and the ion-optical aberrations introduced by the mirrors and the lenses are limiting factors for the resolving power. The stability of the voltages was already improved in [Ayet San Andrés, 2018] and further improved in this work (section 2.4). The aberration coefficients can be tuned by changing the analyzer voltages, but the magnitude of the aberration also depends on the phase space. A procedure for tuning the TOF–energy aberrations was already established. Spatial aberrations then started to limit the performance due to mechanical misalignment of the trap system and the analyzer in the MR-TOF-MS. The beam has to be aligned to provide a phase space suitable for reaching ultra-high resolving powers. The alignment of the beam in the MR-TOF-MS analyzer is essentially a four dimensional problem. The beam must hit the center (two dimensions) under zero angle (another two dimensions). In practice with the given experimental setup this can be achieved by hitting the center by tuning the two dipole steerers between the trap system and the analyzer and removing the tilt by steering with the MRS electrodes. The concept was developed by [Dickel (Private communication)] and the process is illustrated in Fig. 2.5. This splits the four-dimensional problem into two two-dimensional problems, if hitting the analyzer center and removing the tilt can be quantified independently. To achieve this, we use the MRS electrodes as a quadrupolar electrostatic lens and observe the induced shifts in the time-of-flight, proposed and simulated by [Yavor (Private communication)], and the induced change in transmission, both compared to the values in pass-through mode. When the center is hit, no change in field or potential is experienced by the ions and the time-of-flight does not change. Similarly, in an ideal central hit the quadrupole lens does not act as a lens and the transmission is not affected, although the converse is not necessarily true (*i. e.* the transmission may stay the same although the center is not hit).

In this work, firstly electronics were adapted to make these measurements possible, also with limited access to experiment areas, *i. e.*, by remote operation. HV switches were combined such that (i) steering is possible with a pair of dipole

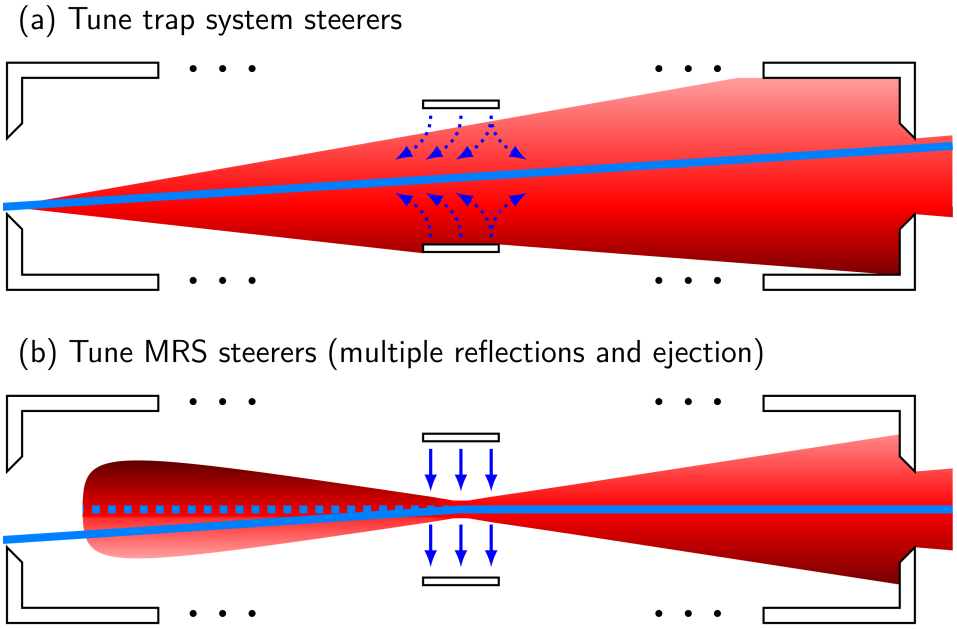

Figure 2.5: Sketch of the two step beam alignment procedure showing the MR-TOF analyzer end cap electrodes, two MRS electrodes in the center, and in blue the beam after (a) the first and (b) the second optimization step. The color-fading cones show areas covered by the beam when the steerers are scanned. (a) Trap system steerers are scanned once while the MRS is operated as quadrupole lens (field lines indicated by dashed dark blue arrows), and once while it is on ground potential. (b) With the optimal trap system steerer values from (a), the MRS steering voltages are scanned (steering field lines indicated by dark blue arrows). The focusing of the quadrupole lens and the analyzer lenses is omitted in the sketch, with their focusing the beam is transmitted for a larger range of steering voltages than indicated. In the second step, after steering during the first passage of the MRS electrodes, the ions undergo multiple turns to accumulate sufficient aberration broadening for analyzing the peak width dependence on the misalignment. The color-fading in case of multiple reflections was chosen for illustration, in the real system the beam would illuminate both sides of the optical axis in both halves of the analyzer for any non-vanishing misalignment. The ions are then ejected, and TOF spectra are recorded for each steering voltage. For details on the actual optimization see text.

steerers (previously, a single dipole steerer was available) and (ii) the mode can be changed easily to use the MRS electrodes as quadrupole lens in pass-through mode. The change between these configurations can be done remotely by adapting the timing settings (*i. e.* by changing the logic signals controling the HV switches, shown in the upper part of Fig. 2.6) of the MR-TOF-MS and the supplied voltages. All electronic components including overcurrent protection and passive voltage stabilization for the steering and deflection voltages were mounted in a 19" rack-mountable box [lower part of Fig. 2.6] to install it in a secure and compact way at the existing setup.

In first attempts of probing the position at the analyzer center, it was found that the count rates are the more direct to use probe than the time-of-flight and thus these were used for probing the beam position in the analyzer center. The time-of-flight approach was later analyzed again and an expected quadrupolar pattern was found underneath a dominant linear time-of-flight shift, but open questions remained as the origin of the linear shift could not yet be explained. The steps towards these preliminary results are shown in appendix B and the results are compared to ion-optical simulations. For the quantification of the proximity to the analyzer center used to obtain the results in this work, count rates with and without quadrupolar field were compared to minimize their difference. The ion optics with which the new procedure was first established is not rotationally symmetric, as the TFS reflector has a planar geometry, and is focusing spatially only in one direction while not acting in the other direction. To be able to work with the transmission, the TFS lens voltages were changed such that the beam is defocussed in both directions on the detector similarly, making the change in transmission sensitive to misalignment in both directions. The voltages were found by SIMION simulations, they are 200 V less negative than the regular voltages for the ions starting at 1.3 keV energy.

Minimal transmission difference can be the case for a steering which is unfavorable for the transmission of the downstream part of the setup, *i. e.* the second half of the analyzer and the TFS reflector with surrounding dipole deflectors. For this, the detector with the new larger accessible detection area is needed. Once the trap steerers are optimized, the remaining tilt has to be removed by operating the MRS electrodes in their standard configuration, *i. e.* for steering in the first pass and cutting the mass range afterwards. This optimization is more direct, as one can simply maximize count rate or resolving power.

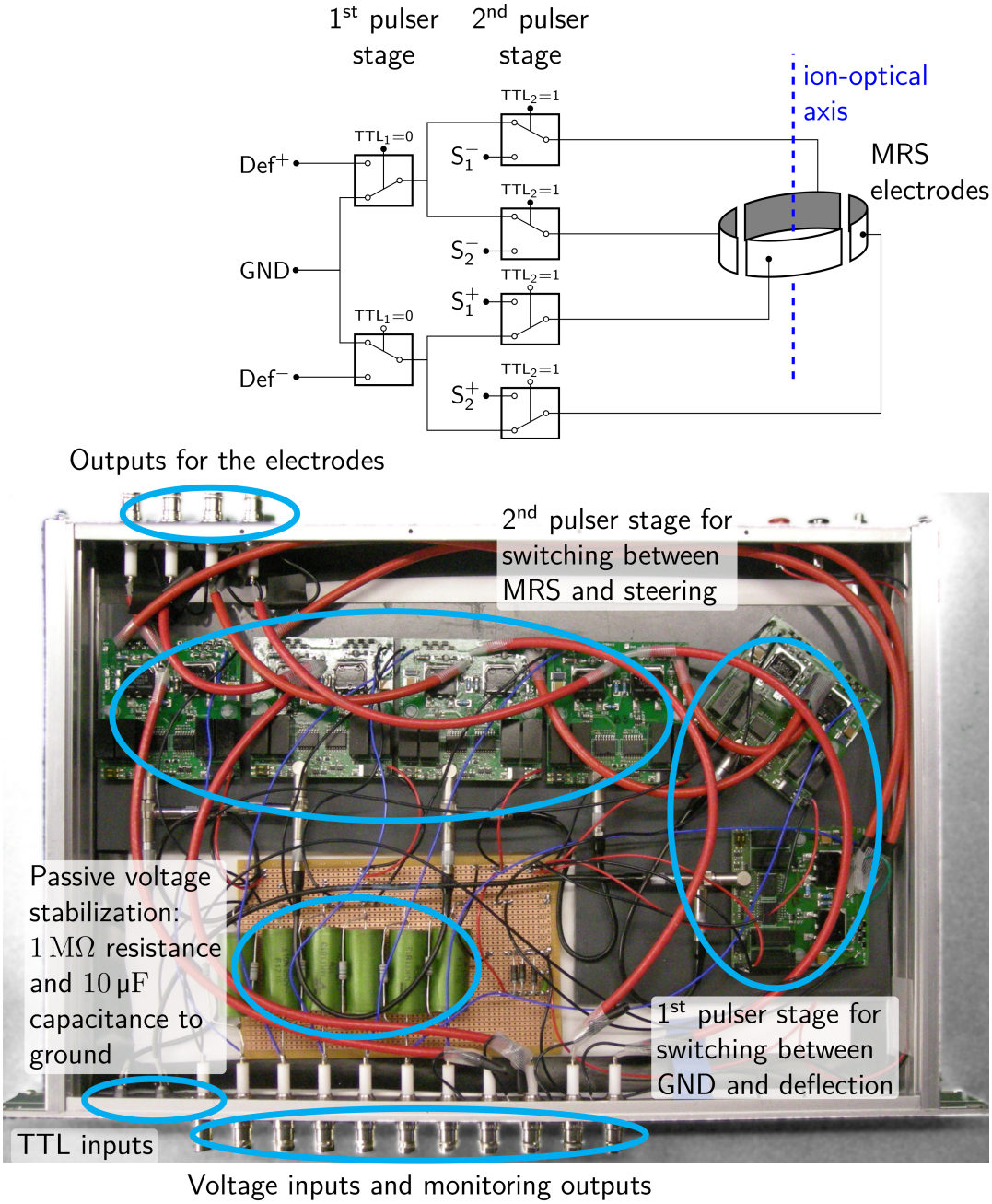

Figure 2.6: Inner parts of the new MRS box including passive voltage stabilization and high voltage pulsers. The hardware is mounted in a 19" rack unit for compact integration into the existing setup. The schematic above shows the connections of the pulsers to the inputs (ground GND, deflection $\mathsf{Defl}^{\pm}$ and two steering voltages $\mathsf{S}^{\pm}_{1,2}$), to each other, and to the MRS electrodes. The operation of the MRS is governed via two logic signals TTL_1 and TTL_2 (shown in ground operation), which are internally inverted for the three lower pulsers.

Several improvements have been implemented for the FRS-IC in this work: The new slow control system for reliable and stable long-term operation, a second TOF detector for reliability and improved tuning capabilities of the MR-TOF-MS, upgraded power supplies for improved stability of the electrostatic fields in the MR-TOF-MS and thus higher mass resolving power, electronics for steering the beam inside the MR-TOF-MS in two dimensions and for probing the beam position in the analyzer center, and a repeatable and systematic procedure for aligning the beam inside the MR-TOF-MS. This procedure and the latter two described modifications will be applied in the next chapter, where the so far highest mass resolving power is reached with an MR-TOF-MS.

Chapter 3

Developments for Highest Mass Resolving Power at the FRS Ion Catcher

The developments in the previous chapter enabled repeated systematic tuning to reach a mass resolving power[1] of $R = m/\Delta m = 1 \times 10^6$ and beyond. Higher resolving powers directly increase the reach of mass measurements for nuclear physics: The mass resolving power determines the uncertainty for measurements with few events, and ultra-high resolving power is needed for the separation of close-by peaks in the spectra, *e. g.*, for the separation of ground and isomeric states and the determination of their excitation energy. The uncertainty due to statistics can be estimated by the standard error of the mean. For Gaussian peaks this is

$$\sigma_{\text{stat., Gauss}} = \frac{\sigma_{\text{peak}}}{\sqrt{N_{\text{events}}}} \tag{3.1}$$

with the number of events N_{events} and the standard deviation of the Gaussian distribution σ_{peak}. The statistical uncertainty is dominating for the most exotic nuclei, where the number of events is very low (*i. e.* below ten events). To minimize the uncertainty one consequently aims for narrow peaks, *i. e.* a small σ_{peak}, or equivalently for ultra-high resolving powers $R \sim 1/\sigma_{\text{peak}}$. Finally, narrow peaks mean narrow windows in TOF or mass, in which the events are located. While this sounds like a tautology first, the direct experimental benefits are that (i) in narrower TOF windows there is less total background, which for a low number of total events can be decisive, and (ii) in narrower

[1]The mass resolving power will be given as the full width at half maximum (FWHM) mass resolving power throughout the chapter, *i. e.* Δm denotes the FWHM of the peak in the mass spectrum.

windows there are fewer –if any– possible contaminant peaks, thus facilitating identification by mass in busy spectra and reducing possible probabilistic error contributions due to contamination by unknown and unresolved peaks.

The peak width of MR-TOF-MS TOF or mass spectra is determined by ion-optical properties of the MR-TOF-MS and the phase space of the analyzed ions. Procedures for tuning the ion optics of the FRS-IC MR-TOF-MS were already established prior to this work. These ensure that the time-energy focus is obtained on the detector regardless of the number of turns, *i. e.*, the TFS reflector and the MR-TOF-MS analyzer are tuned isochronous. In the following, the results of the two steps of the beam alignment outlined in the previous chapter will be presented. An aligned beam inside the MR-TOF-MS analyzer optimized the phase space and thus minimizes the peak width and consequently the statistical uncertainty.

3.1 Probing the Analyzer Center Position

To find the analyzer center position, times-of-flight TOF_0, $\mathrm{TOF}_{\mathrm{qp}}$ and count rates N_0, N_{qp} in pass through mode without and with quadrupolar field at the MRS, respectively, are measured in dependence of the two trap system (TS) steering voltages TS_Steer1 and TS_Steer2. The data was taken fully automatic using MAc with its improved voltage optimizer [Bergmann, thesis in preparation], using three loops for iterating the two steerer voltages and switching the quadrupole voltage. There were in total 270 spectra acquired for 135 different combinations of steering voltages, a screenshot of the program with the acquired data is given in Fig. C.1 in appendix C. The spectra contained about 200 ions on average, summing to 54 000 ions in total. The measurement time was about 5 hours, limited by the ramping speed of a power supply used for the quadrupolar voltage; this can be shortened in the future by supplying that voltage differently. The initial approach to probe the beam position was to observe shifts of the ions' time-of-flight due to the quadrupolar field, $\Delta\mathrm{TOF} = \mathrm{TOF}_0 - \mathrm{TOF}_{\mathrm{qp}}$. A quadrupolar-potential-like pattern was expected, but the data analysis had some difficulties and remaining open questions (appendix B), thus the count rates were used. In an ideal central hit, the count rates should not be affected by the quadrupole lens. To compare the count rates, a merit function with a single global maximum at $N_0 = N_{\mathrm{qp}}$ is needed. Let $\varepsilon = N_{\mathrm{qp}}/N_0$. Since $\varepsilon + \varepsilon^{-1} \geq 2$ for $\varepsilon > 0$ with equality only for $\varepsilon = 1$, the function

$$Q = 2/(\varepsilon + \varepsilon^{-1}) = 2/\left(\tfrac{N_{\mathrm{qp}}}{N_0} + \tfrac{N_0}{N_{\mathrm{qp}}}\right) \tag{3.2}$$

fulfills the above requirements. For equal counts, $Q = 1$ and if one count value is zero, Q is undefined, making it easier to use for a semi-automated

evaluation than the counts difference, for instance. In a real system the beam will be affected by the quadrupolar field even if it hits the analyzer center and there will be statistical fluctuations in addition. Still $Q \leq 1$ holds and Q as defined above has proven to be a robust measure for probing the beam position. The data is shown in Fig. 3.2. Q is constant and close to unity inside a rotated ellipse and then drops towards zero. The deviation from a rotational symmetric pattern and the angle are expected since the TFS reflector renders the system rotationally asymmetric and the TFS reflectors symmetry planes are rotated *vs* those of the quadrupole potential applied at the MRS, see Fig. 3.1. For the determination of the optimal steerer values (s_1, s_2), the plateau can be described by a woods-saxon like[2] function

$$f_{\mathrm{WS}}(r) = 1 - \frac{1}{1 + \exp\Big(-(r(x,y) - r_0)/w\Big)} \,. \tag{3.3}$$

The size of the plateau and the width of the slope of the drop to zero is parametrized by r_0 and w. For circular symmetry, the argument r would be the distance from the center (s_1, s_2), *i. e.* $r = r(x,y) = \|(x - s_1, y - s_2)\|_2$. Due to the broken symmetry, the distance needs to be modified by a rotation by an angle φ and deformation parametrized by α. The simplest area-preserving deformation in two dimensions is an elongation along one dimension by the factor α and a contraction by the same factor along the other dimension[3]. Hence the argument $r(x,y)$ to use in eq. (3.3) is given by shifting the center of the ellipse to the optimal steerer values and applying rotation and deformation, in compact notation the latter reads

$$r_{\alpha,\varphi}(x,y) = \left\| \begin{pmatrix} \alpha & 0 \\ 0 & 1/\alpha \end{pmatrix} \cdot \begin{pmatrix} \cos(\varphi) & -\sin(\varphi) \\ \sin(\varphi) & \cos(\varphi) \end{pmatrix} \cdot \begin{pmatrix} x \\ y \end{pmatrix} \right\|_2 . \tag{3.4}$$

The parameters of the function f_{WS} (eq. 3.3) with $r(x,y) = r_{\alpha,\varphi}(x - s_1, y - s_2)$ (eq. 3.4) are r_0, w, α, φ, s_1 and s_2. They were fitted to the data with the least-squares method using the Levenberg-Marquard algorithm [Moré, 1978] in the software package R [R Core Team, 2021; Elzhov *et al.*, 2016]. Fig. 3.2 also shows the results of this fit. An earlier version of this method was used for the first step of the previously described beam alignment procedure.

The thus found steering voltages lead to an optimal injection of the ions into the analyzer, *i. e.*, such that they traverse the analyzer center plane (where the position was probed) going through the optical axis. In the next step, these voltages are used to completely align the beam inside the analyzer by removing the tilt, *i. e.*, the angles under which they cross the optical axis in the analyzer center plane.

[2]here a purely phenomenological choice

[3]This turns circles $r^2 = x^2 + y^2$ into ellipses $r^2 = x^2/\alpha^2 + y^2\alpha^2$

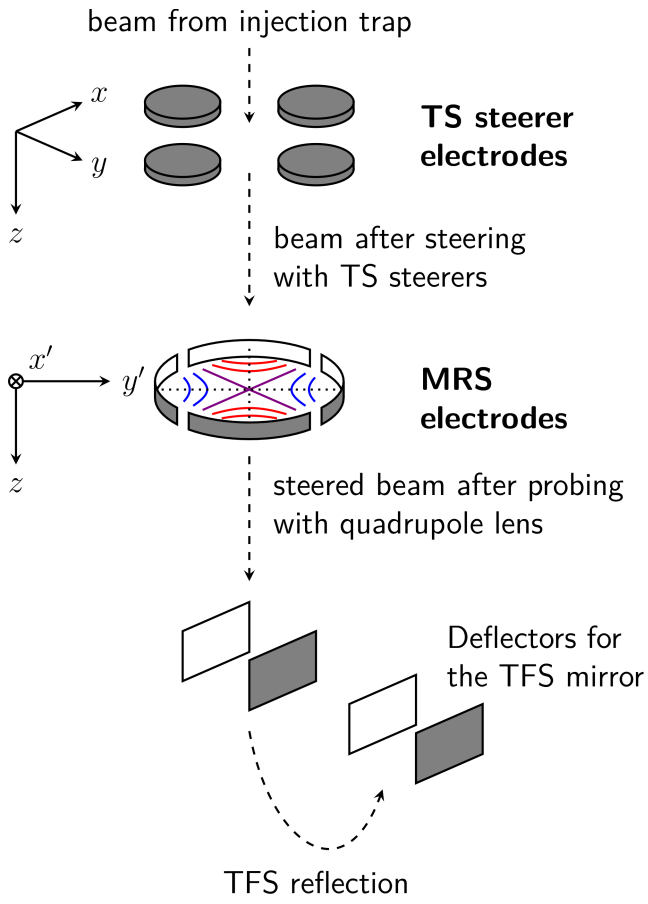

Figure 3.1: Sketch of the beam alignment using the TS steering and the MRS electrodes. The TFS reflection is also sketched. The electrode sizes are not to scale. Ions are injected from the top along the z direction, as indicated. The orientation of the x and y directions is given by the symmetry plane $x = 0$ of the MR-TOF-MS including the TFS reflection. The (x', y', z) coordinate system is rotated by 45° around the z axis, $x' = 0$ and $y' = 0$ are the symmetry planes of the quadrupolar field at the MRS, indicated by dotted lines. Equipotential lines of an ideal quadrupolar potential $V \sim x'^2 - y'^2 = 2xy$ in the MRS plane are sketched in blue and red for the different signs of the potential.

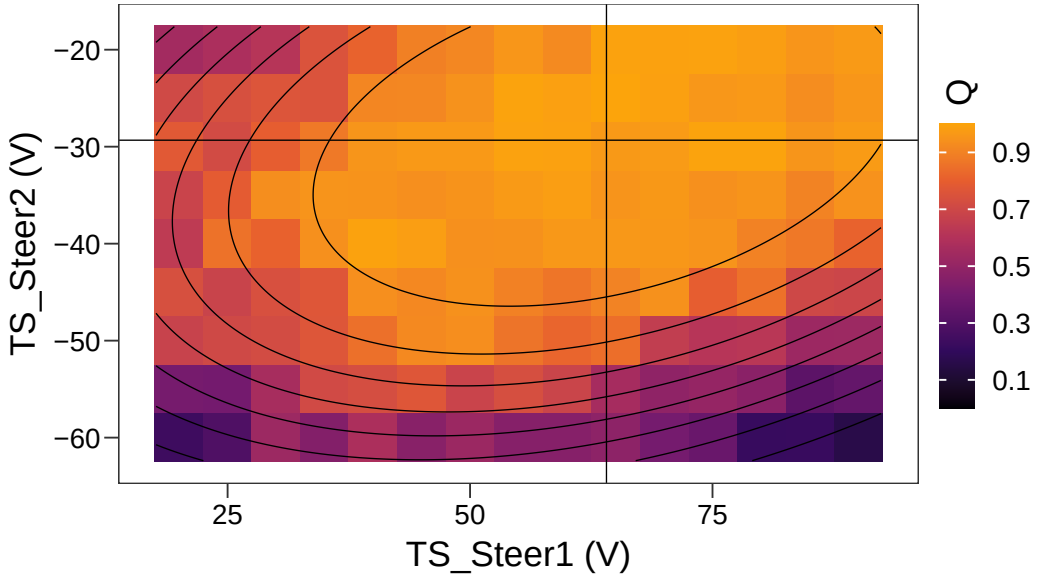

Figure 3.2: Merit function Q *vs* TS steerer voltages. Colored tiles show experimental data, the black ellipses are constant-Q lines from a fit of the two-dimensional rotated and deformed plateau function (eqns. (3.3) and (3.4)) to the data. The straight black lines cross at the fitted optimum.

3.2 Removing the Tilt

After the beam is steered to hit the analyzer center, the remaining tilt has to be removed. This is achieved by minimizing the TOF peak width in a high number of turns, *i. e.*, such that spatial aberrations significantly broaden the TOF peak. Thus the peak widths were recorded after 250 turns in dependence of the two MRS steering voltages MRS_Steer1p and MRS_Steer2p. Again, data was taken fully automatic using MAc with its improved voltage optimizer [Bergmann, thesis in preparation], using two loops for iterating the two steerer voltages. There were in 441 spectra acquired for different combinations of steering voltages, a screenshot of the program with the acquired data is given in Fig. C.2 in appendix C. The acquisition was run overnight in about 14.5 hours.

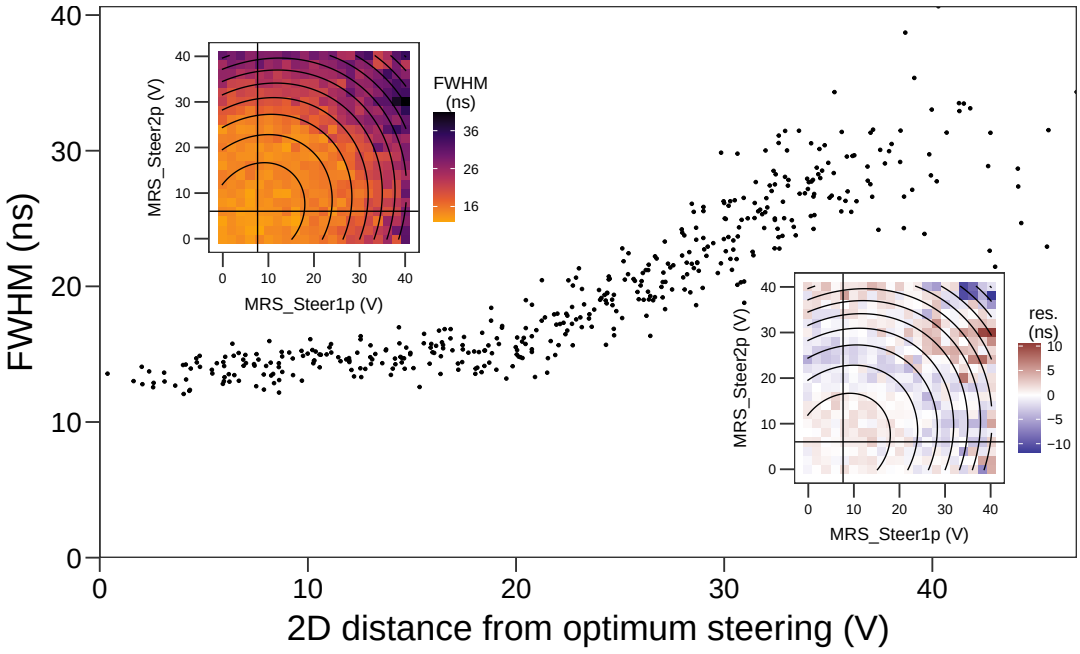

Figure 3.3: Experimental peak width data *vs* steering voltages at the MRS. The top left inset shows the peak width in color code with black elliptic contour lines from fitting a parabola to the data, the bottom right inset shows the respective fit residuals with the same contour lines. The straight black lines in the insets cross at the fitted optimum steerer values. The main plot shows the peak width *vs* the Euclidean distance of the steering voltages from the fitted optimum. The 441 data points represent 330 ions on average, summing to about 150 000 ions total.

For finding optimal steering voltages (s_1, s_2), a two-dimensional parabola can be fitted to the peakwidth data. Using the above rotated and deformed distance argument $r_{\alpha,\varphi}(x, y)$ (eq. (3.4)), the general two-dimensional parabola can be defined as

$$f(x, y) = a_0 + \frac{a_2}{2}\Big(r_{\alpha,\varphi}(x - s_1, y - s_2)\Big)^2, \tag{3.5}$$

with parameters a_0, a_2, α, φ, s_1 and s_2. They were fitted to the data with the least-squares method using the Levenberg-Marquard algorithm [Moré, 1978] in the software package R [R Core Team, 2021; Elzhov *et al.*, 2016]. The data and contours of the fit are shown in the top left inset of Fig. 3.3. This model allows a rotationally asymmetric pattern although less asymmetry is expected after the high number of turns and the thereby mixed phase space. This is seen in the fit results in that the fitted deformation parameter is almost unity, $\alpha_{\text{fit}} = 1.08 \pm 0.02$. The near symmetry motivates observing the data as in the main plot in Fig. 3.3, *i. e.*, with the peakwidth shown *vs* the distance from the optimal steerer voltages neglecting the orientation. The quantitative behavior can be well seen in this representation, and it can be observed that the peak broadening has two different regimes, from 20 V offset steering voltage onward the peak is broadening with a steeper slope. This change of slope shows that the parabola used for the fit is just a model and is reflected in the colormap plots by the ring structure in the residuals, see bottom right inset of Fig. 3.3. From SIMION simulations investigating the change of the beam inclination $a = v_x/v_z$ (with z denoting the optical axis and x one perpendicular axis) in dependence of the steering voltage at the MRS, it was found that at this steering voltage the change in mean a is about half the FWHM of its distribution for typical values of the system. For practical purposes, this demonstrates that the MRS steerers need to be varied over a range of about 40 V to be able to fit optimum steering values.

3.3 Resulting Mass Resolving Power

Indeed, with the systematic tuning, a mass resolving power of $R = 1 \times 10^6$ could be reached repeatedly. A typical spectrum with ions from an internal source is shown in Fig. 3.4, the dependence of the mass resolving power *vs* the number of isochronous turns in this tune is plotted in Fig. 3.5. It was first reached when establishing the procedure [Will, 2019], second during preparations for the 2019 GSI FRS Engineering run and third in the preparations of the 2020 FRS experiments focusing on the proton-neutron interaction strength around the $N = Z$ line below ^{100}Sn [Mardor *et al.*, 2021] and on nuclear structure in this region [Kripkó-Koncz, thesis in preparation]. The latter measurements had

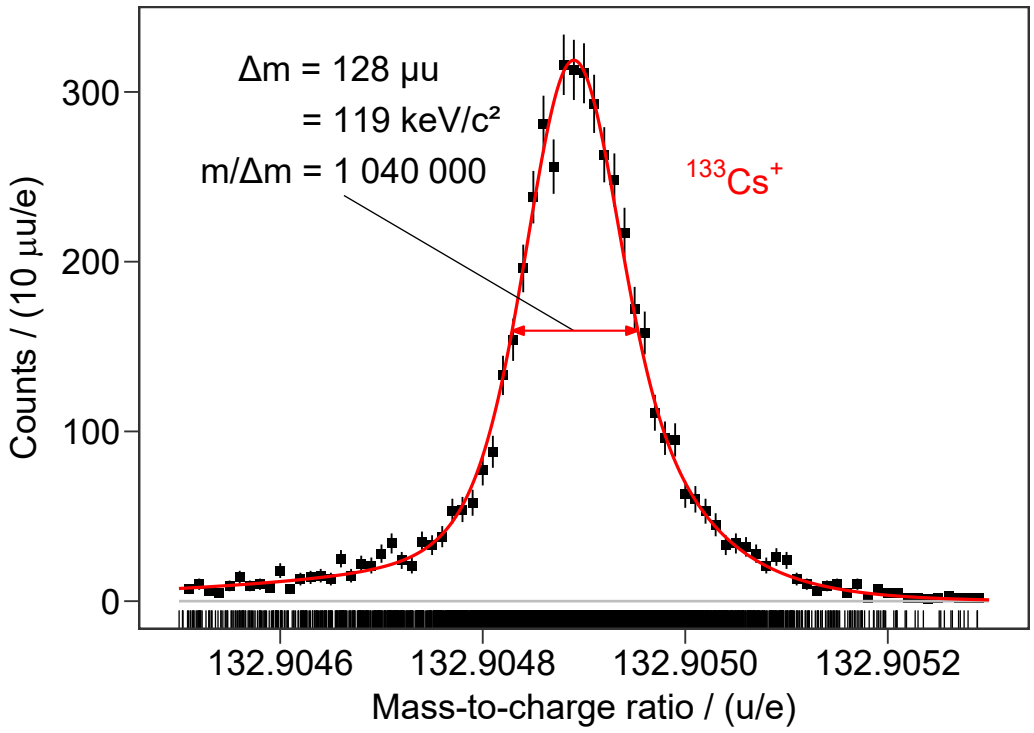

Figure 3.4: Mass spectrum demonstrating the mass resolving power $R = 1\,040\,000$ with 5400 ^{133}Cs ions from an internal source acquired in 20 min. The solid red line is a hyper-EMG fit to the data.

to be performed with a workaround in the trap system of the MR-TOF-MS due to an electrical short between a steering electrode and an adjacent aperture, reducing the safe range of steering voltages for the beam alignment and possibly affecting the stability of the steering voltages.

The strength of the beam alignment method previously presented is its systematic repeatability. Consequently in 2020 a mass resolving power of

$$R = 970\,000 \text{ during experiment S474}$$

was achieved with 256 events for the neutron deficient exotic nucleus ^{70}Se in a 895 IT setting. The total uncertainty in this measurement amounted to 2.6 keV for a total number of 485 events recorded with different turn number settings [Mardor *et al.*, 2021]. The respective spectra are shown in Fig. 3.6. In the same experiment, the mass of ^{69}As was measured with an uncertainty of 22 keV with only ten events, which was possible only due to the ultra high resolving power of 870 000. Furthermore, the $A = 69$ molecule ^{14}N^{15}N^{40}Ar was extracted from the CSC in these measurements and its mass was determined with a relative mass uncertainty of 1.7×10^{-8}, which is an unprecedented accuracy for MR-TOF-MS to date [Mardor *et al.*, 2021].

The results both with stable isotopes from internal sources and unstable isotopes produced in the FRS outperform the previous world record of $R \gtrsim 600\,000$ [Dickel, 2010; Ayet San Andrés, 2018] obtained with stable isotopes. Many parts of the FRS-IC have been improved throughout the years, however this is the first significant improvement in resolving power after about ten years. The repeatability of the tuning procedure and the use of automatic parameter scans in MAc furthermore allowed the direct application to exotic isotopes. Consequently in the ^{70}Se measurement, the previous best value for measurements with exotic nuclei at the FRS-IC, $R \approx 450\,000$ [Hornung *et al.*, 2020], is more than doubled. This and the reduced background due to the narrower TOF window extends the reach of the present FRS facility with the FRS-IC. A factor 2 in resolving power is in the statistical uncertainty equivalent to a factor 4 in the number of events [eq. 3.1], the reduced background makes mass measurements with fewer ions possible and reduces probabilistic uncertainty components due to unknown and unresolved peaks. On can thus expect to measure masses of nuclei with one order of magnitude lower yield without sacrificing uncertainty.

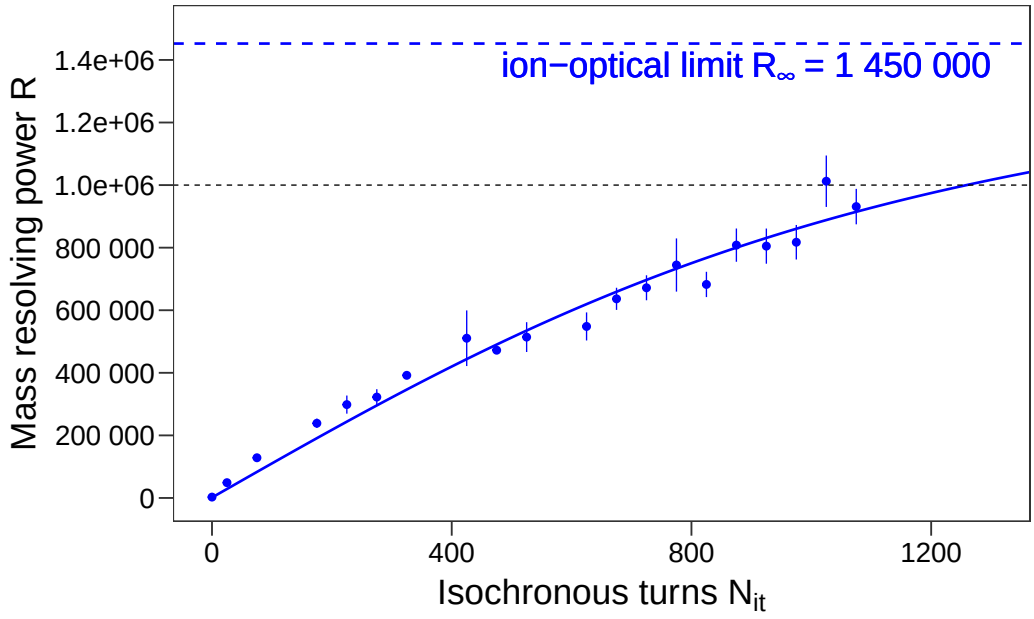

Figure 3.5: Mass resolving power *vs* number of isochronous turns. The systematic data was measured while establishing the tuning procedure [Will, 2019]. Hyper-EMG peaks were fitted to the TOF data, the plotted errors are obtained from the fit. The thin black dashed line indicates $R = 1 \times 10^6$. The solid blue line is a fit of the theoretical curve (eq. 1.30), the asymptotic limit of the resolving power determined by this fit is $R_\infty = 1\,450\,000$, indicated by the dashed blue line.

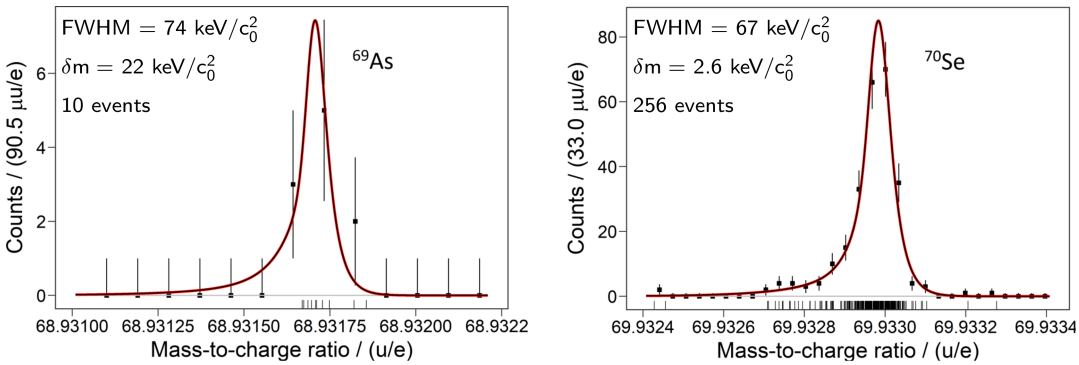

Figure 3.6: Mass spectra of ^{69}As (left) and ^{70}Se (right) measured at the FRS-IC with mass resolving powers of 870 000 and 970 000, respectively. Figures from [Mardor *et al.*, 2021]. The uncertainty of the mass value of ^{70}Se includes another measurement with a different turn number and corresponds to 485 events in total.

Chapter 4

Mass Selective Re-trapping

In this work, mass-selective re-trapping was established for isobar separation in the MR-TOF-MS at TRIUMF's Ion Trap for Atomic and Nuclear sciences (TITAN). It was used to enable and perform mass measurements for exotic nuclei which were so far hampered by isobaric contamination (chapter 5). In this chapter, the TITAN setup is introduced and mass-selective re-trapping is described and the performance of the technique as used in the mass measurements is quantified.

4.1 The TITAN Setup

TITAN is a multiple ion trap setup for ion preparation, manipulation and ultra high-precision mass measurements and decay spectroscopy of singly and highly charged ions [Dilling *et al.*, 2006]. An MR-TOF Mass Spectrometer and Separator developed by the IONAS group has been added in year 2014 [Jesch *et al.*, 2015; Dickel *et al.*, 2019a] for mass measurements, beam diagnostics [Reiter *et al.*, 2020] and purification. TITAN uses the secondary beam delivered by ISAC (sec. 1.3.2), the TITAN MR-TOF-MS was first used with secondary beam in the year 2017. This beam is cooled and bunched in an RFQ filled with helium gas [Brunner *et al.*, 2012], energy-matched with a pulsed drift tube, and further delivered either to the MR-TOF-MS for direct mass measurements or purification or to the Penning trap setup for mass measurements, possibly after charge state breeding.

The TITAN MR-TOF-MS uses the same TOF analyzer design as the FRS-IC MR-TOF-MS but is scaled in size and has a different beamline and trap system, as well as no TFS reflector. It consists of a capturing unit for the incoming beam, an RFQ beamline filled with helium gas including an RFQ switchyard for extracting the purified beam towards the Penning traps, an RF injection

trap, a coaxial TOF analyzer using two electrostatic reflectors, an MRS and an ETP MagneTOF detector mounted at the exit of the TOF analyzer. The ISAC beam is usually attenuated in the ISAC beamline to an intensity that there is a maximum of about one ion detected with the MagneTOF per species per cycle to avoid deterioration of the mass measurement accuracy due to ion-ion interactions. For direct mass measurements, the procedure is similar to the one at the FRS-IC. Ions are cooled in the injection trap and stored in the analyzer by switching the reflectors to a high potential. After many reflections leading to

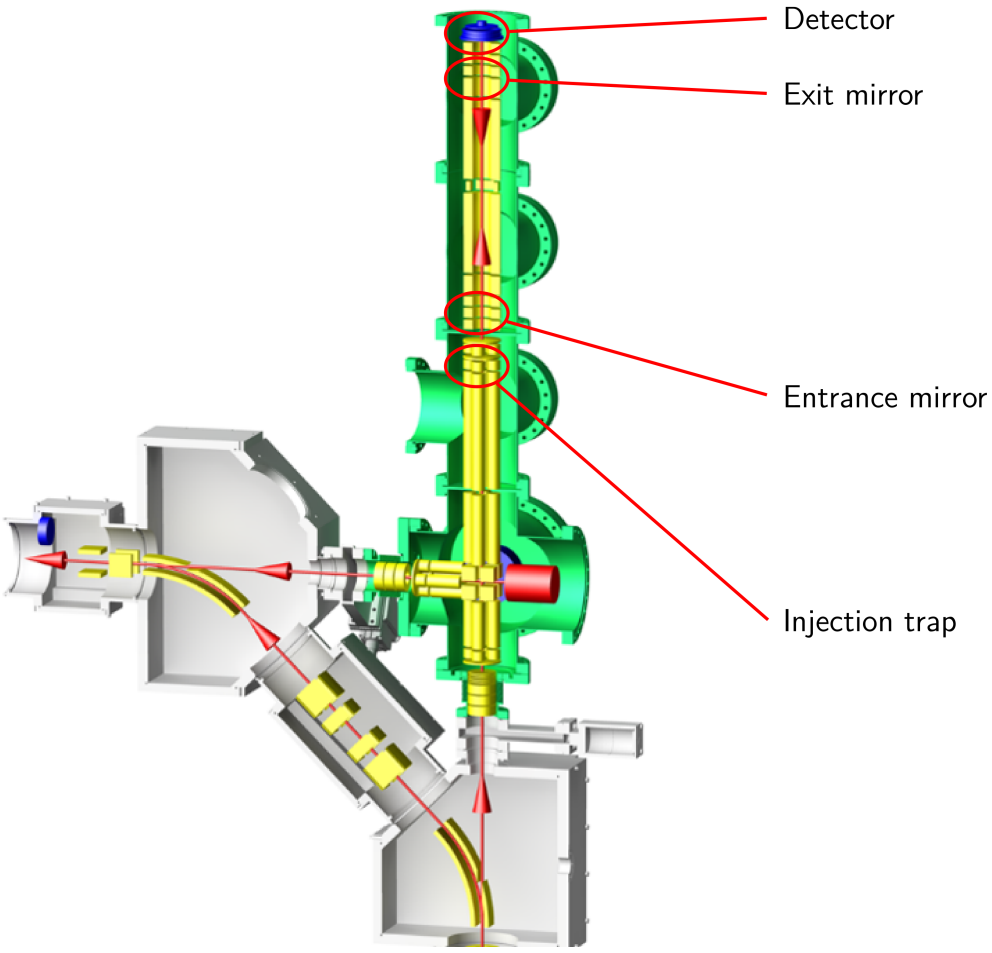

Figure 4.1: Schematic view of the TITAN MR-TOF-MS. Exotic isotopes enter the MR-TOF-MS coming from the TITAN RFQ cooler buncher from below, are captured and transported through an RFQ beamline into the injection trap. There they are cooled and injected into the TOF analyzer for mass analysis, for details see sec. 1.4.1. The injection trap is also used for mass selectively re-trapping ions after TOF dispersion, for details see text.

sufficient TOF dispersion, the exit reflector is pulsed to a low potential and the ions impinge on the detector. The MRS of the TITAN MR-TOF-MS is usually operated such that there is only one atomic mass unit transmitted. Since there is no dedicated TFS reflector installed behind the analyzer of the TITAN MR-TOF-MS, to achieve resolving powers as high as possible the time focus has to be shifted to the detector by different means. At the TITAN MR-TOF-MS, this is achieved by using dynamical time-focus shift with the analyzer with one time-focus shift turn (TFST) before the ions undergo a number of isochronous turns (ITs) [Dickel *et al.*, 2017a, Sec. 1.4.1]. The TFST increases the systematic error of mass measurements compared to the FRS-IC setup, as all analyzer voltages are pulsed during the time the ions spend in the TOF analyzer.

The TITAN MR-TOF-MS was build and initially commissioned at Gießen by C. Jesch [Jesch *et al.*, 2015; Jesch, 2016]. It was then transported to Vancouver and re-commisioned for the TITAN experiment by S. Ayet San Andrés, A. Finlay, C. Hornung, M. P. Reiter, D. Short and C.Will [Will, 2017; Ayet San Andrés, 2018; Reiter *et al.*, 2020]. The first measurements with exotic ions were reported by Leistenschneider *et al.* [2018]. Re-trapping was commissioned with the TRIUMF Off-Line Ion Source prepared prior to the experiment described in chapter 5 by A. Jacobs and M. P. Reiter [Jacobs, 2019]. Here, mass-selective re-trapping is characterized in an analytical model and applied for measurements of exotic nuclei for the first time.

4.2 Mass Selective Re-Trapping with the TITAN MR-TOF-MS

A major challenge for experiments with exotic nuclei at ISOL facilities is isobaric contamination (sec. 1.3). Nuclei closer to stability are produced with rates many orders of magnitude higher than those of the nuclei of interest. Furthermore, molecules can form and increase the amount of isobaric contamination. Due to the limited resolving power of existing magnetic separators at ISOL facilities, typically $m/\Delta m \sim 1000$, these contaminations hamper measurements of the exotic nuclei. Quantitatively, this was illustrated by Jesch *et al.* [2015] by defining a nuclide as accessible if it contributes to at least half of the beam current after separation and by calculating the number of these accessible nuclides in dependence of mass resolving power of the separator. The results of this investigation are shown in Fig. 4.2.

The novel method for mass separation in an MR-TOF-MS established here is the dynamical re-trapping of ions after the TOF dispersion procedure in the RF trap, from which they have been injected into the TOF analyzer. The system

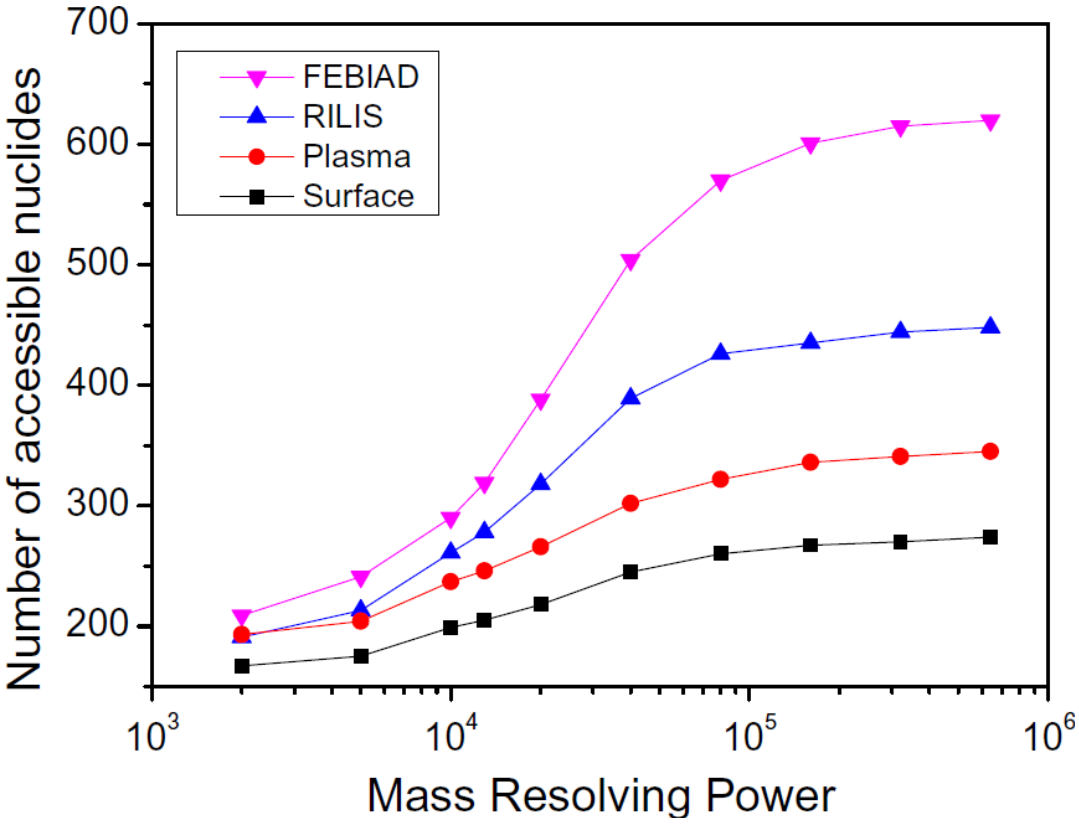

Figure 4.2: The number of accessible nuclides for different ion sources in dependence of the mass resolving power of the separator at ISOL facilities. A mass resolving power of more than 10 000 is necessary to significantly increase the number of accessible nuclides. Figure taken from [Jesch *et al.*, 2015], caption adapted from there. Details on the investigation can be found in the original publication. In this work, a mass resolving power of $R_{\text{sep, edge}} \approx 36\,000$ was reached with the edge (10–90%) of the re-trapping window.

can operate as its own isobar separator, as separator for the other traps (EBIT and Penning traps), or as separator for other experiments by injecting the cleaned beam back into the RFQ buncher and delivering it for example towards laser spectroscopy. The method was presented already earlier [Dickel *et al.*, 2017b], in this work the quantitative treatment is refined and the method is first applied for the separation of exotic isotopes in online experiments. Figure 4.3 shows a sketch of the different stages of the technique. When re-trapping is used, the usual measurement cycle is split in two parts, first re-trapping and then mass measurement. In the re-trapping part, after TOF dispersion of the ions in the analyzer, the entrance reflector is opened instead of the exit reflector, and the ions are dynamically and mass-selectively re-trapped in the injection trap. The time for TOF dispersion as set by the user is called re-trapping time t_{rt}. After re-trapping, the mass-selected ions are again cooled in the injection trap and injected once more into the TOF analyzer for the conventional mass measurement procedure. Quantitative characteristics of the mass separation by re-trapping and related measurements will be discussed in the following.

4.3 Re-trapping Efficiency and Mass Separation Power

For re-trapping, the ions are first slowed down in the RF trap and then the potentials of the trap are switched from retarding to trapping after the re-trapping time t_{rt}. To analyze the re-trapping window, consider the ion's actual re-arrival time, *i. e.*, the TOF after ejection when the ion comes to rest in the RF trap with retarding fields applied, t_{stop}, and the difference δ_{rt} of the set re-trapping time and the re-arrival time,

$$\delta_{\mathrm{rt}} = t_{\mathrm{rt}} - t_{\mathrm{stop}} \,. \tag{4.1}$$

For ideal re-trapping of a single ion species, $\delta_{\mathrm{rt}} = 0$. If several ion species need to be re-trapped and an isobaric contaminant needs to be suppressed, the window position and width needs to be known. Let us define the re-trapping efficiency $\varepsilon_{\mathrm{rt}} = \varepsilon_{\mathrm{rt}}(\delta_{\mathrm{rt}})$ as the fraction of re-trapped ions of a fixed mass-over-charge ratio m/q. Since δ_{rt} depends on m/q through $t_{\mathrm{stop}} = t_{\mathrm{stop}}(m/q)$, $\varepsilon_{\mathrm{rt}}$ also depends on m/q. $\varepsilon_{\mathrm{rt}}$ describes the impact of the set re-trapping time. It can be easily measured and is compared with model results.

Ions are separated according to their kinetic energies after the trap has been closed for re-trapping. $\varepsilon_{\mathrm{rt}}$ can be derived extending the quantitative treatment in [Dickel *et al.*, 2017b] by using the natural choices for the ions velocity dis-

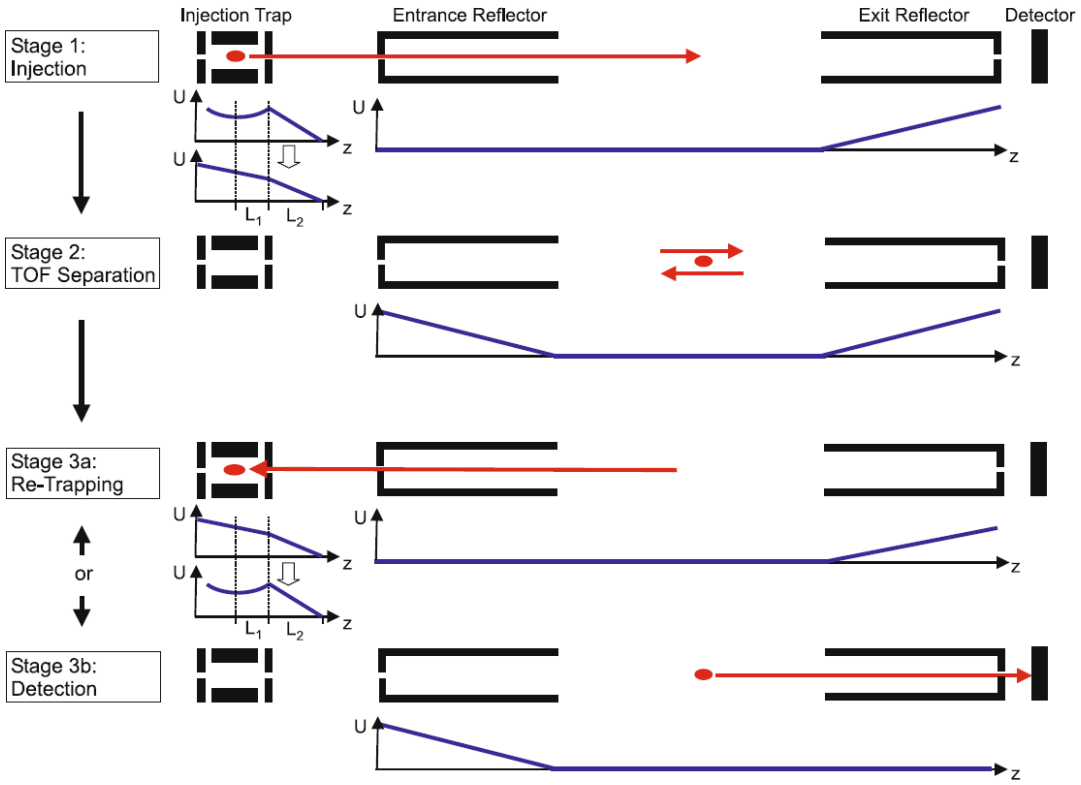

Figure 4.3: A Sketch of the re-trapping procedure from Dickel *et al.* [2017b], showing the different stages in an MR-TOF-MS mass measurement with re-trapping. Red dots and arrows indicate ion samples and ion movements, blue lines in the U *vs* z plots give an idea of the on-axis potential. The ions are first injected by switching the DC potentials of the injection trap from trapping to extraction. In the second stage, the ions separate in TOF inside the analyzer after the entrance mirror has been closed. Finally, either the entrance mirror is opened and the trap later closed again, both at times tuned for the ions which should be re-trapped, or the exit mirror is opened for detection. If in the third stage re-trapping is done, Stages one to three can be repeated, for a direct mass measurement or an additional separation cycle.

tribution and the traps velocity acceptance[1]. The initial velocity spread of the ions with charge and mass q and m, respectively, is due to thermal distribution with width $\Delta v_{\mathrm{thermal}}$. It is converted into an initial TOF spread at the first time focus given by the turn-around time Δt_{ta} after extraction with extraction field E_{ex} via $\Delta t_{\mathrm{ta}} = \frac{m}{qE_{\mathrm{ex}}}\Delta v_{\mathrm{thermal}}$. For their velocity spread at arrival after slowing down with retarding field E_r, the formula $\Delta v = (qE_r/m)\Delta t$ approximately holds, with the ions' time spread Δt at the last time-focus under the assumption that the respective plane coincides with that of the first time-focus. This approximation is assuming a simple time-reversal. It is thus neglecting ion-optical aberrations, which for instance lead to velocity-dependent additional time-spreads not covered by the simple algebraic formula inversion. Consequently, deviations between model and measurements of quantities related to the velocity spread at re-arrival are expected. To arrive at an analytical expression for $\varepsilon_{\mathrm{rt}}$, we first assume a Gaussian distribution[2] for v with density function $f_{v;\delta_{\mathrm{rt}}}$. Width and mean are derived from the TOF distribution at the final time-focus,

$$\sigma_v = \frac{qE_r}{m}\sigma_t \tag{4.2}$$

$$\langle v\rangle(\delta_{\mathrm{rt}}) = \frac{qE_r}{m}\delta_{\mathrm{rt}}\,. \tag{4.3}$$

Widths denoted with Δ, like Δv and Δt, are FWHM while σ denotes standard deviations[3], *e. g.*, σ_v and σ_t. Ions are re-trapped if $|v| < v_{\mathrm{max}}$, *i. e.*, the velocity acceptance is assumed uniform inside $[-v_{\mathrm{max}}, v_{\mathrm{max}}]$. The maximal velocity v_{max} is determined from energy conservation using the depth of the on-axis potential well ΔU_r,

$$v_{\mathrm{max}} = \sqrt{\frac{2q\Delta U_r}{m}}\,. \tag{4.4}$$

The fraction of re-trapped ions is

$$\begin{aligned}\varepsilon_{\mathrm{rt}}(\delta_{\mathrm{rt}}) &= \int_{-v_{\mathrm{max}}}^{v_{\mathrm{max}}} f_{v;\delta_{\mathrm{rt}}}(v')\,\mathrm{d}v' \\ &= \int_{-v_{\mathrm{max}}}^{v_{\mathrm{max}}} \exp\left(-\frac{(v'-\langle v\rangle(\delta_{\mathrm{rt}}))^2}{2\sigma_v}\right)\frac{1}{\sqrt{2\pi\sigma_v^2}}\,\mathrm{d}v'\end{aligned} \tag{4.5}$$

[1]Natural choice means that there is no more information used than available, *i. e.*, the distribution with maximum entropy under the given constraints is used. If we take mean and standard deviation of the velocity distribution as given, a Gaussian is the natural choice. If we take the range of the velocity acceptance as given, a uniform acceptance is the natural choice.

[2]A generalization is only needed for edge separation or narrow re-trapping windows.

[3]Standard deviations are more convenient when dealing with integrals and quantiles of Gaussians, results are usually given in FWHM.

The integral can be solved and written as a difference of error functions (eq. 4.9 in time representation below). It can be visualized, see Fig. 4.4 for the case $\sigma_v \ll v_{\max}$. The expected properties of $\varepsilon_{\mathrm{rt}}$ can be directly seen from the sketch

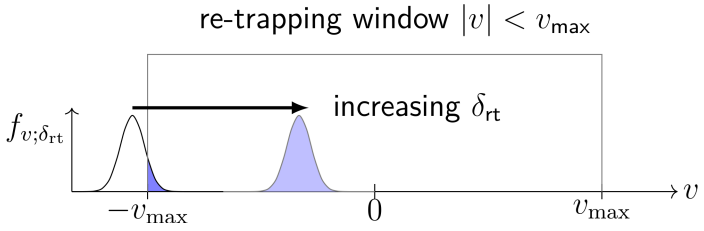

Figure 4.4: Visualization of the integral for $\varepsilon_{\mathrm{rt}}(\delta_{\mathrm{rt}})$. The blue shaded areas describe the amount of re-trapped ions. With increasing δ_{rt}, ions are re-trapped while they are decelerated, stopped, and re-accelerated.

or the integral; it is increasing with δ_{rt} for $\delta_{\mathrm{rt}} < 0$, has its maximum at $\delta_{\mathrm{rt}} = 0$ and then decreases. The maximum of $\varepsilon_{\mathrm{rt}}$ is

$$\varepsilon_{\mathrm{rt;max}} = \mathrm{erf}\left(\frac{v_{\max}}{\sqrt{2\sigma_v^2}}\right) = \mathrm{erf}\left(\sqrt{\ln(2)}\frac{\Delta v_r}{\Delta v}\right), \tag{4.6}$$

with the velocity acceptance width $\Delta v_r = 2v_{\max}$ and the width of the velocity distribution $\Delta v = 2\sqrt{2\ln 2}\sigma_v$. It is clear from the sketch and can easily be shown from the integral that the width of the re-trapping window in velocity representation Δv_{rt} tends to Δv for $\Delta v \gg \Delta v_r$ and to Δv_r for $\Delta v \ll \Delta v_r$,

$$\lim_{\frac{\Delta v_r}{\Delta v}\to 0} \Delta v_{\mathrm{rt}} = \Delta v \tag{4.7}$$

$$\lim_{\frac{\Delta v_r}{\Delta v}\to \infty} \Delta v_{\mathrm{rt}} = \Delta v_r\,. \tag{4.8}$$

In the first case, the maximum of the re-trapping efficiency tends to zero while in the latter it is 100 %. The asymptotic behavior can be described to some extent by quadratically adding the widths as suggested by Dickel *et al.* [2017b] including the corrections below, but this is overestimating the width strongly in the transition region $\Delta v_r \approx \Delta v$ and already for $\Delta v_r \geq 2\Delta v$ the simple approximation $\Delta v_{\mathrm{rt}} \approx \Delta v_r$ is more accurate [Fig. 4.5]. In time representation, the solution of the re-trapping window integral is obtained from the transformation (4.3) and by employing eq. (4.4),

$$\varepsilon_{\mathrm{rt}}(\delta_{\mathrm{rt}}) = \frac{1}{2}\left[\mathrm{erf}\left(\frac{\delta_{\mathrm{rt}}}{\sqrt{2\sigma_t^2}} + \sqrt{\frac{m\Delta U_r}{qE_r^2\sigma_t^2}}\right) - \mathrm{erf}\left(\frac{\delta_{\mathrm{rt}}}{\sqrt{2\sigma_t^2}} - \sqrt{\frac{m\Delta U_r}{qE_r^2\sigma_t^2}}\right)\right] \tag{4.9}$$

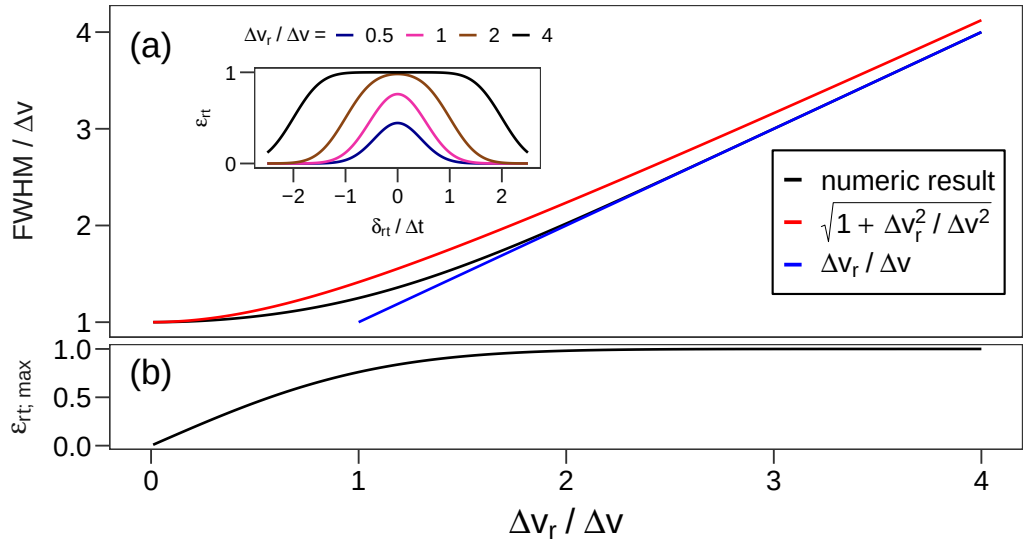

Figure 4.5: (a) Width of the re-trapping window normalized to the velocity width computed numerically from the presented model (black), with quadratic addition (red) and the $\Delta v \ll \Delta v_r$ asymptotic behavior (blue). (b) Maximum relative re-trapping efficiency. The inset in (a) shows the re-trapping window for different $\Delta v/\Delta v_r$ ratios. For $\Delta v/\Delta v_r \leq 1$ the maximum continuously decreases while the width approaches its finite minimum given by the ions velocity distribution.

For the case $\Delta v \ll \Delta v_r$, the window width is

$$\Delta t_{\mathrm{rt}} = \sqrt{\frac{8m\Delta U_r}{qE_r^2}} \qquad \text{(FWHM)}. \tag{4.10}$$

Only the uniform velocity acceptance and the relation $\Delta v \ll \Delta v_r$ are needed to derive eq. (4.10), it is thus applicable for other velocity distributions, *e. g.*, including tails due to collisions with buffer gas or ion-optical aberrations.

For $\Delta v \ll \Delta v_r$ ions of different species can well be separated by the edge of the re-trapping window. We define the edge separation power via the rise time, *i. e.*, the time difference over which $\varepsilon_{\mathrm{rt}}$ changes from 10% to 90%. Close to the edges of the re-trapping window, the ions velocity is close to $\pm v_{\max}$. Because $\Delta v \ll \Delta v_r$, the integrand in (4.5) is negligible around the other limit $\mp v_{\max}$ and this limit can be extended to $\mp\infty$. The relative re-trapping efficiency can hence for the rising edge be described by

$$\varepsilon_{\mathrm{rt}}(\delta_{\mathrm{rt}}) \approx \int_{-v_{\max}}^{\infty} \exp\left(-\frac{(v' - \langle v\rangle(\delta_{\mathrm{rt}}))^2}{2\sigma_v}\right) \frac{1}{\sqrt{2\pi\sigma_v^2}}\,\mathrm{d}v'\,. \tag{4.11}$$

The rise time can then be determined from the 10-th and 90-th percentile $p_{10\%}$ and $p_{90\%}$ of a Gaussian distribution. These can be scaled from the standard normal distribution percentiles, which are readily available in contemporary numerical software. In time representation, the result is

$$\Delta t_{\mathrm{rt;\,edge}} = (p_{90\%} - p_{10\%})\sigma_t \approx 2.56\,\sigma_t \approx 1.09\Delta t \quad (10\text{–}90\%). \tag{4.12}$$

In the limit $\Delta v \gg \Delta v_r$, no transmission plateau is formed and separation is always affected by the edge. An interesting limiting case is the lowest achievable width, *i. e.*, the highest achievable separation power, without sacrificing efficiency. As seen in Fig. 4.5(b), this corresponds to $\Delta v_r = 2\Delta v$, or equivalently $v_{\max} = \Delta v$, with a re-trapping efficiency in the center of the re-trapping window of $\varepsilon_{\mathrm{rt;max}} = 98\%$. This is on the onset of a plateau being formed and the approximation of the window FWHM with Δv_r is already valid, so the width in time is

$$\Delta t_{\mathrm{rt}} \approx 2\Delta t \qquad (\mathrm{FWHM}), \tag{4.13}$$

which can be understood simply as two sided version of the edge separation.

The model developed here can be generalized in a straightforward manner when the velocity distribution is known with more details, for the edge separation power for instance this only requires using the respective percentiles. Furthermore it can be used for other separation methods, like separation with a Bradbury-Nielsen gate [Plaß *et al.*, 2008] after TOF dispersion in an MR-TOF-MS.

4.4 Comparison with Experimental Data

Dickel *et al.* [2017b] investigated the re-trapping separation power systematically with a model where the width of the re-trapping window in velocity representation was obtained from quadratically adding the widths of the velocity distribution and the velocity acceptance window. The data was taken with an MR-TOF-MS of the same analyzer geometry as the TITAN MR-TOF-MS [Lang, 2016]. To estimate the quality of a model fitted to observed values, the chi-square like value $\tilde{\chi}^2 = \sum_i (O_i - f(\mathbf{x}_i))^2 / f(\mathbf{x}_i)^2$ can be used, where the model function f predicts values from parameters (or independent variables) $\mathbf{x}_i$ associated with the i-th observed value (or dependent variable) O_i. Here, measured and modeled separation powers $R_{i,\mathrm{sep}}$ and $R_{i,\mathrm{sep;\,model}}$ are compared, thus $\tilde{\chi}^2 = \sum_i (R_{i,\mathrm{sep}} - R_{i,\mathrm{sep;\,model}})^2 / R^2_{i,\mathrm{sep;\,model}}$. To obtain a good fit of experimental values to the model in [Dickel *et al.*, 2017b], by minimizing $\tilde{\chi}^2$, two adjustments need to be made. Firstly, the depth of the re-trapping potential well has to be reduced by a constant offset of 1.15 V compared to the values calculated from

the applied potentials. This adjustment can be understood since deviations of the real on axis trap depth can be expected, *e. g.*, due to the RF field, which may have a residual component on axis. Secondly, the retarding field strength needs to be scaled by 0.56, which was at the time of writing that paper not understood. With these adjustments, the chi-square like value was $\tilde{\chi}^2 = 0.2$ with 24 observations and two parameters. However, in that investigation, the factor two was missing in the width of the velocity acceptance window,

$$\Delta v_r = 2 v_{\max} \,, \tag{4.14}$$

which is obvious in the model presented above. By just taking this factor into account and only allowing the trap depths to be adjusted globally, the experimental data could be fitted obtaining $\tilde{\chi}^2 = 0.3$ with the same offset of 1.15 V for the re-trapping potential well depth.

With the simple model employing velocity distributions, which was analytically discussed here in some detail, mass selective re-trapping can be understood more detailed. Since separation is often done with the edge of the re-trapping window, the model matches practical operation very well. It is in the following compared to experimental data from the measurements during and in preparation of the experiment described in chapter 5. For this experiment, the apertures surrounding the injection trap were set 12 V above the RF DC average for re-trapping, resulting in a trap depth of $\Delta U_r = 6.3\,\mathrm{V}$, determined using SIMION [Manura, D. and Dahl D., 2008]. This corresponds to $v_{\max} = 3\,\mathrm{mm\,\mu s^{-1}}$ for $^{133}\mathrm{Cs}^+$. The retarding field strength was also determined using SIMION and the respective set voltages to $E_r = 86.1\,\mathrm{V\,mm^{-1}}$. For $^{133}\mathrm{Cs}^+$, the peak width on the detector after 50 IT was measured as 8.7 ns (FWHM). This corresponds to an approximate velocity spread of $\Delta v = 0.54\,\mathrm{mm\,\mu s^{-1}}$ (using the transformation in eq. (4.3) which is neglecting additional broadening due to ion-optical aberrations), hence the condition $\Delta v \ll \Delta v_r$ is fulfilled. Since the calculation of the velocity width neglects broadening due to ion-optical aberrations, it is expected that the experimentally measured rise time is larger than predicted from the TOF peak width at the detector. Furthermore, as argued above, deviations of the real on-axis trap depth can be expected. A measurement with re-trapping after 30 IT with six different trap depths was fitted to the model to quantify these adjustments. From this data, a dimensionless correction factor for the rise time of 1.52 and an offset for the re-trapping potential well depth of 1.7 V could be determined. The model estimates for the re-trapping window FWHM and edge width without and with correction are

$$\Delta t_{\mathrm{rt;model}} = 97\,\mathrm{ns} \quad \text{and} \quad \Delta t_{\mathrm{rt,edge;model}} = 9\,\mathrm{ns} \tag{4.15}$$

$$\Delta t_{\mathrm{rt;adj.\ model}} = 82\,\mathrm{ns} \quad \text{and} \quad \Delta t_{\mathrm{rt,edge;adj.\ model}} = 14\,\mathrm{ns}\,. \tag{4.16}$$

Fig. 4.6 shows a comparison between model and experimental data. The function given in (4.9) was fitted to the measured data once unconstrained and once adjusted as described above, *i. e.*, the width and rise time (corresponding to Δv_r and Δv) were once (in the unconstrained case) fitted and once kept constant at their adjusted model value. Window position t_{rt} and height were fitted in both cases. In the unconstrained fit to the data, experimental values for the re-trapping window FWHM and edge width

$$\Delta t_{\mathrm{rt;exp.}} = 85\,\mathrm{ns} \quad \text{and} \quad \Delta t_{\mathrm{rt,edge;exp.}} = 16\,\mathrm{ns} \tag{4.17}$$

were obtained, in excellent agreement with the results of the adjusted model (eq. 4.16). The center of the re-trapping window is at $t_f(^{133}\mathrm{Cs}^+, 50\mathrm{IT}) = 1185.803(1)\,\mu\mathrm{s}$ (uncertainty from the fit), whereas the estimated one was 1185.732(7) µs (uncertainty from the visual determination of the window edges) from preparations with ions from internal sources. From this, an offset of +72(7) ns of the real re-trapping time minus the predicted re-trapping time could be deduced. This is an impressive agreement, and the analysis presented here can be used to even improve the preparation for future experimental campaigns using the TITAN MR-TOF-MS as separator.

Experimental width and rise time correspond to mass separation powers

$$R_{\mathrm{sep}} \approx 7000\ (\mathrm{FWHM}) \text{ and } R_{\mathrm{sep,\ edge}} \approx 36\,000\ (10\text{–}90\%)\,. \tag{4.18}$$

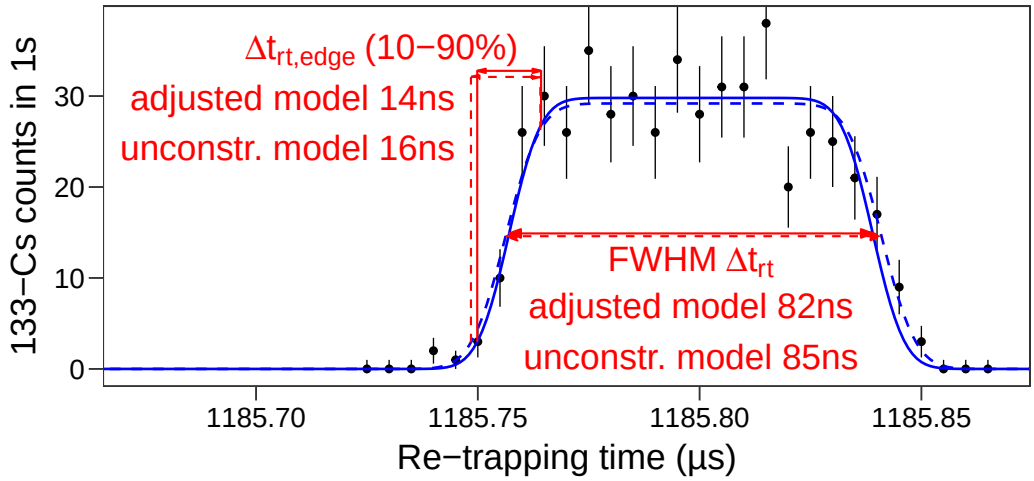

Figure 4.6: Counts of $^{133}\mathrm{Cs}^+$ *vs* re-trapping time. The ions performed 50 IT in the analyzer before being re-trapped. The solid blue line is an adjusted model fit (eq. (4.9)) with width and rise time fixed but adjusted. The dashed blue curve is an unconstrained fit, for details see text.

Both are much larger than the separation power of the ISAC magnet, typically $m/\Delta m \sim 2000$, thus mass selective re-trapping provides a significant improvement in separating ions under study from isobaric contamination. The ions of interest are transmitted for measurement with high efficiency ($\sim 60\%$) while the unwanted species, which occur much more abundantly and which are close in mass-to-charge ratio, are suppressed by several orders of magnitude. The mass separation power can be increased further, exceeding $R_{\mathrm{sep}} = 100\,000$ by increasing the number of turns before re-trapping and/or by decreasing the depth of the re-trapping potential well. The number of turns is limited by the duration of the measurement cycle and thus by the half-life of the ion of interest, the depth of the re-trapping potential well is limited by acceptable efficiency losses, and more reduction will render the ions velocity spread the limiting factor (compare Fig. 4.5).

Re-trapping was tested with an isobaric beam with mass number $A = 154$, produced as described later in chapter 5. In this case, ^{154}Ho, ^{154}Er and ^{154}Dy are expected as contaminants with orders of magnitude higher yields from surface ionization than ^{154}Yb, the ion of interest. The mass separation power needed to separate ^{154}Yb from ^{154}Dy is $R \gtrsim 7000$, clearly exceeding the mass separation power of the ISAC high resolution separator of about 2000. Even higher separation powers are needed for the more exotic contaminants. For separation with the MR-TOF-MS, the ions performed 50 IT in the analyzer before being re-trapped. In about 30 min, a scan of the re-trapping time was done, covering all components of the isobaric beam. For each re-trapping time, full TOF mass spectra were obtained. The spectra were fitted using hyper-EMG shaped peaks [Purushothaman *et al.*, 2017] to obtain species abundance *vs* re-trapping time data, also for the overlapping ^{154}Eu^{+}, ^{154}Dy^{+} double peak. Spectra for some re-trapping times are shown in Fig. 4.7. These spectra demonstrate how different species can be selected by choosing the appropriate re-trapping time.

Abundance data and re-trapping model predictions are shown in Fig. 4.8. The unconstrained fit of the ^{133}Cs re-trapping window (Fig. 4.6) was used to predict the location and shape of the re-trapping windows for the different species. The agreement is very satisfying, showing that the re-trapping technique can be tuned reliably after short preparation in future. This confidence in setting the re-trapping time allows to study very rare cases, *e. g.*, ^{60}Ga, the isotope with the lowest yield measured at TITAN so far [Paul *et al.*, 2021]. In such cases the re-trapping window has to be set to a region of interest with only few detected events per hour, *i. e.*, it has to be set blindly in unknown territory.

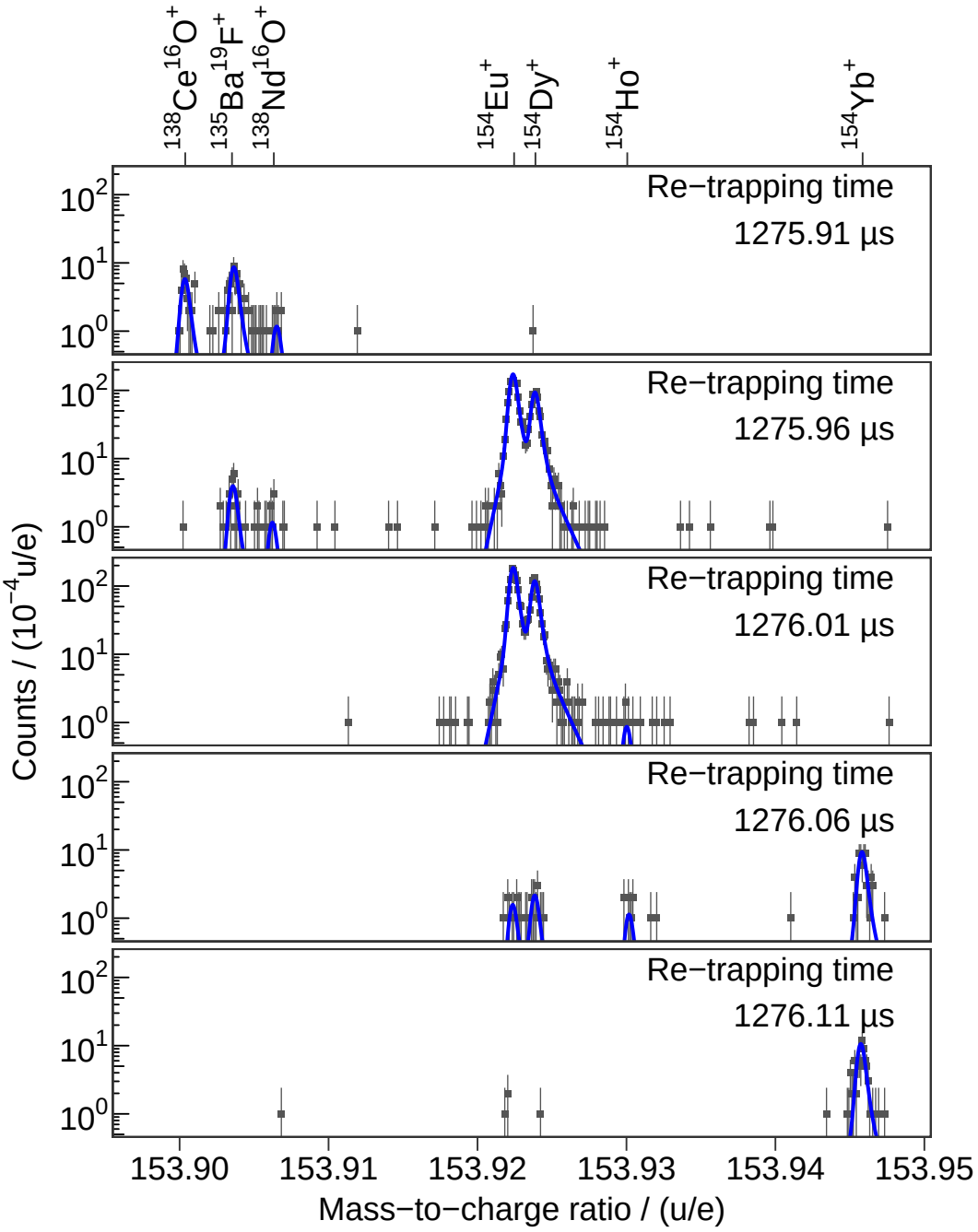

Figure 4.7: Mass spectra at $A = 154$ obtained for different re-trapping times. The re-trapping times increase from top to bottom, shifting the re-trapping window to heavier masses. For the mass measurement, the ions performed 328 IT in the analyzer, corresponding to a TOF of 8.05 ms. The mass resolving power in this measurement amounts to 240 000. Each spectrum was recorded in 40 s. Black curves represent fits to the data.

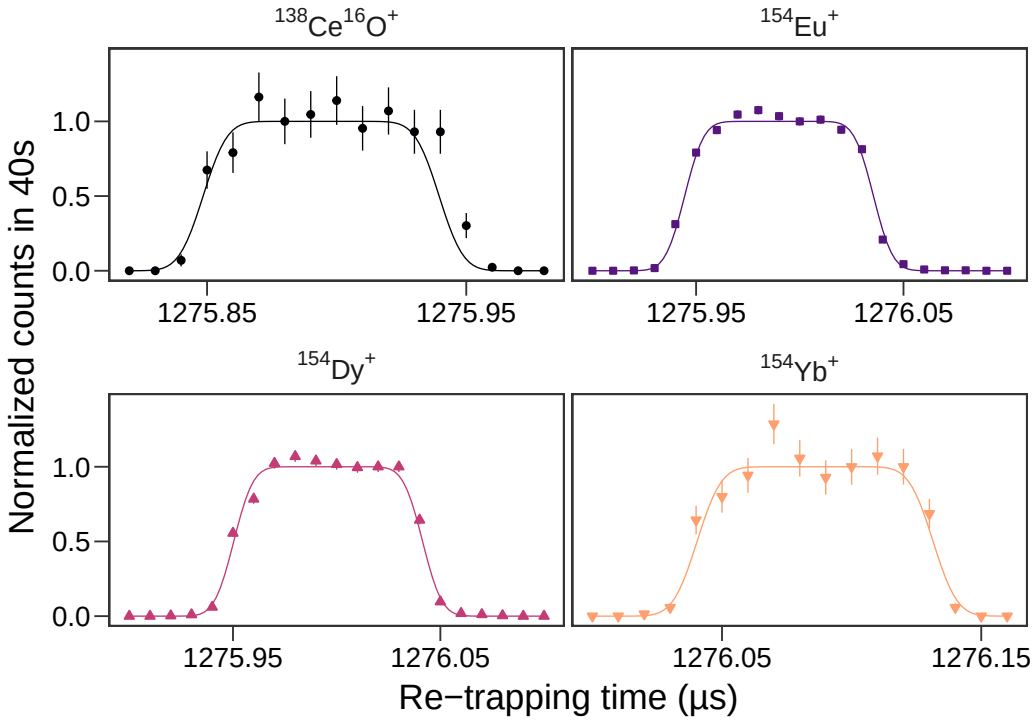

Figure 4.8: Normalized counts of several $A = 154$ TOF peaks *vs* re-trapping time. The smoothly plotted functions are model *predictions* of the re-trapping efficiency. They are obtained from offline calibrations, their positions are *not* fitted to the data shown.

As has been demonstrated, the re-trapping procedure is highly mass-selective. It provides a higher resolving power than conventional magnetic dipole separators. Shorter cycle time and higher ion capacity than with Penning traps can be reached. In contrast with other methods using MR-TOF-MS (selection of ions of interest using a fast-switching deflector, such as a Bradbury-Nielsen gate Plaß *et al.* [2008], a pulsed drift tube Wienholtz *et al.* [2017], or one of the reflectors Johnson *et al.* [2019]), it allows to use the same device to first act as an isobar separator and consecutively as mass spectrometer of the cleaned sample. This makes the complete system very compact and resources are used efficiently. The key here is that the phase space of the ion sample is "reset" after the separation, by buffer gas cooling. The relative re-trapping efficiency was described in a model and tested in offline measurements with an excellent agreement. The method has been developed for the MR-TOF-MS [Jesch *et al.*, 2015; Dickel *et al.*, 2019b] at TITAN but it can in principle be implemented in other MR-TOF-MS as well. By thus adding one or several stages of isobar separation, it can be used to turn MR-TOF-MS into tandem mass spectrometers (MS-MS) or sequential mass spectrometers (MS^n). It has already been applied in several measurements [Beck *et al.*, 2021; Izzo *et al.*, 2021; Mukul *et al.*, 2021; Paul *et al.*, 2021]. The impact on RIB measurements will be part of the following chapter.

Chapter 5

Nuclear Structure of very Neutron-Deficient Yb Isotopes near the N = 82 Shell Closure Revealed by Direct Mass Measurements

At TRIUMF, masses of very neutron-deficient isotopes of thulium ($Z = 69$) and ytterbium ($Z = 70$) were measured with high accuracy using TITANs MR-TOF-MS, which was built by the IONAS group in Gießen and introduced in the preceding chapters. The $N = 82$ neutron-shell closure up to the proton drip line and beyond and isomer excitation energy systematics in odd $N = 81$ nuclei are investigated. Furthermore, masses of the endpoints of two α-decay chains were measured. In one case it is the first direct mass measurements, reducing the uncertainties of all mass values in the connected chain. In the second case it is the first mass measurement at all, closing a missing link on the mass surface. Possible two-proton emitters with $Z > 72$ can now be identified by determining their mass through the connection to the measured nuclei via α-decay chains [Lykiardopoulou *et al.*, 2023]. An enlarged part of the nuclear chart is shown in Fig. 5.1 with highlighted key nuclei.

In this chapter, the ytterbium mass measurements and respective results are presented. Mass-selective re-trapping was necessary to perform these measurements and has been employed for the first time with exotic isotopes. Most results shown in this chapter have been already published in [Beck *et al.*, 2021].

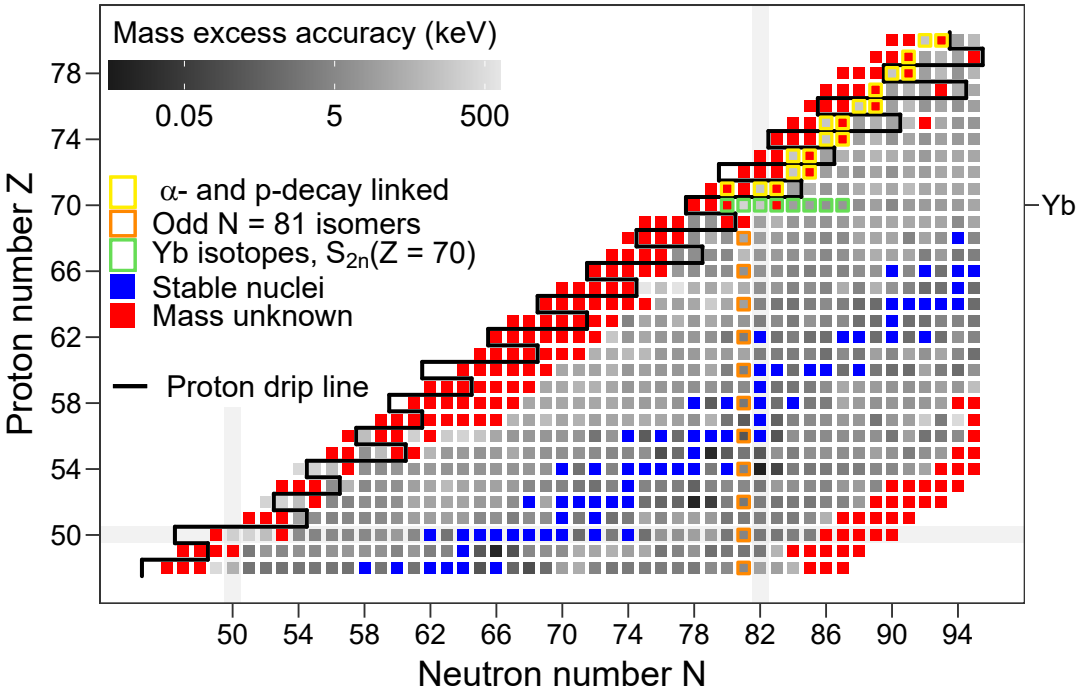

Figure 5.1: A part of the nuclear chart with the region of interest for the Yb mass measurements on the upper right. The nuclei are shaded according to the uncertainty of their mass excess value, nuclei with unknown mass are colored red, stable nuclei in blue. The data are from [Kondev *et al.*, 2021]. The $N = 50, 82$ and $Z = 50$ shell closures are indicated. Nuclei of interest are highlighted according to the chart legend. There are two pairs of α-decay chains, linked with known proton decays. In each pair one chain is anchored in an isotope of ytterbium, thus with the measurements in this work the mass values of the full chains are determined or their accuracy is increased. Additionally, $^{151,153,154}_{71}$Lu have proton decay channels into respective Yb isotopes with known decay energies. Their mass values can thus be deduced or their mass accuracies can be improved from the Yb mass measurements. The boundary between proton bound and unbound nuclei is drawn with the black line according to [Kondev *et al.*, 2021] for odd-Z nuclei and using predictions from [Neufcourt *et al.*, 2020] for even-Z nuclei.

5.1 Description of the Experiment

Neutron-deficient Yb isotopes were produced in spallation reactions at the ISAC facility (sec. 1.3.2). The 480 MeV proton beam from the TRIUMF cyclotron impinged onto a high-power tantalum target with 25 µA to 45 µA current. The TRIUMF resonant ionization laser ion source [Raeder *et al.*, 2014] was used to ionize the ytterbium atoms that effused out of the target. Ions were extracted and separated according to their mass-to-charge ratio at a mass separation power of 2000 using ISAC's high-resolution mass separator. The isobaric beam was transported to the TITAN MR-TOF-MS and mass measurements were performed (sec. 4.1). The ions performed one TFST and about 330 IT in the analyzer, corresponding to a total TOF of about 8 ms. The MRS was used during the first 35 IT to restrict the transmitted mass range to one atomic mass unit. A mass-resolving power of about 250 000 (FWHM) was achieved. For measurements, in which the isobaric contamination was too high to observe ytterbium ions without any further purification, the MR-TOF-MS was first used as an isobar separator employing the re-trapping technique. The cycle time of the measurement was 20 ms. If applicable, the first half of the cycle was used for re-trapping, otherwise the ions were stored for this additional time in the injection trap. The second half was used for the mass measurement. The mass measurements also served for identification of atomic and molecular ions [Reiter *et al.*, 2020], the beam consisted mostly of singly-charged Eu, Dy, Ho, Er, Tm, Yb, BaF and CeO ions. After the mass measurement of each ytterbium isotope, a spectrum without laser ionization was taken to verify the identification of the ytterbium ions by comparison of spectra with and without laser ionization. Sample spectra showing molecular and atomic species as well as the impact of the laser ion source are shown in Fig. 5.2. This demonstrates clearly that the identification is correct.

The first case where a measurement without re-trapping was impossible was ^{151}Yb. Due to the fast, non-scanning and sensitive measurement characteristics of MR-TOF-MS this is already three neutrons farther away from stability than one would expect achievable for TOF-ICR mass measurements in a Penning trap, compare *e. g.* [Leistenschneider *et al.*, 2018]. Figure 5.3 shows a comparison of mass spectra measured (a) without and (b,c) with mass-selective re-trapping. Without re-trapping, there is a considerable amount of background originating from high abundance isobaric contamination in the region where the thulium and ytterbium peaks are expected. ^{151}Eu was separated from ^{151}Yb using the edge of the re-trapping window. The edge was set approximately to ^{151}Ho, such that its count rate could be used to monitor drifts of the re-trapping window. The molecular isobaric contamination as well as ^{151}Eu and ^{151}Dy were strongly suppressed, while ^{151}Er, ^{151}Tm and ^{151}Yb were re-trapped for isobaric

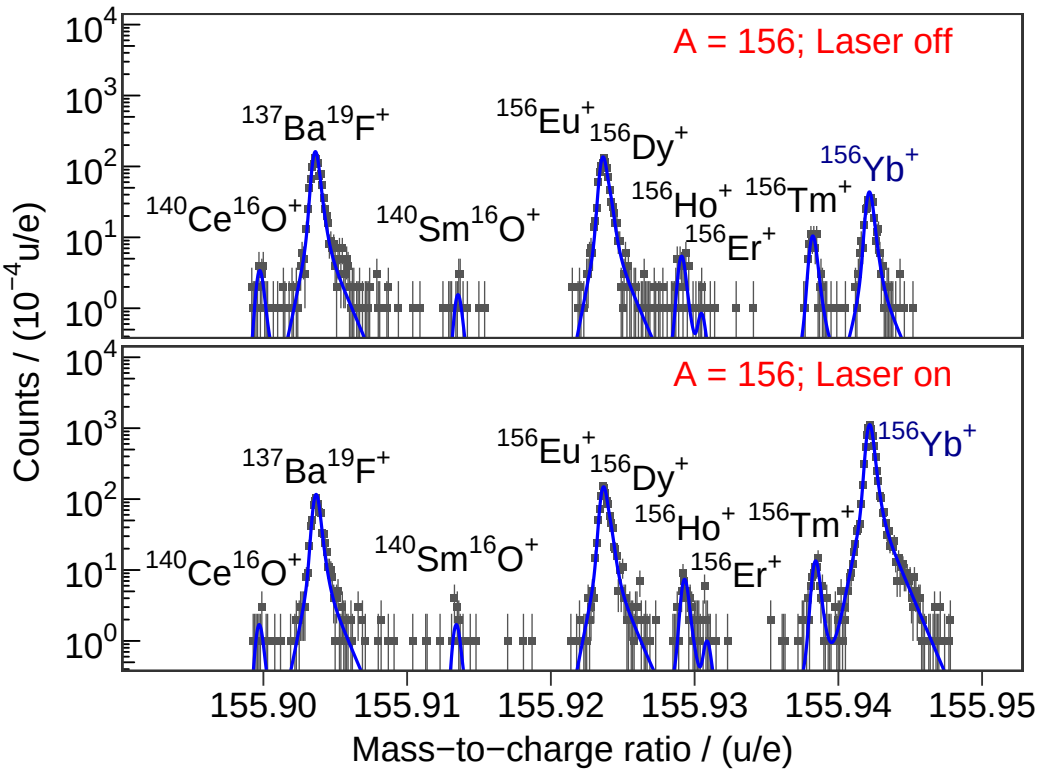

Figure 5.2: Measured mass spectra of molecular and atomic ions with mass number $A = 156$. The top and bottom spectra are without and with enhancing the Yb^+ yield with the laser ion source, respectively. The laser ion source enhanced the $^{156}Yb^+$ yield 25-fold. The ions performed 335 IT in the analyzer, corresponding to a TOF of 8 ms with a 20 ms measurement cycle. The mass resolving power in this measurement amounts to 260 000. The spectra were accumulated in about 15 min each. The blue curves represent fits to the data.

calibration and mass measurement. As the beam was dominated by largely abundant contaminants, re-trapping reduced the total rate on the MagneTOF detector significantly and the overall beam intensity entering the MR-TOF-MS could be increased by first reducing the attenuation in the ISAC beamline and then increasing the proton current on the target. This is making more efficient use of the available beam intensity and the allotted beam time. The reduction of the total number of ions that reach the detector by mass-selective re-trapping also minimizes the background resulting from persistent radioactivity implanted in the detector. Comparing the number of ^{151}Tm ions with the expected incoming ^{151}Eu ions, scaled using the ^{151}Er ions with re-trapping and increased proton current and without re-trapping (Fig. 5.3(a) and (c)), one arrives at an incoming dynamic range of five orders of magnitude. Measuring the masses of ^{151}Tm and ^{151}Yb would not have been possible without re-trapping, whereas with re-trapping the measurement is nearly background-free, as shown in Fig. 5.3. Similarly, the measurement of ^{150}Yb required re-trapping (Fig. 5.4). This measurement is four neutrons farther from stability than one would expect to be able to measure using TOF-ICR in a Penning trap and features the discovery of a new isotope [Thoennessen, 2023]. It is the first discovery of a new isotope with an MR-TOF-MS, and the first discovery of a new isotope at TRIUMF [Thoennessen, 2023], highlighting the increased reach towards more exotic nuclei achieved with re-trapping.

5.2 Data Analysis, Mass Values, Excitation Energies, Isomer-to-Ground-State Yield Ratios

For the analysis of the data, the procedure developed for the MR-TOF-MS at the FRS-IC [Ayet San Andrés *et al.*, 2019b, sec. 1.4.2] was used. The recorded time-of-flight data were converted to mass data in a time-resolved fashion, using an isobaric ion species present in the mass spectrum as calibrant. The obtained mass spectra were analyzed by fitting a Hyper-EMG function to the data, which takes into account the proper peak shape (resulting from the instrument response) including treatment of the tails caused by ion-optical aberrations [Purushothaman *et al.*, 2017]. A good description of the peak shape is needed for describing overlapping peaks (see *e. g.* Fig. 5.9 for a zoom into the ^{151}Yb ground and isomeric state double peak region of Fig. 5.3).

The actual fits to determine the peak positions of the calibrant and of the ytterbium isotopes were performed using a weighted maximum likelihood estimation (wMLE) to unbinned mass data using the software package R [R Core

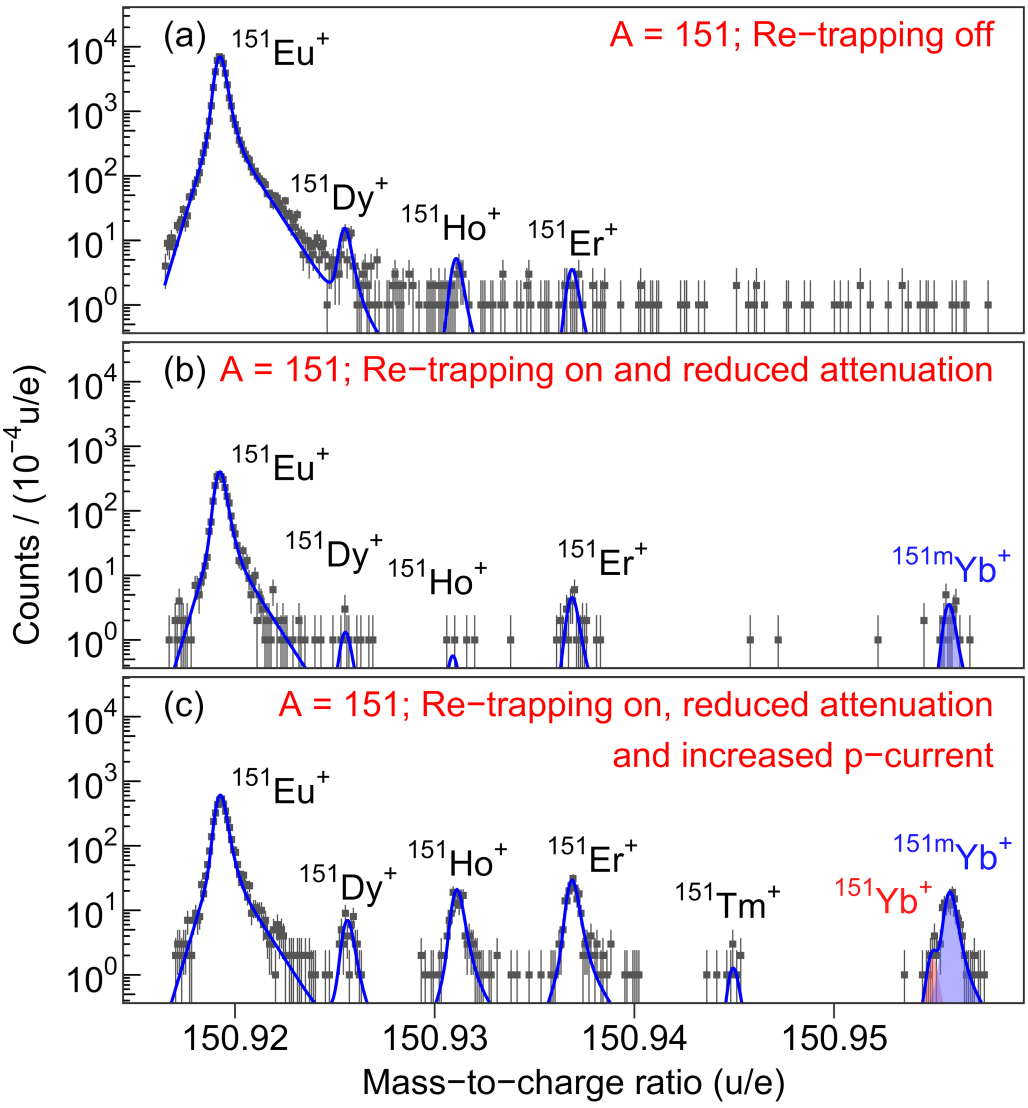

Figure 5.3: Measured mass spectra of ions with mass number $A = 151$ accumulated for equal times, (a) without re-trapping, (b) with re-trapping tuned for ^{151}Yb and reduced attenuation in the ISAC beam line, (c) as (b) but with increased proton-current on the target. The ions performed 335 IT in the analyzer, corresponding to a TOF of 8.14 ms with a 20 ms measurement cycle equally split for re-trapping and mass measurement. The mass resolving power in this measurement amounts to 270 000. The spectra were accumulated in 760 s each. The blue curves represent fits to the data.

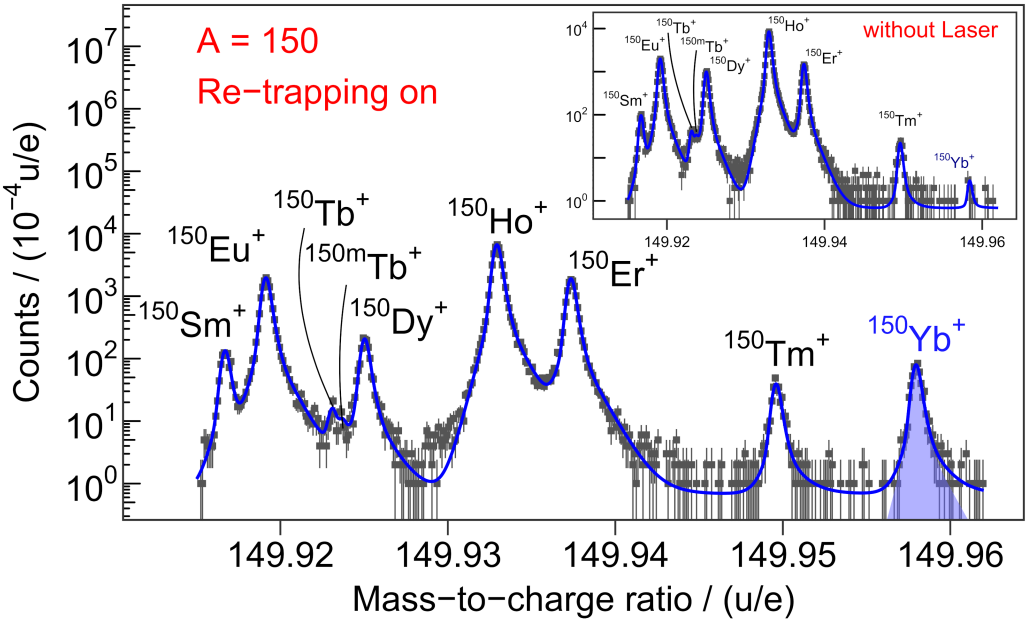

Figure 5.4: Measured mass spectrum of ions with mass number $A = 150$. This spectrum features the most exotic ytterbium isotope measured here; More than 500 events of ^{150}Yb (shaded area) were detected, the measurement required the re-trapping technique. ^{150}Yb was discovered newly in this work. The inset shows the spectrum acquired without Laser ionization for Yb, verifying the identification. With Laser ionization, there are more than twice as much Yb events compared to Tm, whereas without the Laser there is an order of magnitude less Yb than Tm. The mass of ^{150}Yb allows calculation of the mass of ^{151}Lu using the known proton separation energy. The ions performed 338 IT in the analyzer, corresponding to a TOF of 8.19 ms with a 20 ms measurement cycle equally split for re-trapping and mass measurement. The mass resolving power in this measurement amounts to 270 000. The blue curves represent fits to the data.

Team, 2021]. The isotopes of interest and their respective calibrants are listed in Table 5.1. The mass values of the calibrants were taken from the Atomic Mass Evaluation AME2020 [Wang *et al.*, 2021]. The uncertainties of the mass values were obtained by adding in quadrature the statistical uncertainties of the ion of interest and the calibrant, the uncertainties of the fitting of the ion of interest and the calibrant, the uncertainty of the literature mass of the calibrant, and the systematic uncertainty. The individual contributions are described in detail in [Ayet San Andrés *et al.*, 2019b]. Here the dominating contribution to the systematic uncertainty is shifts in the TOF due to voltage ringing caused by the switching of the reflector voltages for ejecting them from the analyzer to the detector [Will, 2017; Reiter *et al.*, 2018]. Its relative value amounts to 3×10^{-7}, which corresponds to $\approx 40\,\mathrm{keV}/c_0^2$ in the mass range under study. For excitation energies from double peak fits, uncertainty contributions due to the calibrant (statistical, fitting and literature mass uncertainty) were neglected, as in the case of $^{151}\mathrm{Yb}^{\mathrm{m}}$, where the calibrant for the mass spectrum, $^{151}\mathrm{Er}^{+}$, does not influence the uncertainty of the double-peak distance. Furthermore for excitation energies from double-peak fits, the systematic uncertainty due to switched reflector voltages was neglected, since these ions are not spatially separated enough at the times of the voltage switching. The systematic uncertainty dominates in all cases but in that of the ground state mass of ^{151}Yb. There, the overall uncertainty is dominated by the statistical uncertainty and the fit uncertainty due to the overlapping abundant peak of the isomeric state. The directly measured mass values and excitation energies are given in Tables 5.1 and 5.3. For the analysis of the $N = 82$ shell, binding energies of lutetium ($Z = 71$) isotopes were calculated using eq (1.15),

$$\mathrm{BE}(71, N) = \mathrm{BE}(70, N) - S_p(71, N)\,, \tag{5.1}$$

with the newly or more accurately measured ytterbium ($Z = 70$) binding energies and known lutetium proton decay energies [Wang *et al.*, 2021]. The uncertainty was obtained by adding the uncertainties of the new mass values and of the known proton decay energies in quadrature. In the case of the proton decay of ^{153}Lu into ^{152}Yb, both masses were already known with an uncertainty of 150 keV. The old mass value for ^{153}Lu and the one obtained from the new ^{152}Yb mass measurement were averaged with inverse variances $\sigma_{1,2}^{-2}$ as weights,

$$m = \left(m_1\sigma_1^{-2} + m_2\sigma_2^{-2}\right)/\sigma^{-2}\,,$$

with $\sigma_{1,2}$ denoting the uncertainties of the two input values and σ denoting the uncertainty of the weighted average. σ is calculated according to the method described in the statistics review of the particle data group [Workman *et al.*, 2022, chapter 40],

$$\sigma^{-2} = \sigma_1^{-2} + \sigma_2^{-2}\,.$$

Since here only the proton-decay link to ^{152}Yb is used, this method is equivalent to averaging the old and the new ^{152}Yb mass value with respective weights and then deriving the ^{153}Lu mass with the new proton decay. Full network calculations for nuclei with more than one link to known masses have been performed in [Lykiardopoulou *et al.*, 2023], which uses the masses measured in this work. The mass values derived here are given in Table 5.2, the results are in agreement with [Lykiardopoulou *et al.*, 2023].

Eight ytterbium ground state masses were determined. For the isotopes $^{154-157}$Yb, the ground state masses were already directly measured before, and the present results are in good agreement with the AME2020 [Wang *et al.*, 2021]; for three out of four cases there is agreement within the one-standard deviation uncertainty. For the ground state masses of ^{151}Yb and ^{152}Yb the uncertainties could be reduced, the masses of ^{150}Yb (Fig. 5.4) and ^{153}Yb were measured for the first time. Furthermore ^{150}Yb is the first discovery of a new isotope with an MR-TOF-MS. A $J^{\pi} = 11/2^{-}$ isomer has been observed in ^{151}Yb previously [Kleinheinz *et al.*, 1985; Toth *et al.*, 1986; Akovali *et al.*, 1990], but in this work its excitation energy was measured for the first time (Fig. 5.9). An isomer-to-ground state yield ratio of 11.1(3.1) with a total number of 460 events was determined in a double peak fit, corresponding to 38 and 422 events of the ground and isomeric states, respectively. The measured excitation energy is 679(105) keV. The mass of ^{153}Yb (Fig. 5.5) provides an anchor point for the α-decay chains from ^{173}Hg to ^{153}Yb and via known proton decays from ^{170}Au to ^{154}Lu and thus determines the absolute masses of 10 more nuclides and fixes the mass surface in this region of the chart of nuclides, as mentioned in a sub-chapter in the AME2017 [Wang *et al.*, 2017]. Similarly, the improved mass value of ^{152}Yb (Fig. 5.6) influences the region via two linked α-decay chains from ^{172}Hg to ^{152}Yb and via known proton decays from ^{161}Re to ^{153}Lu. The respective mass values and details of the influence on the mass surface in that region and related physics are discussed in [Lykiardopoulou *et al.*, 2023].

Nuclide	Calibrant	ME_{TITAN} (keV/c^2)	ME_{lit} (keV/c^2)	ΔME (keV/c^2)	
^{157}Yb	$^{157}Tm^+$	−53395(54)	−53420(11)	25(55)	
^{156}Yb	$^{156}Tm^+$	−53331(55)	−53266(9)	−65(56)	
^{155}Yb	$^{155}Eu^+$	−50514(45)	−50503(17)	−11(48)	
^{154}Yb	$^{138}Ce^{16}O^+$	−49934(45)	−49932(17)	−2(48)	
^{153}Yb	$^{153}Dy^+$	−47102(46)	—	—	
^{152}Yb	$^{136}Ce^{16}O^+$	−46061(46)	−46270(150)	209(157)	
^{151}Yb	$^{151}Er^+$	−41297(114)	−41540(300)	243(321)	
^{151}Yb^{m}	$^{151}Er^+$	−40617(49)	—	—	
^{150}Yb	$^{150}Dy^+$	−38635(44)	—	—	

Table 5.1: Summary of measured mass excess values of Yb isotopes, ME_{TITAN} and respective calibrants. Mass excess values from the AME2020 [Wang *et al.*, 2021], ME_{lit}, and the deviation $\Delta ME = ME_{TITAN} - ME_{lit}$, are given for comparison, where available. The visualization in that column shows how the measured values compare to the known ones. The $\pm 1\sigma$ intervals from this work are plotted as gray bars, the literature values, where available, and errors are plotted as black dot and line in the distance given by the mass excess deviation. The masses of the nuclides printed in bold were measured for the first time in this work.

Nuclide	Anchor	S_p (keV)	ME (keV/c^2)
^{151}Lu	^{150}Yb	1241.0(1.8)	−30105(45)
^{153}Lu	^{152}Yb	606(10)	−38185(45)
^{154}Lu	^{153}Yb	204(14)	−39609(48)

Table 5.2: Derived mass excess values of Lu isotopes, and respective anchors. Proton separation energies S_p from the AME2020 [Wang *et al.*, 2021] and directly measured masses from this work were used for the calculation. For the nuclides printed in bold, no experimental mass value could be determined prior to the mass measurements in this work.

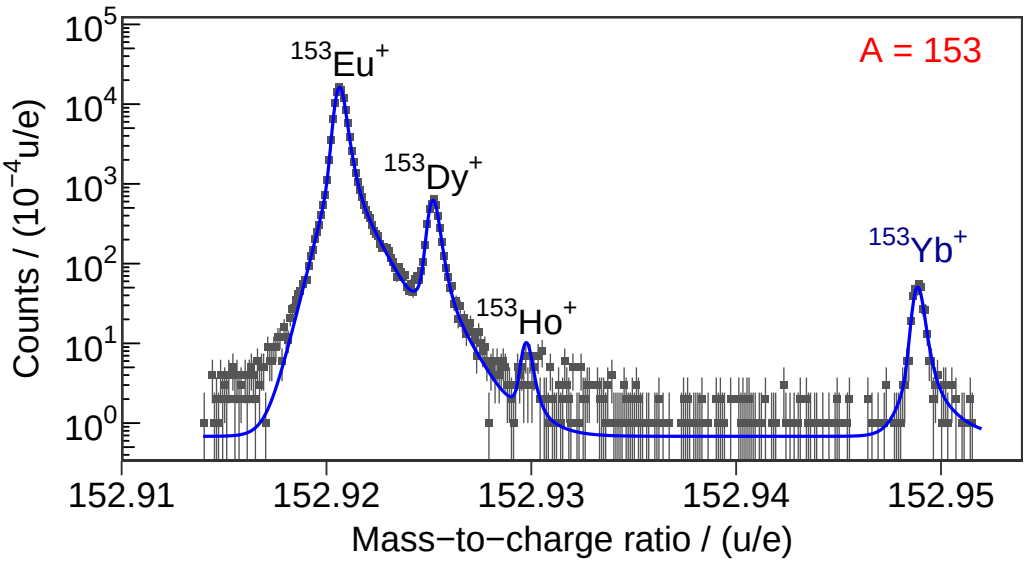

Figure 5.5: Measured mass spectrum of ions with mass number $A = 153$. ^{153}Yb provides an anchor for two α-decay chains, from ^{173}Hg to ^{153}Yb and from ^{170}Au to ^{154}Lu, linked with proton decays. The nuclide ^{154}Lu is also directly connected to ^{153}Yb via a known proton decay. Its mass was here measured for the first time and thus determines the masses of 10 more nuclides and fixes the mass surface in this region of the chart of nuclides. The ions performed 330 IT in the analyzer, corresponding to a TOF of 8.07 ms with a 20 ms measurement cycle. The mass resolving power in this measurement amounts to 220 000. The blue curves represent fits to the data.

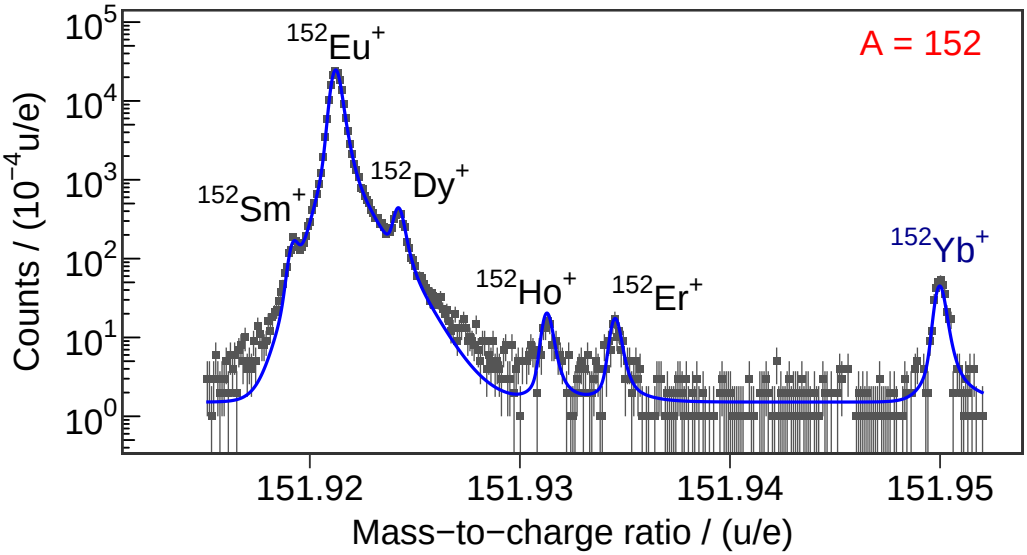

Figure 5.6: Measured mass spectrum of ions with mass number $A = 152$. ^{152}Yb provides an anchor for two α-decay chains, from ^{172}Hg to ^{152}Yb and from ^{161}Re to ^{153}Lu, linked with proton decays. Its mass was here measured for the first time directly, shifting the mass value and reducing its uncertainty. This influences the masses of seven more nuclides and accordingly the mass surface in this region of the chart of nuclides. The ions performed 332 IT in the analyzer, corresponding to a TOF of 8.09 ms with a 20 ms measurement cycle. The mass resolving power in this measurement amounts to 250 000. Blue curves represent fits to the data.

5.3 The N = 82 Shell Closure

With the newly measured and derived masses, the $N = 82$ shell closure can be examined in the extreme proton-rich region, using two-neutron separation energies S_{2n} (sec. 1.1.2). The two-neutron separation energies S_{2n} for Yb were previously known only down to $N = 84$. The new results are shown in Fig. 5.7. Using the evaluated literature data [Wang *et al.*, 2021] for the masses resulted in irregular behavior of the two-neutron separation energies S_{2n} for ^{145,147}Tb, which are both influenced by ^{145}Tb. Since the value in the evaluated data differed by $\approx 500\,\mathrm{keV}$ from the original publication, the original measurement data was used for ^{145}Tb [Litvinov *et al.*, 2005], which removed the inconsistency. The characteristic steep decrease at $N = 82$ can be seen with the newly measured masses for ytterbium and lutetium, that means the direct mass measurements and the derived mass values clearly establish the persistence of the shell at the hitherto farthest measured point from the line of β–stability on the chart of the nuclides. The experimental $N = 82$ data are compared with different theoretical models, the macroscopic-microscopic finite-range droplet model FRDM(2012) [Möller *et al.*, 2016], and two microscopic models, the Hartree-Fock-Bogoliubov model with BSk21 Skyrme interaction (HFB-21) [Goriely *et al.*, 2010], and the energy density functional UNEDF0 [Kortelainen *et al.*, 2010]. These models predict the two-neutron separation energies with a similar trend as observed, but they scatter on the order of 1 MeV.

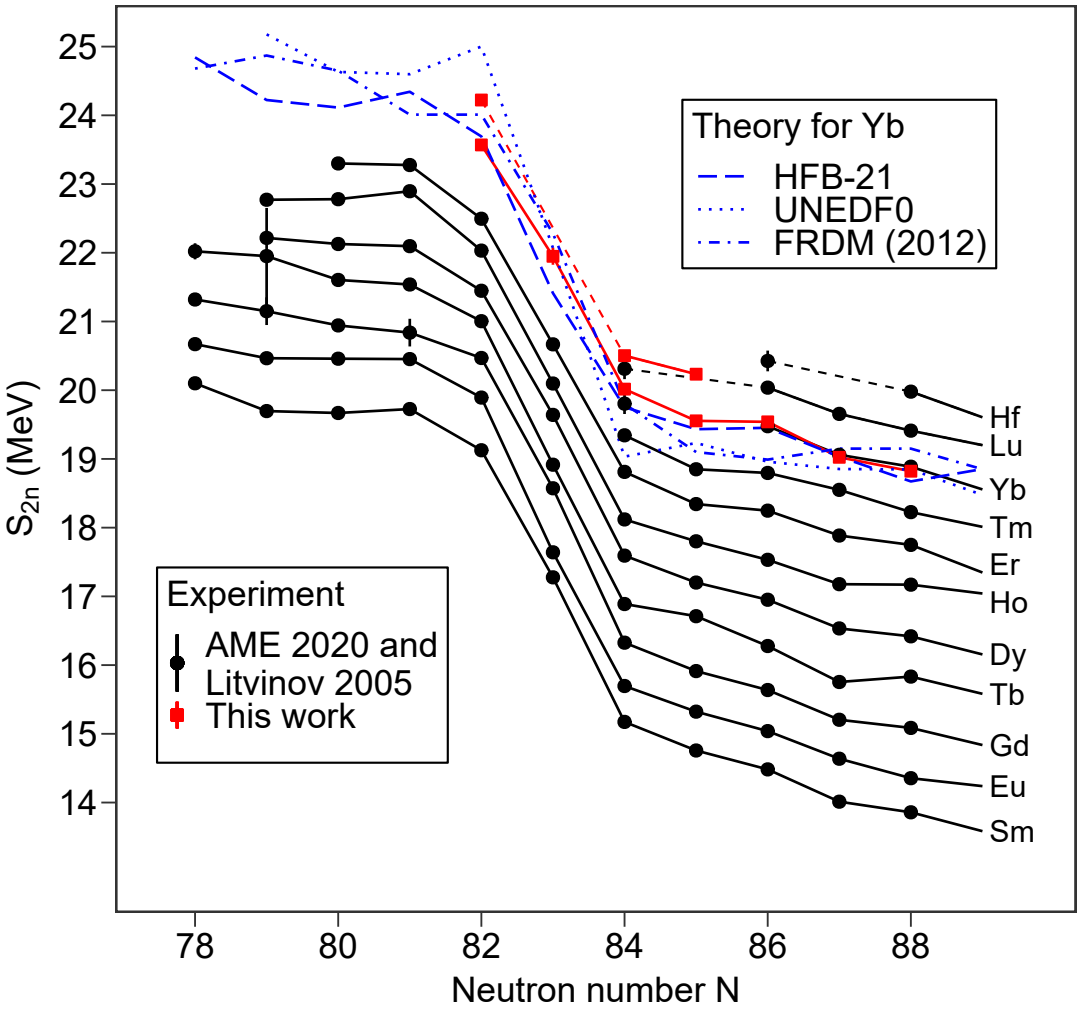

Figure 5.7: Experimental two-neutron separation energies around $N = 82$ for neutron-deficient isotopes and model predictions for Yb from HFB21 [Goriely *et al.*, 2010], UNEDF0 [Kortelainen *et al.*, 2010], and FRDM2012 [Möller *et al.*, 2016]. Literature data from the AME2020 [Wang *et al.*, 2021] and from the original source [Litvinov *et al.*, 2005] for the mass of ^{145}Tb. The data for Lu in this work was calculated from new or more accurate Yb data from this work and literature proton separation energies [Wang *et al.*, 2021]. Most error bars are hidden in the symbols, lines are drawn to guide the eye.

The strength of the shell closure can be analyzed further with the empirical two-neutron-shell gap energy Δ_{2n}, shown in Fig. 5.8 for $N = 80, \ldots, 84$ isotones against the number of protons, for $N = 82$ in comparison with the theoretical models. For $N = 82$, the two-neutron-shell gap energies Δ_{2n} are larger than for the adjacent and next isotones due to the closed neutron shell. Using the evaluated literature data [Wang *et al.*, 2021] for the masses resulted in irregular behavior of the two-neutron-shell gap energy Δ_{2n} most prominently seen for ^{145}Tb as the signature of a weak shell closure for $N = 80, Z = 65$, which has no physical explanation. Since the mass value in the evaluated data differed by $\approx$ 500 keV from the original publication, the original measurement data was used for ^{145}Tb [Litvinov *et al.*, 2005], which removed the inconsistency. The two-neutron-shell gap energy $\Delta_{2n}(N = 82)$ has a maximum at the $Z = 50$ proton shell closure, a phenomenon known as mutually enhanced magicity [Zeldes *et al.*, 1983; Lunney *et al.*, 2003]. From $Z = 50$ with increasing proton number, the two-neutron-shell gap $\Delta_{2n}(N = 82)$ decreases, from $Z = 58$ onward the reduction is only weak. This is also seen for $\Delta_{2n}(N = 83)$. So far, the most proton-rich nuclide, for which $\Delta_{2n}(N = 82)$ was known, was $^{150}_{68}$Er. The newly determined value for $^{152}_{70}$Yb, despite being the lowest value found so far, establishes that the shell persists with almost unmodified shell gap energy up to the proton drip line. The value determined for $^{153}_{71}$Lu establishes the persistence of the shell even beyond the proton drip line. The drip line is expected to lie between $^{152}_{70}$Yb and $^{153}_{71}$Lu for $N = 82$ [Wang *et al.*, 2021; Neufcourt *et al.*, 2020]. The comparison with established models shows that mass measurements of exotic nuclei are key for a better understanding of the nucleus. Although HFB-21 comes closest to the measured and derived two-neutron-shell gap energy values $\Delta_{2n}(N = 82)$ both around $Z = 50$ and for the most proton-rich isotones, none of the models fully reproduces the experimental trend. Clearly models can not cover all details of the real physical system, however the demonstrated deviations highlight the importance of measurements for model improvements —like implementing more details— and model error estimates.

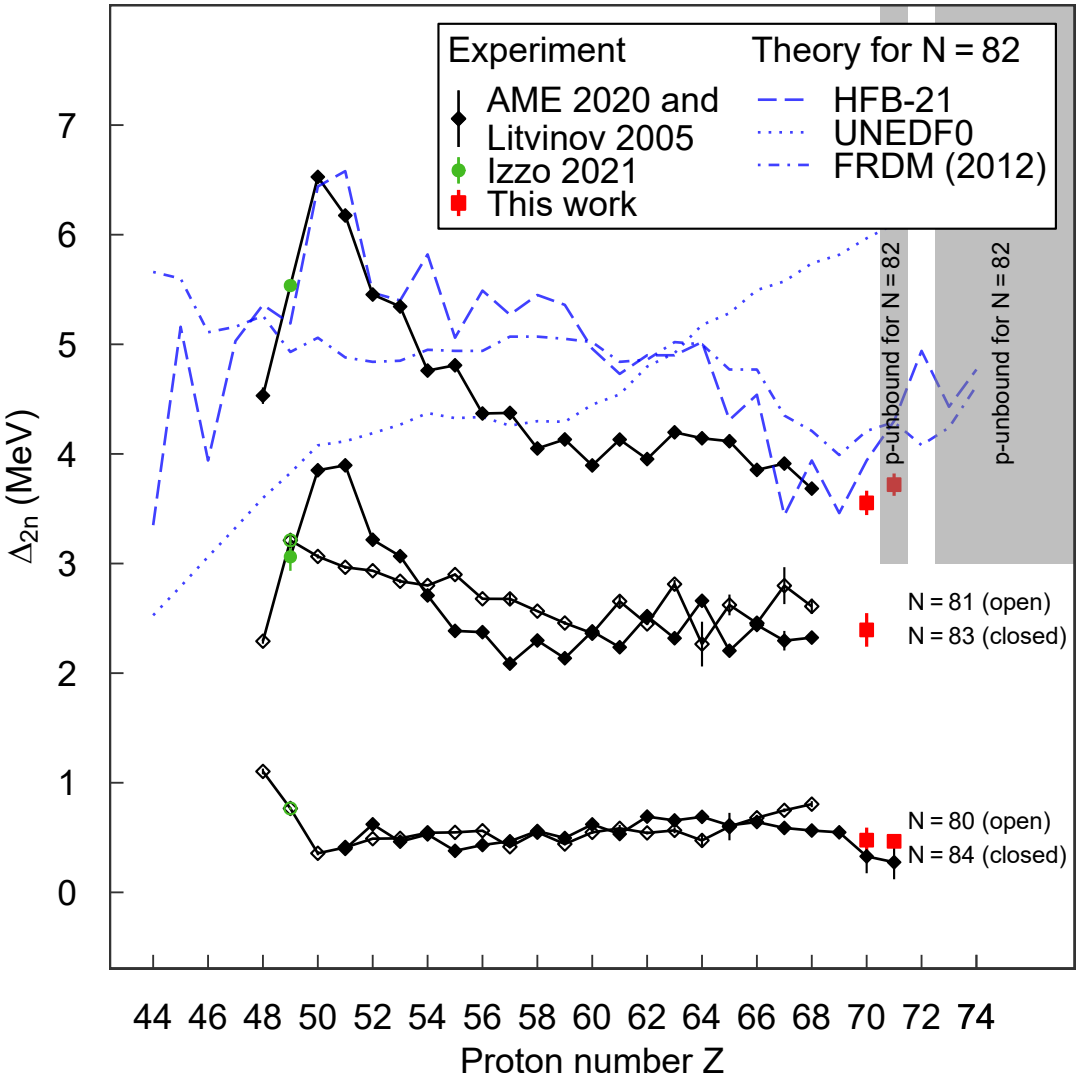

Figure 5.8: Experimental two-neutron-shell gap Δ_{2n} at $N = 80, \ldots, 84$ *vs* proton number Z and $N = 82$ model predictions from HFB21 [Goriely *et al.*, 2010], UNEDF0 [Kortelainen *et al.*, 2010], and FRDM2012 [Möller *et al.*, 2016]. The data with the largest Δ_{2n} values is from the $N = 82$ isotones, experimental data for the surrounding isotones is drawn for comparison. Literature data are from the AME2020 [Wang *et al.*, 2021] and from the original source [Litvinov *et al.*, 2005] for the mass of ^{145}Tb. The value for indium ($Z = 49$) required the masses of ^{133,134}In from [Izzo *et al.*, 2021] which have also been measured using the TITAN MR-TOF-MS and required mass-selective re-trapping. The Δ_{2n} values for ^{153,155}Lu required the masses of ^{151,153}Lu, which were determined using the ^{150,152}Yb masses and literature proton separation energies [Wang *et al.*, 2021]. Regions of proton-unbound nuclides for $N = 82$ are indicated [Wang *et al.*, 2021; Neufcourt *et al.*, 2020]. Most error bars are hidden in the symbols, lines are drawn to guide the eye.

5.4 The odd-A N = 81 Isomer Chain

The sequence of $J^\pi = 11/2^-$ isomers in the odd-A $N = 81$ isotones is remarkable, because the excitation energies of these $J^\pi = 11/2^-$ isomers stay approximately constant at 750 keV between ^{139}Ce and ^{149}Er, over a range of eleven isotones. Such an effect is unique throughout the chart of the nuclides. Its origin has been considered enigmatic since its discovery more than 60 years ago [Kotajima and Morinaga, 1960; Heyde and Brussaard, 1973; Toth *et al.*, 1985]. The next isomer in this series was deduced from β-delayed proton decay data, but not directly observed via γ-spectroscopy [Toth *et al.*, 1986]. The IT branching ratio of the ^{151}Yb isomer is estimated to be about one order of magnitude lower than that of ^{149}Er [Toth *et al.*, 1986] and due to its exoticity the expected yield is about two orders of magnitude lower. In consequence the $J^\pi = 11/2^-$ excitation energy in ^{151}Yb is not accessible via γ-spectroscopy. Mass spectrometry does not need the excited state to decay and thus has an intrinsic advantage when determining the excitation energy of longer-lived isomeric states, making it the method of choice here. The newly measured excitation energy of 679(105) keV for the isomer in ^{151}Yb falls in line with the excitation energy of about 750 keV of this sequence. In addition, ^{149}Er ground and isomeric state were measured and the respective excitation energy could be determined as 807(132) keV which is in agreement with the literature within the error. For ^{149}Er, the error is dominated by the low statistics, as the erbium yield was not enhanced by laser ionization. While the error is larger than for the literature data, an isomer-to-ground-state yield ratio could be extracted to provide a reference for what to expect for ^{151}Yb. Thus the data demonstrates the feasibility of the analysis method and strengthens the identification of the isomer in ^{151}Yb. Table 5.3 summarizes the excitation energy measurements presented here.

Nuclide	E^*_{TITAN} (keV/c^2)	E^*_{lit} (keV/c^2)	ΔE^* (keV/c^2)	Events in g.s. and i.s.	i.s. to g.s. yield ratio
^{149}Er$^{\mathrm{m}}$	814(139)	741.8(0.2)	72(139)	44	3.4(1.0)
^{151}Yb$^{\mathrm{m}}$	679(105)	—	—	422	11.1(3.1)

Table 5.3: Measured even-Z $N = 81$ $J^\pi = 11/2^-$ isomer excitation energies E^*_{TITAN}. Excitation energies from the NUBASE2020, E^*_{lit}, and the deviation $\Delta E^* = E^*_{\mathrm{TITAN}} - E^*_{\mathrm{lit}}$ [Kondev *et al.*, 2021], are given for comparison, where available.

The fits to the data are shown in Fig. 5.9. In both cases the isomeric state with the higher spin is populated dominantly, this is more pronounced in the case of Yb. For the double-peak fit of the ^{151}Yb ground and isomeric state, a good description of the peak shape over two orders of magnitude is needed due to their close distance.

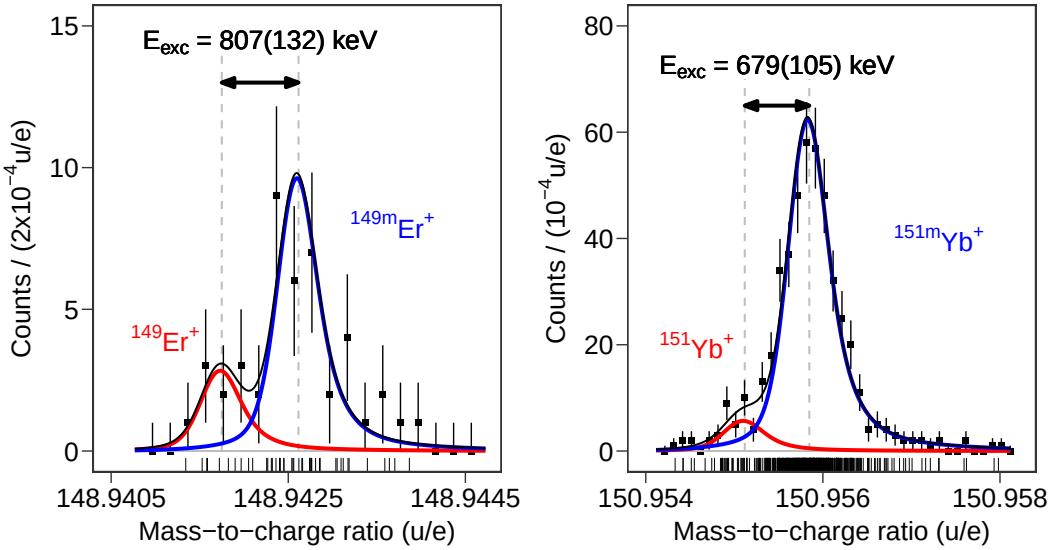

Figure 5.9: Mass spectra of the singly charged ^{149}Er and ^{151}Yb nuclear ground and $J^\pi = 11/2^-$ isomeric states with measured excitation energies of 807(132) keV and 679(105) keV, respectively. The ions performed 324 and 335 IT in the analyzer, corresponding to a TOF of 7.82 ms and 8.14 ms, respectively. The mass resolving power in these measurements amounts to 270 000. The red and blue curves depict the two components of the hyper-EMG double peak fits.

Figure 5.10 exemplary shows detailed partial level schemes of the two measured nuclei. For ^{149}Er and ^{151}Yb, the low energy levels have the same order with a $s_{1/2}$ ground and $h_{11/2}$ isomeric state and an intermediate $d_{3/2}$ level. The energy of this level is known for ^{149}Er, but not for ^{151}Yb, it is in the latter case thus placed at an arbitrary energy. For ^{149}Er, also the isomeric state's excitation energy was measured before and is indicated by a black line, the here measured value and error is indicated by the gray area spanning (807 ± 132) keV in height. As mentioned, the isomeric state's excitation energy in ^{151}Yb is not measurable with γ-spectroscopy due to the lower branching ratio of the internal transition and the lower yield at RIB facilities and as argued above, this makes mass-spectrometry the tool of choice to access the isomeric state in ^{151}Yb. For ^{151}Yb, the gray area similarly spans (679 ± 105) keV in height, here the black line indicates the newly measured excitation energy.

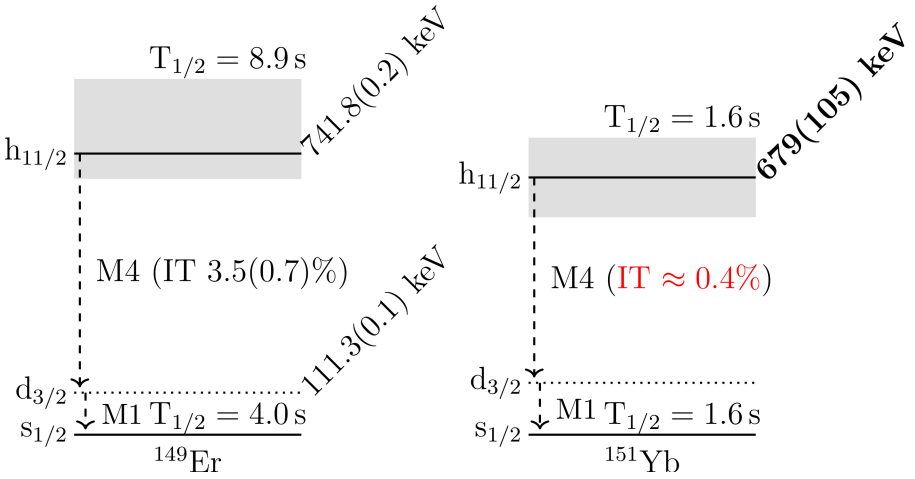

Figure 5.10: Low energy level schemes of ^{149}Er and ^{151}Yb. γ transitions are indicated including the known multipolarity and branching ratios for the known or estimated internal transition (IT). The intermediate $d_{3/2}$ level is indicated by a dotted line. The uncertainty of the isomeric state excitation energy from this work is visualized by the light gray area. For ^{149}Er, the levels are well known from γ-spectroscopy. The M4 transition in ^{151}Yb has a very low estimated branching ratio [Toth *et al.*, 1985], the main decay channel is β^+-decay into the daughter nucleus ^{151}Tm.

The excitation energies of these $J^\pi = 11/2^-$, odd-A $N = 81$ isomers is constant over about half of the $N = 82$ shell, the experimental data are shown in Fig. 5.11a. This behavior is highly surprising. According to nuclear mean-field theory, the dependence of energy *vs* total angular momentum is usually strongly irregular for neutron-hole states [de Voigt *et al.*, 1983]. Still, after the extension of the experimental data of the series, state-of-the-art mean-field calculation were performed by I. Dedes, J. Dudek and co-workers [Dedes (Private communication)]. These succeeded in finally explaining the origin of the constant excitation energies, summarized in Fig. 5.11b. Key to the explanation are nuclear deformations.

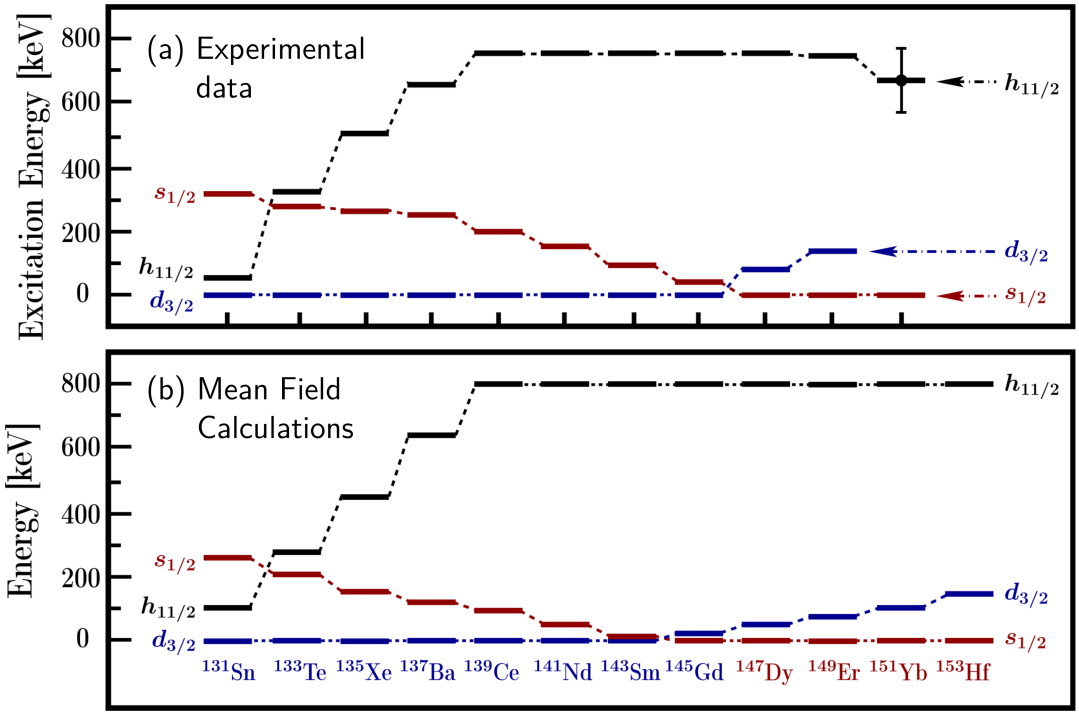

Figure 5.11: (a) Measured excitation energies of isomers in the odd $N = 81$ isotones from Sn to Yb [Toth *et al.*, 1985; Kondev *et al.*, 2021]. The value for ^{151}Yb results from the present work. Most error bars are invisible within the scale of the figure. They have been obtained with γ-spectroscopy, as the life-times are sufficiently short. Note the constancy of the $h_{11/2}$ excitation energy from Ce to Yb. (b) Corresponding results obtained using mean-field calculations with universal parametrization of the Woods-Saxon Hamiltonian. From ^{141}Nd to ^{153}Hf, the filled proton levels are near-degenerate, *c. f.* Fig. 5.12.

The phenomenological, deformed Woods-Saxon (WS) Hamiltonian in its so-called universal parametrization was employed [Dudek and Werner, 1978b; Dudek *et al.*, 1979b, 1980b, 1981; Cwiok *et al.*, 1987]. The parameters are fixed throughout the chart of nuclides and not fitted to the specific region. This WS Hamiltonian has been successfully applied in numerous nuclear structure calculations. Microscopic-macroscopic potential-energy calculations were performed for all even-Z isotones from Sn to Hf, the Strutinsky method [Strutinsky, 1967] was applied using single-particle energies obtained from the WS Hamiltonian to account for the microscopic effects. Nuclear deformations of the ground and isomeric states were obtained by calculating the total nuclear energy of these states for different quadrupole deformations, by varying the deformation parameter α_{20}. The impact of the shell closures at $Z = 50$ and $N = 82$ is seen in that the ground-state equilibrium shapes remain spherical for the lighter isotones from Sn to Ba. Local minima in the energy in dependence of α_{20} could be associated with the ground and isomeric states at different deformations for the heavier isotones. More precisely, for ^{139}Ce and heavier isotones, oblate ($\alpha_{20} < 0$) equilibrium shapes are predicted for the ground state. Below spherical closed neutron shells (here $N = 82$), K-isomers usually correspond to nucleonic configurations with maximum alignment of the angular-momentum j, *i. e.* with projection $m_j = j$, at slightly prolate quadrupole shapes [de Voigt *et al.*, 1983]. For the $J^\pi = 11/2^-$ isomers, small but increasingly prolate shapes with $\alpha_{20} \approx 0.1$ are predicted. The underlying stabilizing structural element is the very high proton-state density at $\alpha_{20} \approx 0.12$ (Fig. 5.12), where six levels are almost degenerate.

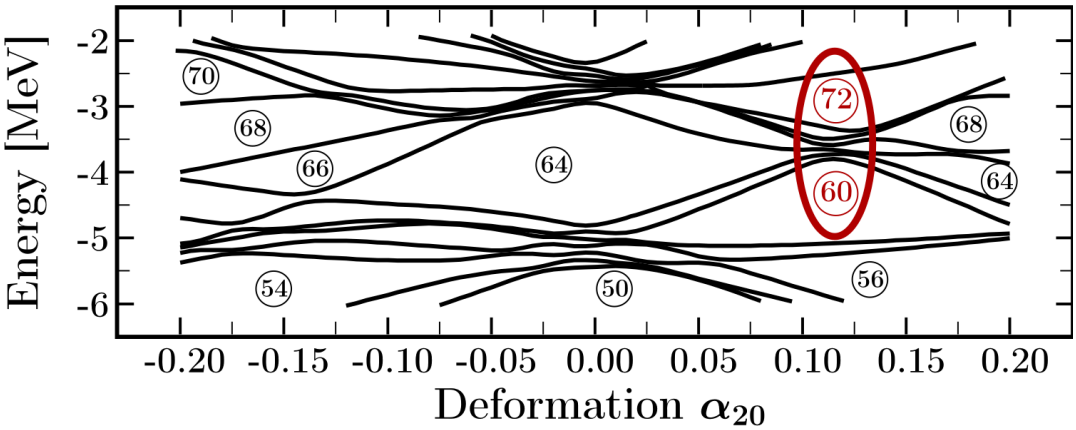

Figure 5.12: Single proton energies as functions of the quadrupole deformation α_{20}, calculated using the Woods-Saxon Hamiltonian. The numbers in the circles are the numbers of protons that can fill the levels below the circles. 6 levels are near-degenerate at small prolate deformations, indicated with oval curve.

The shell-correction is sensitive to the density of single particle levels near the Fermi energy [Strutinsky, 1967; Brack *et al.*, 1972], which is constant for degenerate levels. For the degenerate levels being filled with two protons each for $i \geq i_0$ up to $i_{\max}$, the shell-correction (1.4) becomes

$$\Delta E_{\text{shell}} = \Delta E_{\text{shell},i<i_0} + 2(i_{\max} - i_0 + 1)\underbrace{\left(\varepsilon_{i_0}^{\text{s. p.}} - \int_{-\infty}^{\tilde{\lambda}} Ef\left(\tfrac{E-\varepsilon_{i_0+1}^{\text{s. p.}}}{\gamma}\right)\mathrm{d}E\right)}_{\text{contribution close to Fermi energy}}. \quad (5.2)$$

It is nearly constant and strongly negative, leading to the mentioned minima in the nuclear binding energy at $\alpha_{20} \approx 0.12$ for these nuclei. The new calculations show that the isomer energies are also stabilized at about 800 keV. This evolution coincides with the evolution of the measured energies of the isomers, which increase from about 40 keV in ^{131}Sn to about 750 keV in ^{139}Ce, i.e., within the zone of spherical ground-states. The stabilization at about 750 keV, starting with ^{139}Ce ($Z = 58$), coincides with the mean-field predictions of the slightly prolate quadrupole shapes with quadrupole deformations of $\alpha_{20} \approx 0.10$ at the $J^\pi = 11/2^-$ isomeric energy minima. The calculations also show that the trend of constant $J^\pi = 11/2^-$ isomer excitation energies continues for ^{153}Hf ($Z = 72$).

The calculations were done at the $N = 80$ isotones and WS single particle energies ε^{WS} for the neutron $s_{1/2}$, $d_{3/2}$, $h_{11/2}$ orbitals were added to investigate the $N = 81$ isotones. These come from more general calculations, where the WS Hamiltonian was diagonalized for different deformations and the change of its energy levels was investigated by the theory collaborators. As the levels change with deformation, when the nuclei become prolate, the highest level becomes dominantly an $h_{11/2}$ state with spin projection $m_j = 11/2$. This is consistent with the experimentally observed level crossing. Its energy then stays constant in the series under study since the deformation is constant. Relative WS single particle energies of these orbitals, $\varepsilon^{\text{WS}}(s_{1/2})$, $\varepsilon^{\text{WS}}(d_{3/2})$ and $\varepsilon^{\text{WS}}(h_{11/2})$, are shown in Fig. 5.11 in comparison with the experimental data. In this series, the J^π=$1/2^+$, $3/2^+$, and $11/2^-$ states are neutron-hole states below the closed shell and can be associated with these $s_{1/2}$, $d_{3/2}$, $h_{11/2}$ orbitals, respectively. The J^π=$3/2^+$ ground-states with even-Z from Sn to Gd can be associated with $d_{3/2}$, and J^π=$1/2^+$ with $s_{1/2}$ orbitals from Dy to Hf. The latter orbital does not couple with the spin-orbit field at all, whereas the former does so only very weakly, so that their crossing at Gd and Dy reflects mainly the evolution of the central potential with Z.

Conclusion and Outlook

Novel MR-TOF-MS techniques have been applied to advance the frontier in mass measurements of exotic nuclei and the understanding of nuclear structure at the extremes. At the FRS-IC, several hardware and software elements have been upgraded. The new slow control system at the FRS-IC is running stable and ready to control, monitor and log existing and also various planned extensions of the detector setup. A procedure for systematically tuning the ion optics to unprecedented mass resolving powers $R = m/\Delta m = 1\,000\,000$ and beyond has been established. This enabled the measurement of ${}^{71}_{35}\mathrm{Br}$, ${}^{70,71}_{34}\mathrm{Se}$ and ${}^{69}_{33}\mathrm{As}$, all close to the $N = Z$ line and the latter for the first time directly, with only 10 events and with reduced uncertainty compared to the average of the previous indirect measurements. For the molecule ${}^{14}\mathrm{N}{}^{15}\mathrm{N}{}^{40}\mathrm{Ar}$ an accuracy of $\delta m/m = 1.7 \times 10^{-8}$ was reached, which is the highest accuracy for MR-TOF-MS world-wide. The techniques applied at the FRS-IC have since been used at the TITAN MR-TOF-MS as well, also there leading to improved mass resolving powers.

The high mass resolving power enables mass measurements with fewer ions with high mass accuracy. This allows to study nuclei with very low production yields, and also opens up the possibility to investigate physics previously not addressable with MR-TOF-MS, like testing the unitarity of the CKM matrix via mass measurements.

For TITAN, mass-selective re-trapping was characterized and for the first time used with exotic nuclei, enabling the direct measurement of 2 new and 2 improved ground state masses for neutron deficient ${}_{70}\mathrm{Yb}$ isotopes, the first measurement of the excitation energy of the $J^\pi = 11/2^-$ isomeric state in ${}^{151}_{70}\mathrm{Yb}$ and the indirect determination of 11 more ground state masses connected via α- and p-decays to two of the newly measured masses. The measurement of the mass of ${}^{150}\mathrm{Yb}$ is at the same time the first discovery of a new isotope with an MR-TOF-MS. The direct ground state mass measurements of the ${}_{70}\mathrm{Yb}$ isotopes and the subsequent determination of masses of ${}_{71}\mathrm{Lu}$ isotopes have established the $N = 82$ neutron shell closure farthest from the valley of β-stability with unmodified shell gap; the shell structure far from the valley of stability is a key question of modern nuclear physics.The measurement of the $J^\pi = 11/2^-$ isomeric state excitation energy extends a series of constant excitation energies in these odd $N = 81$ states, which could now be explained by deformation of the ground and isomeric states in collaboration with theorists employing state-of-the-art nuclear mean field [Beck *et al.*, 2021].

Mass-selective re-trapping has meanwhile become a standard technique at

TITAN [*e. g.* Izzo *et al.*, 2021; Mukul *et al.*, 2021; Paul *et al.*, 2021]. It is providing separation and mass measurement in a single device. This allows to measure masses of nuclei which are two neutrons farther from stability compared to conventional MR-TOF-MS measurements, which already reach out two neutrons farther from stability compared to TOF-ICR. Using the MR-TOF-MS as mass separator and subsequently delivering the mass-separated beam towards the other parts of the TITAN setup, re-trapping also facilitates measuring masses of more exotic nuclei with TOF-ICR using highly charged ions. Furthermore, it can be employed to deliver an isobarically cleaned beam to laser spectroscopy and other measurements.

Both improvements, separating exotic ions from isobaric contaminants by mass-selective re-trapping and high accuracy measurements with low statistics due to superior mass resolving power, extend the reach of current and future rare ion beam facilities.

Zusammenfassung

Das Studium exotischer Kerne, das heißt sehr kurzlebiger Kerne weitab vom Stabilitätstal in der Nuklidkarte, ist wesentlich für das Verständnis der Struktur des Atomkernes und der zugrundeliegenden Wechselwirkungen. Starke, schwache und elektromagnetische Wechselwirkung zwischen den Kernbausteinen tragen in einem komplexen Zusammenspiel zur Bindungsenergie und damit zur Masse des Kerns bei. Daher ist die Masse eines Atomkerns eine seiner wichtigsten grundlegenden Eigenschaften und Präzisions-Massenmessungen sind essenziell zur Untersuchung von Kernstruktur und elementaren Wechselwirkungen. Messungen an exotischen Kernen stellen eine besondere Herausforderung dar, da die Kerne kurzlebig sind und zunächst erzeugt werden müssen. Das ist üblicherweise nur in kleinen Raten möglich, insbesondere für exotischere Kerne, die weiter vom Stabilitätstal entfernt sind. Bei den Kernreaktionen zur Erzeugung eines Zielkerns werden typischerweise sehr viele weitere, weniger exotische Kerne in höherer Rate erzeugt. Zur Abtrennung des Zielkerns von den Nebenprodukten werden also Separationsmethoden benötigt. Darüber hinaus müssen Messungen selbst bei geringer Statistik eine hohe Genauigkeit aufweisen, um auch für die exotischsten Kerne Rückschlüsse auf deren Struktur zu ermöglichen.

In dieser Arbeit wurden Verbesserungen und Messungen an zwei Experimenten an unterschiedlichen Beschleunigeranlagen durchgeführt. In beiden Experimenten wird ein an der Universität Gießen gebautes Multireflexions-Flugzeit-Massenspektrometer (*Multiple-Reflection Time-of-Flight Mass Spectrometer*; MR-TOF-MS) zur Massenmessung von exotischen Kernen eingesetzt. Am *FRS Ion Catcher* (FRS-IC) an der GSI in Darmstadt führten die Verbesserungen zu bisher unerreichten Messgenauigkeiten; an *TRIUMF's Ion Trap for Atomic and Nuclear sciences* (TITAN) am TRIUMF in Vancouver, Kanada, wurde eine neuartige Separationsmethode genutzt, um Messungen an bisher unbekannten Kernen zu ermöglichen. Im Rahmen dieser Messungen gelang es sogar, ein neues Isotop zu entdecken. Dies ist die erste Entdeckung eines neuen Isotops mit einem Flugzeitmassenspektrometer. Es können so also an bereits existierenden Teilchenbeschleunigern und Experimenten exotischere Kerne erreicht und studiert werden.

Am FRS-IC wurde eine neue modulare Software basierend auf dem LabVIEW Actor Framework zur Experimentsteuerung implementiert. Das neue Steuersystem ist besser skalierbar um zukünftige Erweiterungen schnell implementieren zu können, es bietet zudem eine größere Ausfallsicherheit und Stabilität. Am MR-TOF-MS des FRS-IC wurden das Detektorsystem erweitert und

stabilere Spannungsquellen verbaut. Durch das erweiterte Detektorsystem sind systematische Einstellungen der Systemparameter vorab ohne Verringerung der Messgenauigkeit im Experiment möglich; die stabileren Spannungsquellen verringern Schwankungen der Flugzeit und verbessern damit die Messgenauigkeit zusätzlich. Weitere technische Verbesserungen wurden in einer neu entwickelten Prozedur zur Ausrichtung des Ionenstrahls im MR-TOF-MS genutzt, die zu zuvor unerreicht hohen Massenauflösungsvermögen $m/\Delta m > 1\,000\,000$ (FWHM) führt. Bei geringer Statistik ist das Massenauflösungsvermögen ein entscheidender, limitierender Faktor für die Messgenauigkeit, daher kann so die Anforderung an die Ausbeute exotischer Kerne bei unverminderter Genauigkeitsforderung verringert werden. Das heißt, es können die Massen exotischerer Kerne ohne Einbußen bei der Genauigkeit gemessen werden. In Experimenten mit exotischen Kernen wurden durch die hier implementierten Verbesserungen bereits Genauigkeiten von $\delta m = 2.6\,\mathrm{keV}/c^2$ für ^{70}Se mit 485 Ereignissen und $22\,\mathrm{keV}/c^2$ für ^{69}As bei nur zehn detektierten Ionen erzielt. Im gleichen Experiment wurde die Masse des Moleküls $^{14}\mathrm{N}^{15}\mathrm{N}^{40}\mathrm{Ar}$ mit einer Genauigkeit von $1.1\,\mathrm{keV}/c^2$ gemessen, das entspricht einer mit MR-TOF-MS zuvor unerreichten relativen Massengenauigkeit $\delta m/m = 1.7 \times 10^{-8}$.

Am MR-TOF-MS des TITAN Experiments wurde der massenselektive Wiedereinfang von im Gerät selbst separierten Ionen erstmalig mit exotischen Kernen für direkte Massenmessungen genutzt, das heißt es wurde erstmals das selbe Gerät mit doppelter Funktionalität genutzt, nämlich sowohl als hochauflösender Massenseparator als auch als Präzisions-Massenspektrometer. Das Verfahren zum massenselektiven Wiedereinfang wurde vorab und unter online-Experimentbedingungen charakterisiert und in einem analytischen Modell beschrieben. Die neue Technik ermöglicht Messungen an Kernen die zuvor durch Isobare dominant überlagert und so verborgen waren. So wurden im Rahmen dieser Arbeit das neue Isotop ^{150}Yb entdeckt und die Anregungsenergie des Kernisomers in ^{151}Yb erstmals gemessen. Diese waren zuvor nicht nachweisbar, da beide Nuklide durch Nebenprodukte, zum Teil um fünf Größenordnungen häufiger erzeugt, überlagert waren. Mit den neuen Werten wurde die Kernstruktur neutronenarmer Lanthanoide nahe der Protonenabbruchkante und der abgeschlossenen $N = 82$ Neutronenschale weitab vom Stabilitätstal untersucht; die Schalenstruktur fernab des Stabilitätstals gehört zu den Schlüsselfragen der modernen Kernphysik. Die Kette der $N = 81$ Isomere mit gerader Protonenzahl wurde um einen Anregungsenergie-Messwert erweitert und in Zusammenarbeit mit einer Theoriegruppe analysiert. Die hier zuvor unverstandene weitgehende Konstanz der Anregungsenergien wurde durch unterschiedliche Deformationen in Grund- und angeregtem Zustand erklärt.

Acronyms

ADC analog-to-digital converter.

CSC Cryogenic Stopping Cell.
CSPP Control System ++.

EMG exponentially modified Gaussian.

FRS Fragment Separator.
FRS-IC FRS ion catcher.
FRSICC FRS ion catcher control.

hyper-EMG hyper-exponentially modified Gaussian.

ISAC Isotope Separator and Accelerator.
ISOL Isotope-Separation On-Line.
IT isochronous turn.

MR-TOF-MS Multiple-Reflection Time-of-Flight Mass Separator.
MR-TOF-MS Multiple-Reflection Time-of-Flight Mass Spectrometry.
MR-TOF-MS Multiple-Reflection Time-of-Flight Mass Spectrometer.
MRS Mass Range Selector.

RF radio-frequency.
RFQ RF quadrupole.
RFQ SY RFQ switchyard.
RIB rare isotope beams.

TFS time-focus shift.
TFST time-focus shift turn.
TITAN TRIUMF's Ion Trap for Atomic and Nuclear sciences.
TOF time of flight.
TRIUMF Tri University Meson Factory.

wMLE weighted maximum likelihood estimation.
WS Woods-Saxon.

Bibliography

Y. A. Akovali, K. S. Toth, A. L. Goodman, J. M. Nitschke, P. A. Wilmarth, D. M. Moltz, M. N. Rao, and D. C. Sousa. Single-particle states in ^{151}Tm and ^{151}Er: Systematics of neutron states in n=83 nuclei. *Phys. Rev. C*, 41:1126–1140, Mar 1990. doi: 10.1103/PhysRevC.41.1126. URL `https://link.aps.org/doi/10.1103/PhysRevC.41.1126`.

S. G. Alikhanov. A New Impulse Technique for Ion Mass Measurements. *Soviet Phys. JETP*, 4, 1957.

Ambiprobe. AmbiProbe. http://www.ambiprobe.net/, 2021. Last accessed Sep 2021.

F. W. Aston. Isotopes and atomic weights. *Nature*, 105(2646):617–619, 1920.

Georges Audi. The history of nuclidic masses and of their evaluation. *International Journal of Mass Spectrometry*, 251(2):85–94, 2006. ISSN 1387-3806. doi: https://doi.org/10.1016/j.ijms.2006.01.048. URL `https://www.sciencedirect.com/science/article/pii/S1387380606000820`.

Samuel Ayet San Andrés. *Developments for Multiple-Reflection Time-of-Flight Mass Spectrometers and Their Application to High-Resolution Accurate Mass Measurements of Short-Lived Exotic Nuclei*. PhD thesis, Justus Liebig University Gießen, 2018.

Samuel Ayet San Andrés, Christine Hornung, Jens Ebert, Wolfgang R. Plaß, Timo Dickel, Hans Geissel, Christoph Scheidenberger, Julian Bergmann, Florian Greiner, Emma Haettner, Christian Jesch, Wayne Lippert, Israel Mardor, Ivan Miskun, Zygmunt Patyk, Stephane Pietri, Alexander Pihktelev, Sivaji Purushothaman, Moritz P. Reiter, Ann-Kathrin Rink, Helmut Weick, Mikhail I. Yavor, Soumya Bagchi, Volha Charviakova, Paul Constantin, Marcel Diwisch, Andrew Finlay, Satbir Kaur, Ronja Knöbel, Johannes Lang, Bo Mei, Iain D. Moore, Jan-Hendrik Otto, Ilkka Pohjalainen, Andrej Prochazka, Christophe Rappold, Maya Takechi, Yoshiki K. Tanaka, John S. Winfield, and Xiaodong Xu. High-resolution, accurate multiple-reflection time-of-flight mass spectrometry for short-lived, exotic nuclei of a few events in their ground and low-lying isomeric states. *Phys. Rev. C*, 99:064313, Jun 2019a.

Samuel Ayet San Andrés, Christine Hornung, Jens Ebert, Wolfgang R. Plaß, Timo Dickel, Hans Geissel, Christoph Scheidenberger, Julian Bergmann, Flo-

rian Greiner, Emma Haettner, *et al.* High-resolution, accurate multiple-reflection time-of-flight mass spectrometry for short-lived, exotic nuclei of a few events in their ground and low-lying isomeric states. *Phys. Rev. C*, 99: 064313, Jun 2019b.

Sönke Beck, Brian Kootte, Irene Dedes, Timo Dickel, A. A. Kwiatkowski, Eleni Marina Lykiardopoulou, Wolfgang R. Plaß, Moritz P. Reiter, Corina Andreoiu, Julian Bergmann, Thomas Brunner, Dominique Curien, Jens Dilling, Jerzy Dudek, Eleanor Dunling, Jake Flowerdew, Abdelghafar Gaamouci, Leigh Graham, Gerald Gwinner, Andrew Jacobs, Renee Klawitter, Yang Lan, Erich Leistenschneider, Nikolay Minkov, Victor Monier, Ish Mukul, Stefan F. Paul, Christoph Scheidenberger, Robert I. Thompson, James L. Tracy, Michael Vansteenkiste, Hua-Lei Wang, Michael E. Wieser, Christian Will, and Jie Yang. Mass Measurements of Neutron-Deficient Yb Isotopes and Nuclear Structure at the Extreme Proton-Rich Side of the $N = 82$ Shell. *Phys. Rev. Lett.*, 127:112501, Sep 2021. doi: 10.1103/PhysRevLett.127.112501. URL `https://link.aps.org/doi/10.1103/PhysRevLett.127.112501`.

J. Bergmann. PhD. thesis in preparation.

H. A. Bethe and R. F. Bacher. Nuclear Physics A. Stationary States of Nuclei. *Rev. Mod. Phys.*, 8(2):82, 1936.

K. Blaum. High-accuracy mass spectrometry with stored ions. *Phys. Rep.*, 425: 1–78, 2006.

K. Blaum, J. Dilling, and W. Nörtershäuser. Precision atomic physics techniques for nuclear physics with radioactive beams. *Phys. Scr.*, T152:014017, 2013.

M. Bolsterli, E. O. Fiset, J. R. Nix, and J. L. Norton. New calculation of fission barriers for heavy and superheavy nuclei. *Phys. Rev. C*, 5:1050–1077, Mar 1972. doi: 10.1103/PhysRevC.5.1050. URL `https://link.aps.org/doi/10.1103/PhysRevC.5.1050`.

M. Brack, Jens Damgaard, A. S. Jensen, H. C. Pauli, V. M. Strutinsky, and C. Y. Wong. Funny hills: The shell-correction approach to nuclear shell effects and its applications to the fission process. *Rev. Mod. Phys.*, 44:320–405, Apr 1972. doi: 10.1103/RevModPhys.44.320. URL `https://link.aps.org/doi/10.1103/RevModPhys.44.320`.

Holger Brand and Dennis Neidherr. CS++: Class libraries extending the NI Actor Framework and native LabVIEW classes., 2021. URL https://git.gsi.de/EE-LV/CSPP.

H. Brandt. FRSICC launcher actor (private communication), 2020.

P. Bricault, F. Ames, M. Dombsky, P. Kunz, F. Labrecque, J. Lassen, A. Mjos, G. Minor, and A. Teigelhöfer. Recent developments of the ion sources at Tri University Meson Factory/Isotope Separator and ACcelerator Facility. *Rev. Sci. Instrum.*, 83:02A914, 2012.

Pierre Bricault, Richard Baartman, Marik Dombsky, Andrew Hurst, Clive Mark, Guy Stanford, and Paul Schmor. TRIUMF-ISAC target station and mass separator commissioning. *Nucl. Phys. A*, 701(1):49–53, 2002. ISSN 0375-9474. doi: https://doi.org/10.1016/S0375-9474(01)01546-9. URL https://www.sciencedirect.com/science/article/pii/S0375947401015469.

T. Brunner, M. J. Smith, M. Brodeur, S. Ettenauer, A. T. Gallant, V. V. Simon, A. Chaudhuri, A. Lapierre, E. Mane, R. Ringle, *et al.* TITAN's digital RFQ ion beam cooler and buncher, operation and performance. *Nucl. Instrum. Methods A*, 676:32–43, 2012.

E. M. Burbidge, G. R. Burbidge, W. A. Fowler, and F. Hoyle. Synthesis of the elements in stars. *Rev. Mod. Phys.*, 29(4):547–650, Oct 1957. doi: 10.1103/RevModPhys.29.547.

I. Bylinskii and M.K. Craddock. The triumf 500 mev cyclotron: the driver accelerator. *Hyperfine Interactions*, 225:9–16, 2014. URL https://doi.org/10.1007/s10751-013-0878-6.

James Chadwick. Possible existence of a neutron. *Nature*, 129:312, 1932a. doi: 10.1038/129312a0.

James Chadwick. The existence of a neutron. *Proc. R. Soc. Lond. A*, 136:692–708, 1932b. doi: 10.1098/rspa.1932.0112.

S. Cwiok, J. Dudek, W. Nazarewicz, J. Skalski, and T. Werner. Single-particle energies, wave functions, quadrupole moments and g-factors in an axially deformed woods-saxon potential with applications to the two-centre-type nuclear problems. *Computer Physics Communications*, 46(3):379 – 399, 1987. doi: https://doi.org/10.1016/0010-4655(87)90093-2.

M. J. A. de Voigt, J. Dudek, and Z. Szymanski. High-spin phenomena in atomic nuclei. *Rev. Mod. Phys.*, 55:949–1046, Oct 1983. doi: 10.1103/RevModPhys.55.949.

I. Dedes. Nuclear mean-field calculations for investigating the $j^\pi = 11/2^-$, odd-a $n = 81$ isomers. (private communication), 2021.

I. Dedes and J. Dudek. Propagation of the nuclear mean-field uncertainties with increasing distance from the parameter adjustment zone: Applications to superheavy nuclei. *Phys. Rev. C*, 99:054310, May 2019. doi: 10.1103/PhysRevC.99.054310.

T. Dickel. *Design and Commissioning of an Ultra-High-Resolution Time-of-Flight Based Isobar Separator and Mass Spectrometer*. PhD thesis, Justus Liebig University Gießen, 2010.

T. Dickel. Beam alignment by splitting one 4d problem into two easier-to-handle 2d problems. (private communication), 2016.

T. Dickel, W. R. Plaß, J. Lang, J. Ebert, H. Geissel, E. Haettner, C. Jesch, W. Lippert, M. Petrick, C. Scheidenberger, and M. I. Yavor. Multiple-reflection time-of-flight mass spectrometry for in situ applications. *Nucl. Instrum. Methods B*, 317:779–784, 2013.

T. Dickel, W. R. Plaß, S. Ayet San Andrés, J. Ebert, H. Geissel, E. Haettner, C. Hornung, I. Miskun, S. Pietri, S. Purushothaman, M. P. Reiter, A. K. Rink, C. Scheidenberger, H. Weick, P. Dendooven, M. Diwisch, F. Greiner, F. Heiße, R. Knöbel, W. Lippert, I. D. Moore, I. Pohjalainen, A. Prochazka, M. Ranjan, M. Takechi, J. S. Winfield, and X. Xu. First spatial separation of a heavy ion isomeric beam with a multiple-reflection time-of-flight mass spectrometer. *Phys. Lett. B*, 744:137–141, 2015a.

T. Dickel, W. R. Plaß, A. Becker, U. Czok, H. Geissel, E. Haettner, C. Jesch, W. Kinsel, M. Petrick, C. Scheidenberger, and M. I. Yavor. A high-performance multiple-reflection time-of-flight mass spectrometer and isobar separator for the research with exotic nuclei. *Nucl. Instrum. Methods A*, 777: 172–188, 2015b.

T. Dickel, M. I. Yavor, J. Lang, W. R. Plaß, W. Lippert, H. Geissel, and C. Scheidenberger. Dynamical time focus shift in multiple-reflection time-of-flight mass spectrometers. *Int. J. Mass Spectrom.*, 412:1–7, 2017a.

Timo Dickel, Wolfgang R. Plaß, Wayne Lippert, Johannes Lang, Mikhail I. Yavor, Hans Geissel, and Christoph Scheidenberger. Isobar separation in

a multiple-reflection time-of-flight mass spectrometer by mass-selective retrapping. *J. Am. Soc. Mass Spectrom.*, 28(6):1079–1090, Jun 2017b.

Timo Dickel, Samuel Ayet San Andres, Soenke Beck, Julian Bergmann, Jens Dilling, Florian Greiner, Christine Hornung, Andrew Jacobs, Gabriella Kripko-Koncz, Ania Kwiatkowski, Erich Leistenschneider, Alexander Pikthtelev, Wolfgang R. Plass, Moritz P. Reiter, Christoph Scheidenberger, and Christian Will. Recent upgrades of the multiple-reflection time-of-flight mass spectrometer at TITAN, TRIUMF. *Hyperfine Interact.*, 240:62, 2019a.

Timo Dickel, Samuel Ayet San Andres, Soenke Beck, Julian Bergmann, Jens Dilling, Florian Greiner, Christine Hornung, Andrew Jacobs, Gabriella Kripko-Koncz, Ania Kwiatkowski, *et al.* Recent upgrades of the multiple-reflection time-of-flight mass spectrometer at TITAN, TRIUMF. *Hyperfine Interact.*, 240, 2019b.

J. Dilling, R. Baartman, P. Bricault, M. Brodeur, L. Blomeley, F. Buchinger, J. Crawford, J. R. Crespo Lopez-Urrutia, P. Delheij, M. Froese, *et al.* Mass measurements on highly charged radioactive ions, a new approach to high precision with TITAN. *Int. J. Mass Spectrom.*, 251:198–203, 2006.

J. Dilling, R. Krücken, and G. C. Ball. ISAC overview. *Hyperfine Interactions*, 225:1–8, 2014. URL `https://doi.org/10.1007/s10751-013-0877-7`.

Jens Dilling, Klaus Blaum, Maxime Brodeur, and Sergey Eliseev. Penning-trap mass measurements in atomic and nuclear physics. *Annual Review of Nuclear and Particle Science*, 68(1):45–74, 2018. doi: 10.1146/annurev-nucl-102711-094939. URL `https://doi.org/10.1146/annurev-nucl-102711-094939`.

M. Dombsky, D. Bishop, P. Bricault, D. Dale, A. Hurst, K. Jayamanna, R. Keitel, M. Olivo, P. Schmor, and G. Stanford. Commissioning and initial operation of a radioactive beam ion source at ISAC. *Rev. Sci. Instrum.*, 71(3): 978, 2000.

J. Dudek and T. Werner. New parameters of the deformed woods-saxon potential for a= 110-210 nuclei. *J. Phys. G: Nucl. Phys.*, 4(10):1543, 1978a.

J Dudek and T Werner. New parameters of the deformed woods-saxon potential for $a = 110 - 210$ nuclei. *Journal of Physics G: Nuclear Physics*, 4(10):1543–1561, oct 1978b. doi: 10.1088/0305-4616/4/10/006.

J. Dudek, A. Majhofer, J. Skalski, T. Werner, S. Cwiok, and W. Nazarewicz. Parameters of the deformed woods-saxon potential outside a= 110-210 nuclei. *J. Phys. G: Nucl. Phys.*, 5(10):1359, 1979a.

J Dudek, A Majhofer, J Skalski, T Werner, S Cwiok, and W Nazarewicz. Parameters of the deformed woods-saxon potential outside $a = 110 - 210$ nuclei. *Journal of Physics G: Nuclear Physics*, 5(10):1359–1381, oct 1979b. doi: 10.1088/0305-4616/5/10/014.

J. Dudek, W. Nazarewicz, and T. Werner. Discussion of the improved parametrisation of the woods-saxon potential for deformed nuclei. *Nucl. Phys. A*, 341(2):253–268, 1980a.

J. Dudek, W. Nazarewicz, and T. Werner. Discussion of the improved parametrisation of the woods-saxon potential for deformed nuclei. *Nuclear Physics A*, 341(2):253 – 268, 1980b. doi: https://doi.org/10.1016/0375-9474(80)90312-7.

J. Dudek, Z. Szymański, and T. Werner. Woods-saxon potential parameters optimized to the high spin spectra in the lead region. *Phys. Rev. C*, 23: 920–925, Feb 1981. doi: 10.1103/PhysRevC.23.920.

W. M. Elsasser. Sur le principe de Pauli dans les noyaux. *J. Phys. Radium*, 4 (10):549–556, 1933. doi: 10.1051/jphysrad:01933004010054900. URL `https://hal.archives-ouvertes.fr/jpa-00233175`.

W.M. Elsasser. Sur le principe de Pauli dans les noyaux - II. *J. Phys. Radium*, 5(8):389–397, 1934. doi: 10.1051/jphysrad:0193400508038900. URL `https://hal.archives-ouvertes.fr/jpa-00233250`.

Timur V. Elzhov, Katharine M. Mullen, Andrej-Nikolai Spiess, and Ben Bolker. *minpack.lm: R Interface to the Levenberg-Marquardt Nonlinear Least-Squares Algorithm Found in MINPACK, Plus Support for Bounds*, 2016. URL `https://CRAN.R-project.org/package=minpack.lm`. R package version 1.2-1.

ENSDF. From ENSDF database as of October, 2020. https://www.nndc.bnl.gov/ensarchivals/, 2020. Last accessed Apr 2021.

J. Erler, N. Birge, M. Kortelainen, W. Nazarewicz, E. Olsen, A. M. Perhac, and M. Stoitsov. The limits of the nuclear landscape. *Nature*, 486:509–512, 2012.

A. T. Gallant, J. C. Bale, T. Brunner, U. Chowdhury, S. Ettenauer, A. Lennarz, D. Robertson, V. V. Simon, A. Chaudhuri, J. D. Holt, A. A. Kwiatkowski,

E. Mané, J. Menéndez, B. E. Schultz, M. C. Simon, C. Andreoiu, P. Delheij, M. R. Pearson, H. Savajols, A. Schwenk, and J. Dilling. New precision mass measurements of neutron-rich calcium and potassium isotopes and three-nucleon forces. *Phys. Rev. Lett.*, 109:032506, Jul 2012. doi: 10.1103/PhysRevLett.109.032506. URL `https://link.aps.org/doi/10.1103/PhysRevLett.109.032506`.

G. Gamow. Mass defect curve and nuclear constitution. *Proc. R. Soc. London*, 126(803):632–644, 1930.

H. Geissel, P. Armbruster, K. H. Behr, A. Brünle, K. Burkard, M. Chen, H. Folger, B. Franczak, H. Keller, O. Klepper, B. Langenbeck, F. Nickel, E. Pfeng, M. Pfützner, E. Roeckl, K. Rykaczewski, I. Schall, D. Schardt, C. Scheidenberger, K. H. Schmidt, A. Schröter, T. Schwab, K. Sümmerer, M. Weber, G. Münzenberg, T. Brohm, H. G. Clerc, M. Fauerbach, J. J. Gaimard, A. Grewe, E. Hanelt, B. Knödler, M. Steiner, B. Voss, J. Weckenmann, C. Ziegler, A. Magel, H. Wollnik, J. P. Dufour, Y. Fujita, D. J. Vieira, and B. Sherrill. The GSI projectile fragment separator (FRS): a versatile magnetic system for relativistic heavy ions. *Nucl. Instrum. Methods B*, 70 (1-4):286 – 297, 1992.

S. Goriely, N. Chamel, and J. M. Pearson. Further explorations of skyrme-hartree-fock-bogoliubov mass formulas. xii. stiffness and stability of neutron-star matter. *Phys. Rev. C*, 82:035804, Sep 2010. doi: 10.1103/PhysRevC.82.035804. URL `https://link.aps.org/doi/10.1103/PhysRevC.82.035804`.

F. Greiner, T. Dickel, S. Ayet San Andrés, J. Bergmann, P. Constantin, J. Ebert, H. Geissel, E. Haettner, C. Hornung, I. Miskun, W. Lippert, I. Mardor, I. Moore, W.R. Plaß, S. Purushothaman, A.-K. Rink, M.P. Reiter, C. Scheidenberger, and H. Weick. Removal of molecular contamination in low-energy RIBs by the isolation–dissociation–isolation method. *Nucl. Instrum. Methods B*, 463:324–326, 2020.

GSI Helmholtzzentrum für Schwerionenforschung. GSI – Accelerator Facility. online, 2021. URL `https://www.gsi.de/en/researchaccelerators/accelerator_facility`.

Otto Haxel, J. Hans D. Jensen, and Hans E. Suess. On the "magic numbers" in nuclear structure. *Phys. Rev.*, 75:1766–1766, Jun 1949. doi: 10.1103/PhysRev.75.1766.2. URL `https://link.aps.org/doi/10.1103/PhysRev.75.1766.2`.

K. Heyde and P. J. Brussaard. Neutron hole states in the $N = 81$ nuclei. *Zeitschrift für Physik A Hadrons and nuclei*, 259(1):15–36, Feb 1973. ISSN 0939-7922. doi: 10.1007/BF01394476. URL https://doi.org/10.1007/BF01394476.

T. Y. Hirsh, N. Paul, M. Burkey, A. Aprahamian, F. Buchinger, S. Caldwell, J. A. Clark, A. F. Levand, L. L. Ying, S. T. Marley, *et al.* First operation and mass separation with the CARIBU MR-TOF. *Nucl. Instrum. Methods B*, 376:229–232, 2016.

C. Hornung. *High-Resolution Experiments with the Multiple-Reflection Time-Of-Flight Mass Spectrometer at the Fragment Separator FRS*. PhD thesis, Justus Liebig University Gießen, 2018.

Christine Hornung, Daler Amanbayev, Irene Dedes, Gabriella Kripko-Koncz, Ivan Miskun, Noritaka Shimizu, Samuel Ayet San Andrés, Julian Bergmann, Timo Dickel, Jerzy Dudek, Jens Ebert, Hans Geissel, Magdalena Górska, Hubert Grawe, Florian Greiner, Emma Haettner, Takaharu Otsuka, Wolfgang R. Plaß, Sivaji Purushothaman, Ann-Kathrin Rink, Christoph Scheidenberger, Helmut Weick, Soumya Bagchi, Andrey Blazhev, Olga Charviakova, Dominique Curien, Andrew Finlay, Satbir Kaur, Wayne Lippert, Jan-Hendrik Otto, Zygmunt Patyk, Stephane Pietri, Yoshiki K. Tanaka, Yusuke Tsunoda, and John S. Winfield. Isomer studies in the vicinity of the doubly-magic nucleus ^{100}Sn: Observation of a new low-lying isomeric state in ^{97}Ag. *Phys. Lett. B*, 802:135200, 2020.

Y. Ito, P. Schury, M. Wada, F. Arai, H. Haba, Y. Hirayama, S. Ishizawa, D. Kaji, S. Kimura, H. Koura, M. MacCormick, H. Miyatake, J. Y. Moon, K. Morimoto, K. Morita, M. Mukai, I. Murray, T. Niwase, K. Okada, A. Ozawa, M. Rosenbusch, A. Takamine, T. Tanaka, Y. X. Watanabe, H. Wollnik, and S. Yamaki. First direct mass measurements of nuclides around $Z = 100$ with a multireflection time-of-flight mass spectrograph. *Phys. Rev. Lett.*, 120:152501, Apr 2018.

C. Izzo, J. Bergmann, K. A. Dietrich, E. Dunling, D. Fusco, A. Jacobs, B. Kootte, G. Kripkó-Koncz, Y. Lan, E. Leistenschneider, E. M. Lykiardopoulou, I. Mukul, S. F. Paul, M. P. Reiter, J. L. Tracy, C. Andreoiu, T. Brunner, T. Dickel, J. Dilling, I. Dillmann, G. Gwinner, D. Lascar, K. G. Leach, W. R. Plaß, C. Scheidenberger, M. E. Wieser, and A. A. Kwiatkowski. Mass measurements of neutron-rich indium isotopes for r-process studies. *Phys. Rev. C*, 103:025811, Feb 2021. doi: 10.1103/PhysRevC.103.025811. URL https://link.aps.org/doi/10.1103/PhysRevC.103.025811.

Andrew Jacobs. *Collision induced dissociation and mass spectrometry with the TITAN Multiple-Reflection Time-of-Flight Mass-Spectrometer*. Master thesis, University of British Columbia, 2019. URL https://open.library.ubc.ca/collections/ubctheses/24/items/1.0380561.

Ashok Kumar Jain, Bhoomika Maheshwari, and Alpana Goel. *Nuclear Isomers*. Springer, Cham, 1 edition, 2021. doi: https://doi.org/10.1007/978-3-030-78675-5.

C. Jesch. *The Multiple-Reflection Time-of-Flight Isobar Separator for TITAN and Direct Mass Measurements at the FRS Ion Catcher*. PhD thesis, Justus Liebig University Gießen, 2016.

C. Jesch, T. Dickel, W. R. Plaß, D. Short, S. Ayet San Andres, J. Dilling, H. Geissel, F. Greiner, J. Lang, K. G. Leach, W. Lippert, C. Scheidenberger, and M. I. Yavor. The MR-TOF-MS isobar separator for the TITAN facility at TRIUMF. *Hyperfine Interact.*, 235:97–106, 2015.

Joshua T. Johnson, Ian J. Carrick, Gregory S. Eakins, and Scott A. McLuckey. Mirror switching for high-resolution ion isolation in an electrostatic linear ion trap. *Anal. Chem.*, 91(14):8789–8794, Jul 2019. ISSN 0003-2700. doi: 10.1021/acs.analchem.9b00874. URL https://doi.org/10.1021/acs.analchem.9b00874.

R. Kanungo. A new view of nuclear shells. *Phys. Scripta*, T152:014002, 2013.

P. Kleinheinz, B. Rubio, M. Ogawa, M. Piiparinen, A. Plochocki, D. Schardt, R. Barden, O. Klepper, R. Kirchner, and E. Roeckl. Beta-decay of ^{151}Yb. *Z. Phys. A*, 322:705–706, 1985.

R. Knöbel, M. Diwisch, F. Bosch, D. Boutin, L. Chen, C. Dimopoulou, A. Dolinskii, B. Franczak, B. Franzke, H. Geissel, M. Hausmann, C. Kozhuharov, J. Kurcewicz, S.A. Litvinov, G. Martinez-Pinedo, M. Matoš, M. Mazzocco, G. Münzenberg, S. Nakajima, C. Nociforo, F. Nolden, T. Ohtsubo, A. Ozawa, Z. Patyk, W.R. Plaß, C. Scheidenberger, J. Stadlmann, M. Steck, B. Sun, T. Suzuki, P.M. Walker, H. Weick, M.-R. Wu, M. Winkler, and T. Yamaguchi. First direct mass measurements of stored neutron-rich ^{129,130,131}Cd isotopes with FRS-ESR. *Physics Letters B*, 754:288–293, 2016. ISSN 0370-2693. doi: https://doi.org/10.1016/j.physletb.2016.01.039. URL https://www.sciencedirect.com/science/article/pii/S0370269316000563.

Takeshi Kodama. β-Stability Line and Liquid-Drop Mass Formulas. *Progress of Theoretical Physics*, 45(4):1112–1122, 04 1971. ISSN 0033-068X. doi: 10.1143/PTP.45.1112. URL https://doi.org/10.1143/PTP.45.1112.

F.G. Kondev, M. Wang, W.J. Huang, S. Naimi, and G. Audi. The NUBASE2020 evaluation of nuclear physics properties *. *Chin. Phys. C*, 45(3):030001, mar 2021. doi: 10.1088/1674-1137/abddae. URL https://doi.org/10.1088/1674-1137/abddae.

Markus Kortelainen, Thomas Lesinski, J Moré, W Nazarewicz, J Sarich, N Schunck, M. V. Stoitsov, and S Wild. Nuclear energy density optimization. *Phys. Rev. C*, 82(2):024313, 2010.

K. Kotajima and H. Morinaga. Isomers in $N = 81$ nuclei. *Nuclear Physics*, 16(2):231–245, 1960. ISSN 0029-5582. doi: https://doi.org/10.1016/S0029-5582(60)81034-6. URL https://www.sciencedirect.com/science/article/pii/S0029558260810346.

G. Kripkó-Koncz. PhD. thesis in preparation.

Johannes Sebastian Lang. *Development of a Mobile High-Resolution Multiple-Reflection Time-of-Flight Mass Spectrometer for In-Situ Life Science Application*. PhD thesis, Justus Liebig University Gießen, 2016.

E. Leistenschneider, M. P. Reiter, S. Ayet San Andrés, B. Kootte, J. D. Holt, P. Navrátil, C. Babcock, C. Barbieri, B. R. Barquest, J. Bergmann, J. Bollig, T. Brunner, E. Dunling, A. Finlay, H. Geissel, L. Graham, F. Greiner, H. Hergert, C. Hornung, C. Jesch, R. Klawitter, Y. Lan, D. Lascar, K. G. Leach, W. Lippert, J. E. McKay, S. F. Paul, A. Schwenk, D. Short, J. Simonis, V. Somà, R. Steinbrügge, S. R. Stroberg, R. Thompson, M. E. Wieser, C. Will, M. Yavor, C. Andreoiu, T. Dickel, I. Dillmann, G. Gwinner, W. R. Plaß, C. Scheidenberger, A. A. Kwiatkowski, and J. Dilling. Dawning of the $N = 32$ shell closure seen through precision mass measurements of neutron-rich titanium isotopes. *Phys. Rev. Lett.*, 120:062503, Feb 2018.

E. Leistenschneider, E. Dunling, G. Bollen, B. A. Brown, J. Dilling, A. Hamaker, J. D. Holt, A. Jacobs, A. A. Kwiatkowski, T. Miyagi, W. S. Porter, D. Puentes, M. Redshaw, M. P. Reiter, R. Ringle, R. Sandler, C. S. Sumithrarachchi, A. A. Valverde, and I. T. Yandow. Precision mass measurements of neutron-rich scandium isotopes refine the evolution of $N = 32$ and $N = 34$ shell closures. *Phys. Rev. Lett.*, 126:042501, Jan 2021. doi: 10.1103/PhysRevLett.126.042501. URL https://link.aps.org/doi/10.1103/PhysRevLett.126.042501.

Yu. A. Litvinov, H. Geissel, T. Radon, F. Attallah, G. Audi, K. Beckert, F. Bosch, M. Falch, B. Franzke, M. Hausmann, M. Hellström, Th. Kerscher, O. Klepper, H.-J. Kluge, C. Kozhuharov, K. E. G. Löbner, G. Münzenberg,

F. Nolden, Yu. N. Novikov, W. Quint, Z. Patyk, H. Reich, C. Scheidenberger, B. Schlitt, M. Steck, K. Sümmerer, L. Vermeeren, M. Winkler, Th. Winkler, and H. Wollnik. Mass measurement of cooled neutron-deficient bismuth projectile fragments with time-resolved Schottky mass spectrometry at the FRS-ESR facility. *Nucl. Phys. A*, 756:3–38, 2005.

D. Lunney, J. M. Pearson, and C. Thibault. Recent trends in the determination of nuclear masses. *Rev. Mod. Phys.*, 75(3):1021–1062, 2003.

E. M. Lykiardopoulou, G. Audi, T. Dickel, W. J. Huang, D. Lunney, Wolfgang R. Plaß, M. P. Reiter, J. Dilling, and A. A. Kwiatkowski. Exploring the limits of existence of proton-rich nuclei in the $z = 70 - -82$ region. *Phys. Rev. C*, 107:024311, Feb 2023. doi: 10.1103/PhysRevC.107.024311. URL `https://link.aps.org/doi/10.1103/PhysRevC.107.024311`.

V. Manea, J. Karthein, D. Atanasov, M. Bender, K. Blaum, T. E. Cocolios, S. Eliseev, A. Herlert, J. D. Holt, W. J. Huang, Yu. A. Litvinov, D. Lunney, J. Menéndez, M. Mougeot, D. Neidherr, L. Schweikhard, A. Schwenk, J. Simonis, A. Welker, F. Wienholtz, and K. Zuber. First glimpse of the $N = 82$ shell closure below $Z = 50$ from masses of neutron-rich cadmium isotopes and isomers. *Phys. Rev. Lett.*, 124:092502, Mar 2020. doi: 10.1103/PhysRevLett.124.092502. URL `https://link.aps.org/doi/10.1103/PhysRevLett.124.092502`.

Manura, D. and Dahl D. *SIMION® 8.0 User Manual*. Scientific Instrument Services Inc, Ringoes, NJ., 2008.

I. Mardor, S. Ayet San Andrés, T. Dickel, D. Amanbayev, S. Beck, J. Bergmann, H. Geissel, L. Gröf, E. Haettner, C. Hornung, N. Kalantar-Nayestanaki, G. Kripko-Koncz, I. Miskun, A. Mollaebrahimi, W. R. Plaß, C. Scheidenberger, H. Weick, Soumya Bagchi, D. L. Balabanski, A. A. Bezbakh, Z. Brencic, O. Charviakova, V. Chudoba, Paul Constantin, M. Dehghan, A. S. Fomichev, L. V. Grigorenko, O. Hall, M. N. Harakeh, J.-P. Hucka, A. Kankainen, O. Kiselev, R. Knöbel, D. A. Kostyleva, S. A. Krupko, N. Kurkova, N. Kuzminchuk, I. Mukha, I. A. Muzalevskii, D. Nichita, C. Nociforo, Z. Patyk, M. Pfützner, S. Pietri, S. Purushothaman, M. P. Reiter, H. Roesch, F. Schirru, P. G. Sharov, A. Spătaru, G. Stanic, A. State, Y. K. Tanaka, M. Vencelj, M. I. Yavor, and J. Zhao. Mass measurements of As, Se, and Br nuclei, and their implication on the proton-neutron interaction strength toward the $N = Z$ line. *Phys. Rev. C*, 103:034319, Mar 2021. doi: 10.1103/PhysRevC.103.034319. URL `https://link.aps.org/doi/10.1103/PhysRevC.103.034319`.

Maria G. Mayer. On closed shells in nuclei. *Phys. Rev.*, 74:235–239, Aug 1948. doi: 10.1103/PhysRev.74.235. URL https://link.aps.org/doi/10.1103/PhysRev.74.235.

Maria Goeppert Mayer. On closed shells in nuclei. ii. *Phys. Rev.*, 75:1969–1970, Jun 1949. doi: 10.1103/PhysRev.75.1969. URL https://link.aps.org/doi/10.1103/PhysRev.75.1969.

S. Michimasa, M. Kobayashi, Y. Kiyokawa, S. Ota, D. S. Ahn, H. Baba, G. P. A. Berg, M. Dozono, N. Fukuda, T. Furuno, E. Ideguchi, N. Inabe, T. Kawabata, S. Kawase, K. Kisamori, K. Kobayashi, T. Kubo, Y. Kubota, C. S. Lee, M. Matsushita, H. Miya, A. Mizukami, H. Nagakura, D. Nishimura, H. Oikawa, H. Sakai, Y. Shimizu, A. Stolz, H. Suzuki, M. Takaki, H. Takeda, S. Takeuchi, H. Tokieda, T. Uesaka, K. Yako, Y. Yamaguchi, Y. Yanagisawa, R. Yokoyama, K. Yoshida, and S. Shimoura. Magic nature of neutrons in ^{54}Ca: First mass measurements of $^{55-57}$Ca. *Phys. Rev. Lett.*, 121:022506, Jul 2018. doi: 10.1103/PhysRevLett.121.022506. URL https://link.aps.org/doi/10.1103/PhysRevLett.121.022506.

P. Möller, A. J. Sierk, T. Ichikawa, and H. Sagawa. Nuclear ground-state masses and deformations: FRDM(2012). *At. Data Nucl. Data Tables*, 109: 1–204, 2016.

J. J Moré. The Levenberg-Marquardt algorithm: implementation and theory. In *Numerical analysis*, pages 105–116. Springer, 1978.

I. Mukul, C. Andreoiu, J. Bergmann, M. Brodeur, T. Brunner, K. A. Dietrich, T. Dickel, I. Dillmann, E. Dunling, D. Fusco, G. Gwinner, C. Izzo, A. Jacobs, B. Kootte, Y. Lan, E. Leistenschneider, E. M. Lykiardopoulou, S. F. Paul, M. P. Reiter, J. L. Tracy, J. Dilling, and A. A. Kwiatkowski. Examining the nuclear mass surface of rb and sr isotopes in the $a \approx 104$ region via precision mass measurements. *Phys. Rev. C*, 103:044320, Apr 2021. doi: 10.1103/PhysRevC.103.044320. URL https://link.aps.org/doi/10.1103/PhysRevC.103.044320.

J. W. Negele. The mean-field theory of nuclear structure and dynamics. *Rev. Mod. Phys.*, 54:913–1015, Oct 1982. doi: 10.1103/RevModPhys.54.913. URL https://link.aps.org/doi/10.1103/RevModPhys.54.913.

J. A. Nelder and R. Mead. A Simplex Method for Function Minimization. *The Computer Journal*, 7(4):308–313, 01 1965. ISSN 0010-4620. doi: 10.1093/comjnl/7.4.308. URL https://doi.org/10.1093/comjnl/7.4.308.

Léo Neufcourt, Yuchen Cao, Samuel Giuliani, Witold Nazarewicz, Erik Olsen, and Oleg B. Tarasov. Beyond the proton drip line: Bayesian analysis of proton-emitting nuclei. *Phys. Rev. C*, 101:014319, Jan 2020. doi: 10.1103/PhysRevC.101.014319. URL https://link.aps.org/doi/10.1103/PhysRevC.101.014319.

R. Neugart and G. Neyens. *Nuclear Moments*. 2006. doi: 10.1007/b11743651. URL https://www.euroschoolonexoticbeams.be/files/nlp/LNP700_contrib4.pdf.

W. Ogle, S. Wahlborn, R. Piepenbring, and S. Fredriksson. Single-particle levels of nonspherical nuclei in the region $150 < a < 190$. *Rev. Mod. Phys.*, 43:424–478, Jul 1971. doi: 10.1103/RevModPhys.43.424. URL https://link.aps.org/doi/10.1103/RevModPhys.43.424.

S. F. Paul, J. Bergmann, J. D. Cardona, K. A. Dietrich, E. Dunling, Z. Hockenbery, C. Hornung, C. Izzo, A. Jacobs, A. Javaji, B. Kootte, Y. Lan, E. Leistenschneider, E. M. Lykiardopoulou, I. Mukul, T. Murböck, W. S. Porter, R. Silwal, M. B. Smith, J. Ringuette, T. Brunner, T. Dickel, I. Dillmann, G. Gwinner, M. MacCormick, M. P. Reiter, H. Schatz, N. A. Smirnova, J. Dilling, and A. A. Kwiatkowski. Mass measurements of $^{60--63}$Ga reduce x-ray burst model uncertainties and extend the evaluated $t = 1$ isobaric multiplet mass equation. *Phys. Rev. C*, 104:065803, Dec 2021. doi: 10.1103/PhysRevC.104.065803. URL https://link.aps.org/doi/10.1103/PhysRevC.104.065803.

M. Pfützner, M. Karny, L. V. Grigorenko, and K. Riisager. Radioactive decays at limits of nuclear stability. *Rev. Mod. Phys.*, 84(2):567, 2012.

A. Pikhtelev. MAc mass analyzer control and DAQ software, 2010-2015.

W. R. Plaß, T. Dickel, U. Czok, H. Geissel, M. Petrick, K. Reinheimer, C. Scheidenberger, and M. I. Yavor. Isobar separation by time-of-flight mass spectrometry for low-energy radioactive ion beam facilities. *Nucl. Instrum. Methods B*, 266:4560–4564, 2008.

W. R. Plaß, T. Dickel, S. Purushothaman, P. Dendooven, H. Geissel, J. Ebert, E. Haettner, C. Jesch, M. Ranjan, M. P. Reiter, H. Weick, F. Amjad, S. Ayet, M. Diwisch, A. Estrade, F. Farinon, F. Greiner, N. Kalantar-Nayestanaki, R. Knöbel, J. Kurcewicz, J. Lang, I. Moore, I. Mukha, C. Nociforo, M. Petrick, M. Pfuetzner, S. Pietri, A. Prochazka, A.-K. Rink, S. Rinta-Antila, D. Schäfer, C. Scheidenberger, M. Takechi, Y. K. Tanaka, J. S. Winfield,

and M. I. Yavor. The FRS Ion Catcher - a facility for high-precision experiments with stopped projectile and fission fragments. *Nucl. Instrum. Methods B*, 317:457–462, 2013a.

W. R. Plaß, T. Dickel, and C. Scheidenberger. Multiple-reflection time-of-flight mass spectrometry. *Int. J. Mass Spectrom.*, 349:134–144, 2013b.

W. R. Plaß, T. Dickel, S. Ayet San Andrés, J. Ebert, F. Greiner, C. Hornung, C. Jesch, J. Lang, W. Lippert, T. Majoros, D. Short, H. Geissel, E. Haettner, M. P. Reiter amd A.-K. Rink, C. Scheidenberger, and M. I. Yavor. High-performance multiple-reflection time-of-flight mass spectrometers for research with exotic nuclei and for analytical mass spectrometry. *Phys. Scr. T*, 166: 014069, 2015.

Wolfgang R Plaß, Timo Dickel, Israel Mardor, Stephane Pietri, Hans Geissel, Christoph Scheidenberger, Daler Amanbayev, Samuel Ayet San Andrés, Juha Äystö, Dimiter L Balabanski, *et al.* The science case of the FRS Ion Catcher for FAIR Phase-0. *Hyperfine Interact.*, 240(1):73, 2019.

S. Purushothaman, M. P. Reiter, E. Haettner, P. Dendooven, T. Dickel, H. Geissel, J. Ebert, C. Jesch, W. R. Plaß, M. Ranjan, H. Weick, F. Amjad, S. Ayet, M. Diwisch, A. Estrade, F. Farinon, F. Greiner, N. Kalantar-Nayestanaki, R. Knöbel, J. Kurcewicz, J. Lang, I. Moore, I. Mukha, C. Nociforo, M. Petrick, M. Pfuetzner, S. Pietri, A. Prochazka, A.-K. Rink, S. Rinta-Antila, C. Scheidenberger, M. Takechi, Y. K. Tanaka, J. S. Winfield, and M. I. Yavor. First online results of a cryogenic stopping cell with short-lived heavy uranium fragments produced at 1000 MeV/u. *Eur. Phys. Lett.*, 104:42001, 2013.

S. Purushothaman, S. Ayet San Andrés, J. Bergmann, T. Dickel, J. Ebert, H. Geissel, C. Hornung, W. R. Plaß, C. Rappold, C. Scheidenberger, Y. K. Tanaka, and M. I. Yavor. Hyper-EMG: A new probability distribution function composed of exponentially modified gaussian distributions to analyze asymmetric peak shapes in high-resolution time-of-flight mass spectrometry. *Int. J. Mass Spectrom.*, 421:245–254, 2017.

R Core Team. *R: A Language and Environment for Statistical Computing*. R Foundation for Statistical Computing, Vienna, Austria, 2021. URL `https://www.R-project.org/`.

Sebastian Raeder, Henning Heggen, Jens Lassen, Friedhelm Ames, Daryl Bishop, Pierre Bricault, Peter Kunz, Anders Mjøs, and Andrea Teigelhöfer.

An ion guide laser ion source for isobar-suppressed rare isotope beams. *Rev. Sci. Instrum.*, 85:033309, 2014.

M. Ranjan, S. Purushothaman, T. Dickel, H. Geissel, W. R. Plaß, D. Schäfer, C. Scheidenberger, J. Van de Walle, H. Weick, and P. Dendooven. New stopping cell capabilities: RF carpet performance at high gas density and cryogenic operation. *Eur. Phys. Lett.*, 96:52001, 2011.

M. P. Reiter. *Pilot Experiments with Relativistic Uranium Projectile and Fission Fragments Thermalized in a Cryogenic Gas-Filled Stopping Cell.* PhD thesis, Justus Liebig University Gießen, 2015.

M. P. Reiter, S. Ayet San Andrés, E. Dunling, B. Kootte, E. Leistenschneider, C. Andreoiu, C. Babcock, B. R. Barquest, J. Bollig, T. Brunner, I. Dillmann, A. Finlay, G. Gwinner, L. Graham, J. D. Holt, C. Hornung, C. Jesch, R. Klawitter, Y. Lan, D. Lascar, J. E. McKay, S. F. Paul, R. Steinbrügge, R. Thompson, J. L. Tracy, M. E. Wieser, C. Will, T. Dickel, W. R. Plaß, C. Scheidenberger, A. A. Kwiatkowski, and J. Dilling. Quenching of the N=32 neutron shell closure studied via precision mass measurements of neutron-rich vanadium isotopes. *Phys. Rev. C*, 98:024310, 2018.

M. P. Reiter, F. Ames, C. Andreoiu, S. Ayet San Andrés, C. Babcock, B. R. Barquest, J. Bergmann, J. Bollig, T. Brunner, T. Dickel, J. Dilling, I. Dillmann, E. Dunling, A. Finlay, G. Gwinner, C. Hornung L. Graham, B. Kootte, R. Klawitter, P. Kunz, Y. Lan, D. Lascar, J. Lassen, E. Leistenschneider, R. Li, J. E. McKay, M. Mostamand, S. F. Paul, W.R. Plaß, C. Scheidenbergera, B. E. Schultz, R. Steinbrügge, A. Teigelhoefer, R. Thompson, M.E. Wieser, C. Will, and A. A. Kwiatkowski. Improved beam diagnostics and optimization at ISAC via TITAN's MR-TOF-MS. *Nucl. Instrum. Methods B*, 463:431–436, 2020.

K. Riisager. Nuclear halo states. *Rev. Mod. Phys.*, 66:1105–1116, Jul 1994. doi: 10.1103/RevModPhys.66.1105. URL `https://link.aps.org/doi/10.1103/RevModPhys.66.1105`.

M. Rosenbusch, P. Ascher, D. Atanasov, C. Barbieri, D. Beck, K. Blaum, Ch. Borgmann, M. Breitenfeldt, R. B. Cakirli, A. Cipollone, S. George, F. Herfurth, M. Kowalska, S. Kreim, D. Lunney, V. Manea, P. Navrátil, D. Neidherr, L. Schweikhard, V. Somà, J. Stanja, F. Wienholtz, R. N. Wolf, and K. Zuber. Probing the $N = 32$ shell closure below the magic proton number $Z = 20$: Mass measurements of the exotic isotopes ^{52,53}K. *Phys. Rev. Lett.*, 114:202501, May 2015. doi: 10.1103/PhysRevLett.114.202501. URL `https://link.aps.org/doi/10.1103/PhysRevLett.114.202501`.

F. Sarazin, H. Savajols, W. Mittig, F. Nowacki, N. A. Orr, Z. Ren, P. Roussel-Chomaz, G. Auger, D. Baiborodin, A. V. Belozyorov, C. Borcea, E. Caurier, Z. Dlouhý, A. Gillibert, A. S. Lalleman, M. Lewitowicz, S. M. Lukyanov, F. de Oliveira, Y. E. Penionzhkevich, D. Ridikas, H. Sakuraï, O. Tarasov, and A. de Vismes. Shape coexistence and the $N = 28$ shell closure far from stability. *Phys. Rev. Lett.*, 84:5062–5065, May 2000. doi: 10.1103/PhysRevLett.84.5062. URL `https://link.aps.org/doi/10.1103/PhysRevLett.84.5062`.

G. Savard, St. Becker, G. Bollen, H. J. Kluge, R. B. Moore, Th. Otto, L. Schweikhard, H. Stolzenberg, and U. Wiess. A new cooling technique for heavy ions in a Penning trap. *Phys. Lett. A*, 158(5):247–252, 1991.

C. Scheidenberger. The contribution of precision mass measurements to nuclear physics. *Nucl. Phys. A*, 751:209–225, 2005.

O. Sorlin and M.-G. Porquet. Nuclear magic numbers: New features far from stability. *Prog. Part. Nucl. Phys.*, 61(2):602–673, 2008.

A.N. State, S. Beck, D. Amanbayev, D.L. Balabanski, H. Brand, P. Constantin, T. Dickel, C. Hornung, D. Nichita, W.R. Plaß, H. Roesch, A. Rotaru, C. Scheidenberger, J. Siebring, A. Spataru, N. Tortorelli, and J. Zhao. The slow control system of the frs ion catcher, 2022. ISSN 0168-9002. URL `https://www.sciencedirect.com/science/article/pii/S0168900222002844`.

Markus Steck and Yuri A. Litvinov. Heavy-ion storage rings and their use in precision experiments with highly charged ions. *Progress in Particle and Nuclear Physics*, 115:103811, 2020. ISSN 0146-6410. doi: https://doi.org/10.1016/j.ppnp.2020.103811. URL `https://www.sciencedirect.com/science/article/pii/S0146641020300582`.

D. Steppenbeck, S. Takeuchi, N. Aoi, P. Doornenbal, M. Matsushita, H. Wang, H. Baba, N. Fukuda, S. Go, M. Honma, J. Lee, K. Matsui, S. Michimasa, T. Motobayashi, D. Nishimura, T. Otsuka, H. Sakurai, Y. Shiga, P.-A. Söderström, T. Sumikama, H. Suzuki, R. Taniuchi, Y. Utsuno, J. J. Valiente-Dobón, and K. Yoneda. Evidence for a new nuclear 'magic number' from the level structure of ^{54}Ca. *Nature*, 502(7470):207, 2013.

D. Stresau and K. L. Hunter. Detailed performance characteristics of a new discrete dynode tof detector. 1999. URL `https://www.etp-ms.com/file-repository/19`.

V.M. Strutinsky. Shell effects in nuclear masses and deformation energies. *Nuclear Physics A*, 95(2):420–442, 1967. ISSN 0375-9474. doi: https://doi.org/

10.1016/0375-9474(67)90510-6. URL https://www.sciencedirect.com/science/article/pii/0375947467905106.

C. Thibault, R. Klapisch, C. Rigaud, A. M. Poskanzer, R. Prieels, L. Lessard, and W. Reisdorf. Direct measurement of the masses of ^{11}Li and $^{26-32}$Na with an on-line mass spectrometer. *Phys. Rev. C*, 12:644–657, Aug 1975. doi: 10.1103/PhysRevC.12.644. URL https://link.aps.org/doi/10.1103/PhysRevC.12.644.

C. Thibault, F. Touchard, S. Büttgenbach, R. Klapisch, M. de Saint Simon, H. T. Duong, P. Jacquinot, P. Juncar, S. Liberman, P. Pillet, J. Pinard, J. L. Vialle, A. Pesnelle, and G. Huber. Hyperfine structure and isotope shift of the D_2 line of $^{76-98}$Rb and some of their isomers. *Phys. Rev. C*, 23:2720–2729, Jun 1981. doi: 10.1103/PhysRevC.23.2720. URL https://link.aps.org/doi/10.1103/PhysRevC.23.2720.

M. Thoennessen. 2022 update of the discoveries of nuclides. *International Journal of Modern Physics E*, 32(01):2330001, 2023. doi: 10.1142/S0218301323300011. URL https://doi.org/10.1142/S0218301323300011.

Y. Toker, N. Altstein, O. Aviv M. L. Rappaport, O. Heber, D. Schwalm, D. Strasser, and D. Zajfman. The kick-out mass selection technique for ions stored in an electrostatic ion beam trap. *J. Instrum.*, 4:P09001, 2009.

K. S. Toth, Y. A. Ellis-Akovali, F. T. Avignone, R. S. Moore, D. M. Moltz, J. M. Nitschke, P. A. Wilmarth, P. K. Lemmertz, D. C. Sousa, and A. L. Goodman. Single-particle states in ^{149}Er and ^{149}Ho, and the effect of the Z=64 closure. *Phys. Rev. C*, 32:342–345, 1985.

K.S. Toth, Y.A. Ellis-Akovali, J.M. Nitschke, P.A. Wilmarth, P.K. Lemmertz, D.M. Moltz, and F.T. Avignone. Structure in β-delayed proton spectra of N=81 precursors. *Physics Letters B*, 178(2):150–154, 1986. ISSN 0370-2693. doi: https://doi.org/10.1016/0370-2693(86)91486-3. URL https://www.sciencedirect.com/science/article/pii/0370269386914863.

C. F. von Weizäcker. Zur Theorie der Kernmassen. *Z. Phys.*, 96:431, 1935.

M. Wang, G. Audi, F. G. Kondev, W. J. Huang, S. Naimi, and Xing Xu. The AME2016 atomic mass evaluation (II). Tables, graphs and references. *Chin. Phys. C*, 41(3):030003, 2017.

Meng Wang, W.J. Huang, F.G. Kondev, G. Audi, and S. Naimi. The AME 2020 atomic mass evaluation (II). tables, graphs and references*. *Chin. Phys.*

C, 45(3):030003, mar 2021. doi: 10.1088/1674-1137/abddaf. URL `https://doi.org/10.1088/1674-1137/abddaf`.

Hadley Wickham, Mara Averick, Jennifer Bryan, Winston Chang, Lucy D'Agostino McGowan, Romain François, Garrett Grolemund, Alex Hayes, Lionel Henry, Jim Hester, Max Kuhn, Thomas Lin Pedersen, Evan Miller, Stephan Milton Bache, Kirill Müller, Jeroen Ooms, David Robinson, Dana Paige Seidel, Vitalie Spinu, Kohske Takahashi, Davis Vaughan, Claus Wilke, Kara Woo, and Hiroaki Yutani. Welcome to the tidyverse. *Journal of Open Source Software*, 4(43):1686, 2019. doi: 10.21105/joss.01686.

F. Wienholtz, D. Beck, K. Blaum, Ch. Borgmann, M. Breitenfeldt, R. B. Cakirli, S. George, F. Herfurth, J. D. Holt, M. Kowalska, S. Kreim, D. Lunney, V. Manea, J. Menéndez, D. Neidherr, M. Rosenbusch, L. Schweikhard, J. Simonis, J. Stanja, R.N. Wolf, and K. Zuber. Masses of exotic calcium isotopes pin down nuclear forces. *Nature*, 498:346, 2013.

F. Wienholtz, S. Kreim, M. Rosenbusch, L. Schweikhard, and R.N. Wolf. Mass-selective ion ejection from multi-reflection time-of-flight devices via a pulsed in-trap lift. *Int. J. Mass Spectrom.*, 421:285–293, 10 2017.

C. Will. *TITAN's Multiple-Reflection Time-of-Flight Mass Spectrometer and Isobar Separator – Characterization and First Experiments*. Bachelor thesis, Justus Liebig University Gießen, 2017.

C. Will. *Achieving One Million Mass Resolving Power with a Multiple-Reflection Time-of-Flight Mass Spectrometer*. Master thesis, Justus Liebig University Gießen, 2019.

R. N. Wolf, D. Beck, K. Blaum, Ch. Böhm, Ch. Borgmann, M. Breitenfeldt, N. Chamel, S. Goriely, F. Herfurth, M. Kowalska, *et al.* Plumbing neutron stars to new depth with the binding energy of the exotic nuclide ^{82}Zn. *Phys. Rev. Lett.*, 110:041101, 2013a.

R.N. Wolf, F. Wienholtz, D. Atanasov, D. Beck, K. Blaum, Ch. Borgmann, F. Herfurth, M. Kowalska, S. Kreim, Yu. A. Litvinov, D. Lunney, V. Manea, D. Neidherr, M. Rosenbusch, L. Schweikhard, J. Stanja, and K. Zuber. ISOLTRAP's multi-reflection time-of-flight mass separator/spectrometer. *Int. J. Mass Spectrom.*, 349-350:123–133, 2013b.

H. Wollnik and K. Becker. Ion optical design for an on-line mass separator with low cross contamination and the capability of good mass resolution. *Nucl. Instrum. Methods A*, 238:206–214, 1985.

H. Wollnik and M. Przewloka. Time-of-flight mass spectrometers with multiply reflected ion trajectories. *Int. J. Mass Spectrom. Ion Processes*, 96:267–274, 1990.

R. L. Workman *et al.* Review of Particle Physics. *PTEP*, 2022:083C01, 2022. doi: 10.1093/ptep/ptac097.

Xing Xu, Meng Wang, Yu-Hu Zhang, Hu-Shan Xu, Peng Shuai, Xiao-Lin Tu, Yuri A. Litvinov, Xiao-Hong Zhou, Bao-Hua Sun, You-Jin Yuan, Jia-Wen Xia, Jian-Cheng Yang, Klaus Blaum, Rui-Jiu Chen, Xiang-Cheng Chen, Chao-Yi Fu, Zhuang Ge, Zheng-Guo Hu, Wen-Jia Huang, Da-Wei Liu, Yi-Hua Lam, Xin-Wen Ma, Rui-Shi Mao, T. Uesaka, Guo-Qing Xiao, Yuan-Ming Xing, T. Yamaguchi, Y. Yamaguchi, Qi Zeng, Xin-Liang Yan, Hong-Wei Zhao, Tie-Cheng Zhao, Wei Zhang, and Wen-Long Zhan. Direct mass measurements of neutron-rich 86-Kr projectile fragments and the persistence of neutron magic number $N = 32$ in Sc isotopes. *Chinese Physics C*, 39(10):104001, oct 2015. doi: 10.1088/1674-1137/39/10/104001. URL `https://doi.org/10.1088/1674-1137/39/10/104001`.

M. I. Yavor. Using TOF shifts due to a quadrupolar field at the center of the analyzer for beam alignment. (private communication), 2016.

M. I. Yavor, W. R. Plaß, T. Dickel, H. Geissel, and C. Scheidenberger. Ion-optical design of a high-performance multiple-reflection time-of-flight mass spectrometer and isobar separator. *Int. J. Mass Spectrom.*, 381-382:1–9, 2015.

N. Zeldes, T.S. Dumitrescu, and H.S. Köhler. Mutual support of magicities and residual effective interactions near 208Pb. *Nuclear Physics A*, 399(1): 11–50, 1983. ISSN 0375-9474. doi: https://doi.org/10.1016/0375-9474(83)90592-4. URL `https://www.sciencedirect.com/science/article/pii/0375947483905924`.

Danksagung

Diese Arbeit wäre nicht ohne die Hilfe zahlreicher Menschen entstanden.

Ich danke Prof. Dr. Christoph Scheidenberger und Prof. Dr. Dr. h. c. Hans Geissel für die Möglichkeit zu promovieren und konstruktive Gespräche und Anregungen bezüglich meiner Arbeit und wissenschaftliche Diskussionen auch über weiterführende und verknüpfte Themen.

Bei Dr. Timo Dickel bedanke ich mich für wissenschaftliche Gespräche, zahlreiche wertvolle Anregungen, das Teilen seines großen Fundus an Erfahrung in experimenteller Physik und Ionenoptik und generelle Betreuung und Unterstützung im Arbeits- und Laboralltag. Dr. Wolfgang R. Plaß war mir eine große Hilfe beim präzisen Formulieren wissenschaftlicher Ergebnisse in Wort und Bild. Viel Dank geht auch an Dr. Moritz Pascal Reiter, für die Erfahrung am TITAN Experiment und Diskussionen über die wissenschaftlichen Ergebnisse und Methoden. Bei Prof. Dr. Jerzy Dudek und Dr. Irene Dedes bedanke ich mich für die Gespräche zur Modellierung von Kernen.

Für die Hilfe bei der neuen Kontrollsoftware für den FRS Ion Catcher bedanke ich mich bei Holger Brandt, Alexandru State und Heidi Roesch. Bei den technischen Verbesserungen am FRS Ion Catcher und beim Testen der Strahlausrichtung konnte ich auf Unterstützung von Markus Kielmann, Adrian Rotaru, Gabriella Kripkó-Koncz, Christian Will, Dr. Christine Hornung und Thomas Wasem und die feinmechanische Werkstatt des Fachbereichs 07 der Justus-Liebig-Universität Gießen zurückgreifen.

Bei den Mitgliedern der TITAN Kollaboration bedanke ich mich für die Vorbereitung vor Ort, das offenherzige Willkommen und die gute Zusammenarbeit. Prof. Dr. A. A. Kwiatkowski, Dr. Moritz Pascal Reiter, Eleni Marina Lykiardopoulou, Brian Kootte, Andrew Jacobs danke ich auch für Diskussionen rund um die Auswertung der Daten.

Ganz allgemein bedanke ich mich bei den Mitgliedern der IONAS Gruppe und der FRS und FRS Ion Catcher Kollaborationen an der GSI Darmstadt für die gute Zusammenarbeit in allen Aspekten der täglichen Arbeit und des menschlichen Miteinanders.

Zu guter Letzt danke ich Familie und Freunden, für deren tatkräftige und vielfältige Unterstützung.

Appendix

Appendix A

Technical Details of the FRS-IC Slow Control System

The FRS ion catcher control (FRSICC) software is developed such that basic maintenance and extension can be done by a non-expert, though some LabVIEW experience is needed. The main properties to achieve this are the modularization and the configuration via a simple text file and inside easily accessible and extendable parts of LabVIEW VIs. The following should guide maintenance and extension in a not completely general way (which would be out of scope here), with the help of the examples of exchanging an MKS974B gauge and of adding another high precision power supply (HiPPS actor). Where VI names are given, they are given with library and class name in the structure as in the LabVIEW project, but not with the full path due to its excessive length. The `FRSICC_Launcher.lvlib` should be in `FRSICC/Control` and `FRSICC_MainGUI.lvlib` should be in `FRSICC/GUI`.

Generally if a device is replaced by the same type and the hardware address changes, this has to be complemented by a change in the text file only, see Fig. A.2. What can be configured in the text file depends on the actor implementation and its inheritance. Often the actor inherits from the CSPP base actor, then among other properties the polling time (the interval at which the device is periodically read out) can be configured in the text file, see Fig. A.2. If a new instance of an existing device is added, the corresponding section of the configuration file needs to be duplicated and at minimum name and hardware be adapted for the new device. In the sections `[StartActor.ActorList]` and `[Client.ActorList]`, lines with the new actor name have to be added. Then for automatically launching the actor for the new device, the `[FRSICCLauncher]` section of the configuration file has to be extended by duplicating and adapting the appropriate line, *e. g.*

```
FRSICC_Launcher:FRSICC_Launcher.HiPPS6="HiPPS6,1"
                                ↓
FRSICC_Launcher:FRSICC_Launcher.HiPPS6="HiPPS6,1"
FRSICC_Launcher:FRSICC_Launcher.HiPPS7="HiPPS7,1"
```

and the new name (here HiPPS7) has to be added in an text array in the file `FRSICC_Launcher.lvlib/FRSICC_Launcher.lvclass/Private/Initialize Attibute - Nested Actors.vi`, see Fig. A.1. Furthermore, if the actor should be relaunched upon stopping, its name needs to be added to the "relaunch actors" case in `FRSICC_Launcher.lvlib/FRSICC_Launcher.lvclass/Override/Handle Last Ack Core.vi`. The number of automatic relaunches is the one given after the actor name separated with a comma, in the above example `"HiPPS6,1"` it is one. Equivalent steps have to be taken for adding entirely new devices, only

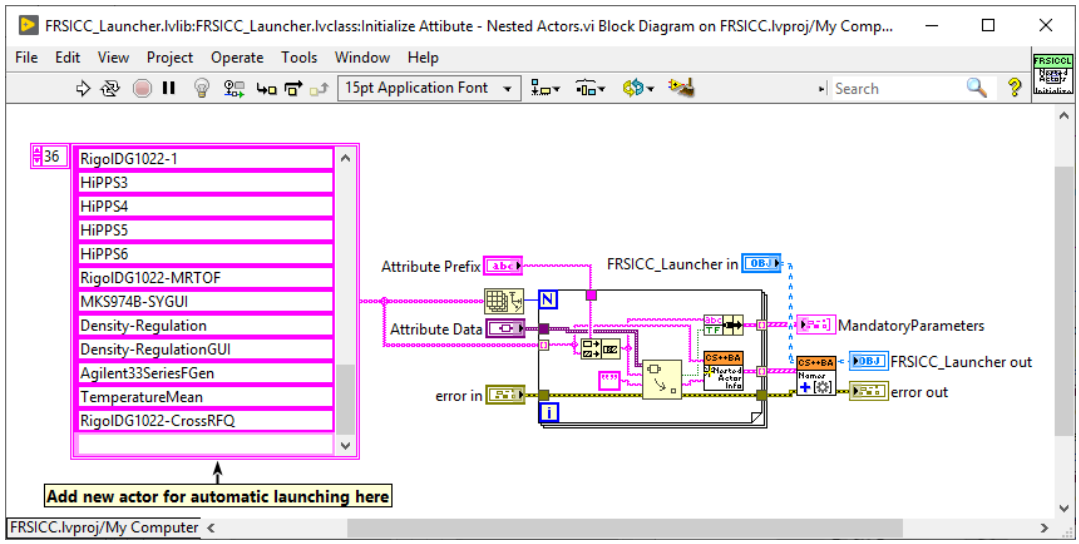

Figure A.1: Block diagram of `Initialize Attibute - Nested Actors.vi`. The text array which needs to be extended when another actor is added for automatic starting is on the left.

then a formerly not used actor has to be copied (if existing) or implemented and its configuration put into the text file.

For adding controls and readouts to the main GUI, more lines need to be added in the configuration file and more VIs need to be edited. As for the launcher, *e. g.*

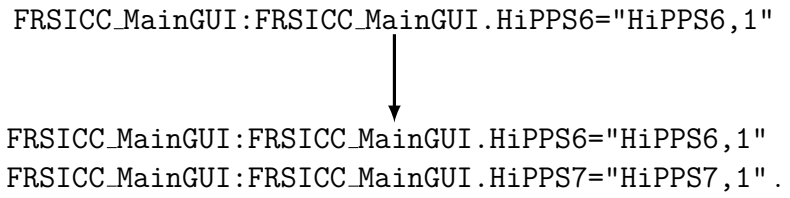

In case of the main GUI, actor name, enqueuer and actor proxy (that means a string constant, an enqueuer constant and another string constant, all with names matching the corresponding names in the configuration file) have to be added to the class private data
`FRSICC_MainGUI.lvlib/FRSICC_MainGUI.ctl`.
Then actor and proxy can be added as new bundle elements and bundled into the array in
`FRSICC_MainGUI.lvlib/FRSICC_MainGUI.lvclass/Private/FRSICC_BundleElements.vi`.
Similarly, array alements have to be added, bundled and wired in
`FRSICC_MainGUI.lvlib/FRSICC_MainGUI.lvclass/Override/FRSICC_Initialize Attributes Core.vi`.
For the `Actor Core.vi` of the main GUI, no universal recipe exists, but one can use the already existing devices as examples. In general, first the process variables (PVs) have to be registered and then possible interaction can be programmed in an event structure, see fig. A.3. This structure covers updates of the actors PVs and user input. If an existing devices is to be duplicated, also the LabVIEW code can be duplicated. For some devices this is made easier by using dedicated VIs for initialization [*e. g.* Fig. A.4] and furthermore controls belonging to one device are gathered in tabs on the main GUI front panel for simple duplication.

```
[MKS974B-MRTOF-top]
LVClassPath="CSPP_MKS974B.lvlib:CSPP_MKS974B.lvclass"
# Settings:  "Ignore", "Auto", "User"
CSPP_BaseActor:CSPP_BaseActor.Settings="Ignore"
CSPP_BaseActor:CSPP_BaseActor.DefaultGUI=
        "CSPP_MKS974B_GUI.lvlib:CSPP_MKS974B_GUI.
        lvclass"
CSPP_BaseActor:CSPP_BaseActor.LaunchDefaultGUI=False
CSPP_BaseActor:CSPP_BaseActor.ErrorDialog=False
CSPP_BaseActor:CSPP_BaseActor.PollingInterval_s=1.
CSPP_BaseActor:CSPP_BaseActor.PVProxy=
        "MKS974B-MRTOF-topProxy"
CSPP_BaseActor:CSPP_BaseActor.LaunchPVProxy=True
CSPP_DeviceActor:CSPP_DeviceActor.ResourceName=
        "FRSIC-MRTOF-974B-top"
CSPP_DeviceActor:CSPP_DeviceActor.Reset=False
CSPP_DeviceActor:CSPP_DeviceActor.Selftest=False
CSPP_DeviceActor:CSPP_DeviceActor.OptionString=
        "Simulate=0,RangeCheck=1,
        QueryInstrStatus=0,Cache=1"
CSPP_DeviceActor:CSPP_DeviceActor.
        ResetWithDefaults=False
CSPP_MKS974B:CSPP_MKS974B.Address=253
# Serial Parameter explanation:
CSPP_MKS974B:CSPP_MKS974B.Serial=
        "9600,None,8,1.0,None"
CSPP_MKS974B:CSPP_MKS974B.MeasurementMode=3
```

Figure A.2: A part of the FRSICC initialization text file for configuring a MKS 974b widerange gauge. Comments start with a hashtag (`# Comment`), sections for actors are enclosed in brackets (`[Actor]`). Actors and their properties in the project are referred to in the format `Library:Class.Property`. For example, in the first blue line the class of the actor configured in this section is given as `CSPP_MKS974B.lvlib:CSPP_MKS974B.lvclass` and in the second blue line the `PollingInterval_s` property of the CSPP base actor —from which the MKS974B actor inherits— is set to `1`, *i. e.* the actor is set to read the device every second. The additionally blue highlighted lines shows parts which would need to be updated if the hardware address changes.

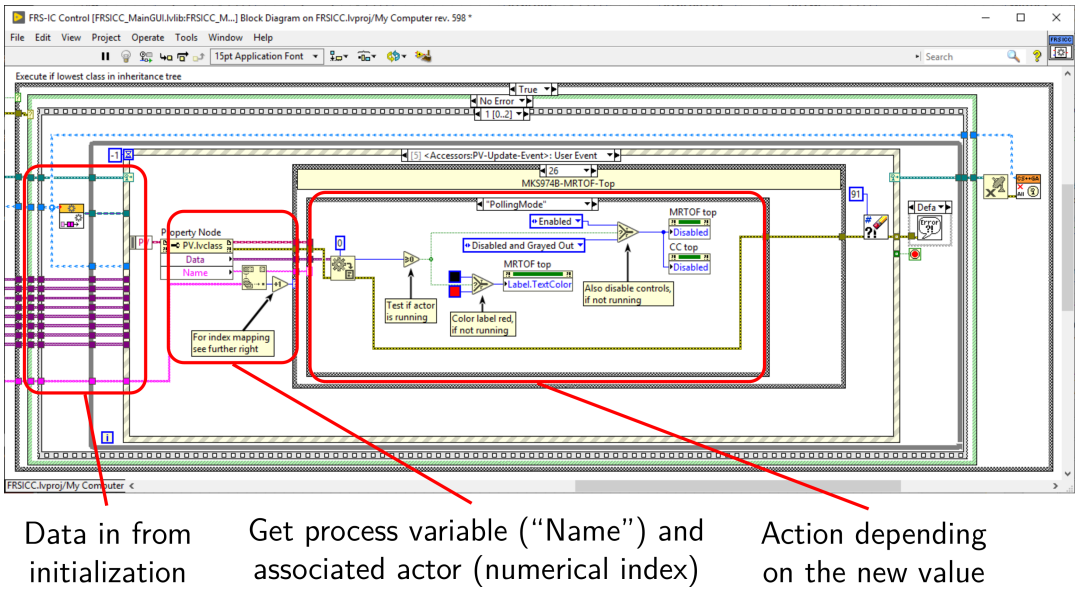

Figure A.3: A part of the main GUI LabVIEW block diagram, showing processing of user inputs and changes caused by other actors. Not shown on the left is the initialization part, an example subVI is given in Fig. A.4. The event structure triggers on changes in main GUI inputs or from other actors, here shown is the event where the "PollingMode" process variable of one pressure transducer is updated. Its value is used to test if the respective device actor is running ("PollingMode"≥ 0). If it is not running, some controls get disabled and the actor label is rendered in red on the main GUI to notify the operator.

Figure A.4: Block diagram of the main GUI initialization of the HiPPS actors. If another HiPPS is added, the two clusters need to be extended after adapting the textfile and another subVI, then the respective parts in the main GUI block diagram can be copied to be able to control the added devices from there.

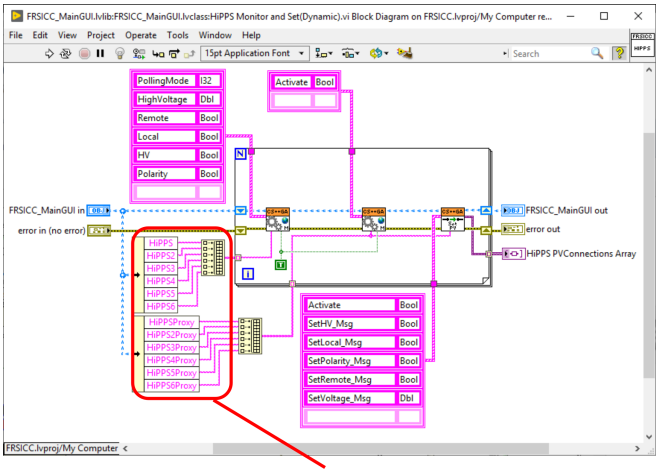

Appendix B

Quadrupolar Lens at the MRS: TOF Shift Model, Simulations and Experimental Data

Here the approach to probe the beam position inside the analyzer by observing the time-of-flight (TOF) shift due to the quadrupolar lens is presented including simulations and initial analysis of the available experimental data. This approach is an alternative to observing changes in the count rates. Since the count rate changes depend on deflecting the beam to electrode surfaces or apertures, they can be unaffected by the quadrupole potential in a broad range and observing the TOF shift should be more accurate. Moreover, edges on different sides of the transmission plateau can be due to different electrode surfaces or apertures, thus also the determination of these edges can introduce systematic deviations from the actual optimum of the steering voltages.

Model and Simulations

For a quantitative treatment of the TOF shift introduced by a quadrupolar field at the MRS, assume that the potential along the optical axis z has sharp steps up and down at the planes corresponding to the beginning and end of the MRS electrodes, respectively. The potential change will change the velocity $v_0 \to v_1$ according to the coordinates (x_0, y_0) where the beam enters the quadrupolar potential, but not the direction. Index numbers $0, 1$ and 2 refer to immediately before entering the quadrupole, inside the quadrupole and immediately after leaving it. Thus the velocity components are all changed by the same factor $\sqrt{K_1/K_0}$. The velocity component parallel to the optical axis $v_{1;z}$ remains constant while traversing the quadrupolar field.

The potential of an ideal quadrupole field generated by hyperbolic electrodes is

$$V(x,z) = V_{\mathrm{qp}}^{0}(x^2 - y^2)\,, \tag{B.1}$$

where the foci of the hyperbolic electrodes are located on the $y = 0$ and $x = 0$ lines. The constant V_{qp}^{0} defines the strength of the potential. Other electrode shapes lead to deviation from the ideal quadrupole field, which can still be used as low order approximation for the central part around $(x, y) = (0, 0)$. To estimate the magnitude of the TOF shift, SIMION simulations where performed to get the position change *vs* trap system steerer voltage in one dimension and the value of V_{qp}^{0} *vs* the applied quadrupolar voltage. This resulted in

$$x_0 = 0.035\,\mathrm{mm\,V^{-1}} \cdot V_{\mathrm{steer}} \tag{B.2}$$

$$V_{\mathrm{qp}}^{0} = 0.016 \cdot V_{\mathrm{applied}}\,. \tag{B.3}$$

For an estimate of the TOF shift caused by the different potential only, consider a steering voltage difference of 50 V. Then a position difference of 1.75 mm is expected. With an applied voltage at the MRS electrodes of ±60 V, this corresponds to a potential difference of about 3 V between a central hit and an offset in the direction of the steepest gradient ($y = 0$ or $x = 0$). With the approximations $v_{0;z} \approx v_0$ and $v_{1;z} \approx v_1$, the TOF shift is

$$\Delta\mathrm{TOF}_{\mathrm{MRS}} \approx \frac{l_{\mathrm{MRS}}}{v_0} - \frac{l_{\mathrm{MRS}}}{v_1} \tag{B.4}$$

with the length of the MRS $l_{\mathrm{MRS}} = 8\,\mathrm{mm}$ and

$$v_i = \sqrt{\frac{2K_i}{m}}\,. \tag{B.5}$$

Employing $K_0 = 1300\,\mathrm{eV}$, $K_1 = 1303\,\mathrm{eV}$ and the mass $m = 133\,\mathrm{u}$, this yields the TOF shift $\Delta\mathrm{TOF}_{\mathrm{MRS}} \approx 0.2\,\mathrm{ns}$, which is about a factor 20 lower than expected from the fit to the experimental data obtained with ^{133}Cs (see below).

SIMION simulations for different steering voltages have been carried out to compare with the experimental data and the above considerations. They confirm that the TOF shift due to the potential difference at the MRS plane is not dominant and they also show a rotated quadrupole pattern, see Fig. B.1. Furthermore, the mean MRS-only TOF shift around steering voltages ($\pm 35\,\mathrm{V}, \mp 35\,\mathrm{V}$) (this corresponds to 50 V steering in the direction of the steepest gradient of the quadrupolar potential, as used for the earlier calculation) is 0.3 ns in good agreement with the above estimate.

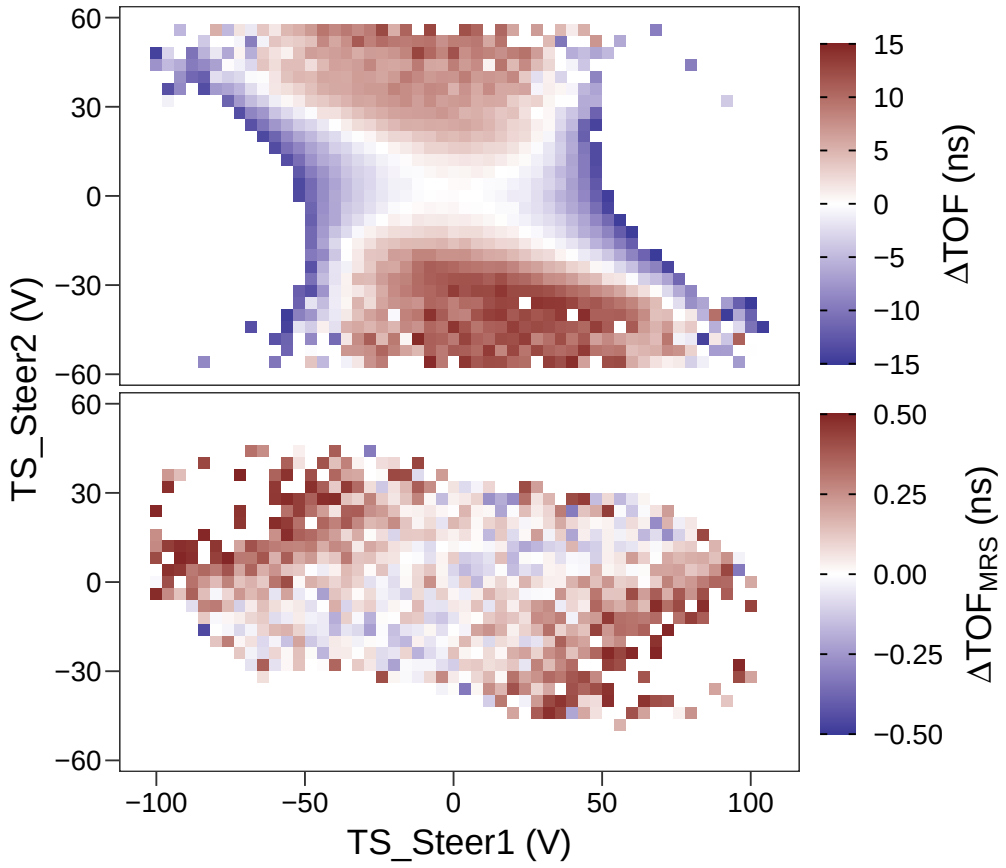

Figure B.1: Evaluated TS steerer scans from SIMION simulations. Top panel: Total TOF shift (ΔTOF). Bottom panel: TOF shift accumulated when traversing the MRS ($\Delta\text{TOF}_{\text{MRS}}$). It can be observed that $\Delta\text{TOF}_{\text{MRS}}$ shows the expected symmetry due to the rotation of the MRS electrodes compared to the TS steerer electrodes, that it is not the dominant contribution to the total TOF shift, and that the rotation of the quadrupole pattern seen in the total TOF shift is different than that of $\Delta\text{TOF}_{\text{MRS}}$.

First Analysis of Experimental Data

With the experimental data, the TOF shift method was first not applied since its dependence *vs* the TS steerer voltages does not directly reveal the expected quadrupole pattern, but a dominantly linear dependence [top panel in Fig. B.2]. However, a more detailed look at the residuals of a linear fit showed the expected characteristics and motivated the fit of a combined function. The positions x', y' depend linearly on the two steering voltages, thus the TOF shift was fitted with a function employing a phenomenological linear and a rotated quadrupole term,

$$f_{\text{lin.+qp}}(x,y) = \overbrace{a_0 + a_1(x-s_1) + a_2(y-s_2)}^{\text{linear part}} + \ldots \\ \underbrace{b\Big[\sin(\varphi)((x-s_1)^2 - (y-s_2)^2) - \cos(\varphi)\cdot 2(x-s_1)(y-s_2)\Big]}_{\text{rotated quadrupole part}} . \quad \text{(B.6)}$$

The fit of its parameters a_0, a_1, a_2, b, φ, s_1 and s_2 was performed using a Nelder-Mead optimization algorithm in R [Nelder and Mead, 1965; R Core Team, 2021] to minimize the sum of the squared residuals. The results are shown in Fig. B.2. When comparing the fit of $f_{\text{lin.+qp}}$ to ΔTOF with the fit of f_{WS} to Q (chapter 3), the center differs by 3 and 10 V for the two steering voltages, respectively.

The outcome of the analysis could not yet be tested as the system is undergoing repair. The origin of the dominating linear dependence is not yet understood.

As argued above, the observed quadrupolar potential pattern is not purely due to the TOF shift caused by the potential difference. This can be seen by observing that the MRS electrodes are rotated by 45° compared to the trap system steerer electrodes [Fig. 3.1], but the pattern is not. Furthermore, the magnitude of the observed shift is too large – about $\Delta\text{TOF} = 5\,\text{ns}$ at 50 V one-dimensional off-optimum steering with the other steerer centered, to be compared with the estimated $\Delta\text{TOF}_{\text{potential}} = 0.2\,\text{ns}$ [Appendix B]. On the other hand, the magnitude fits reasonably well to the simulation.

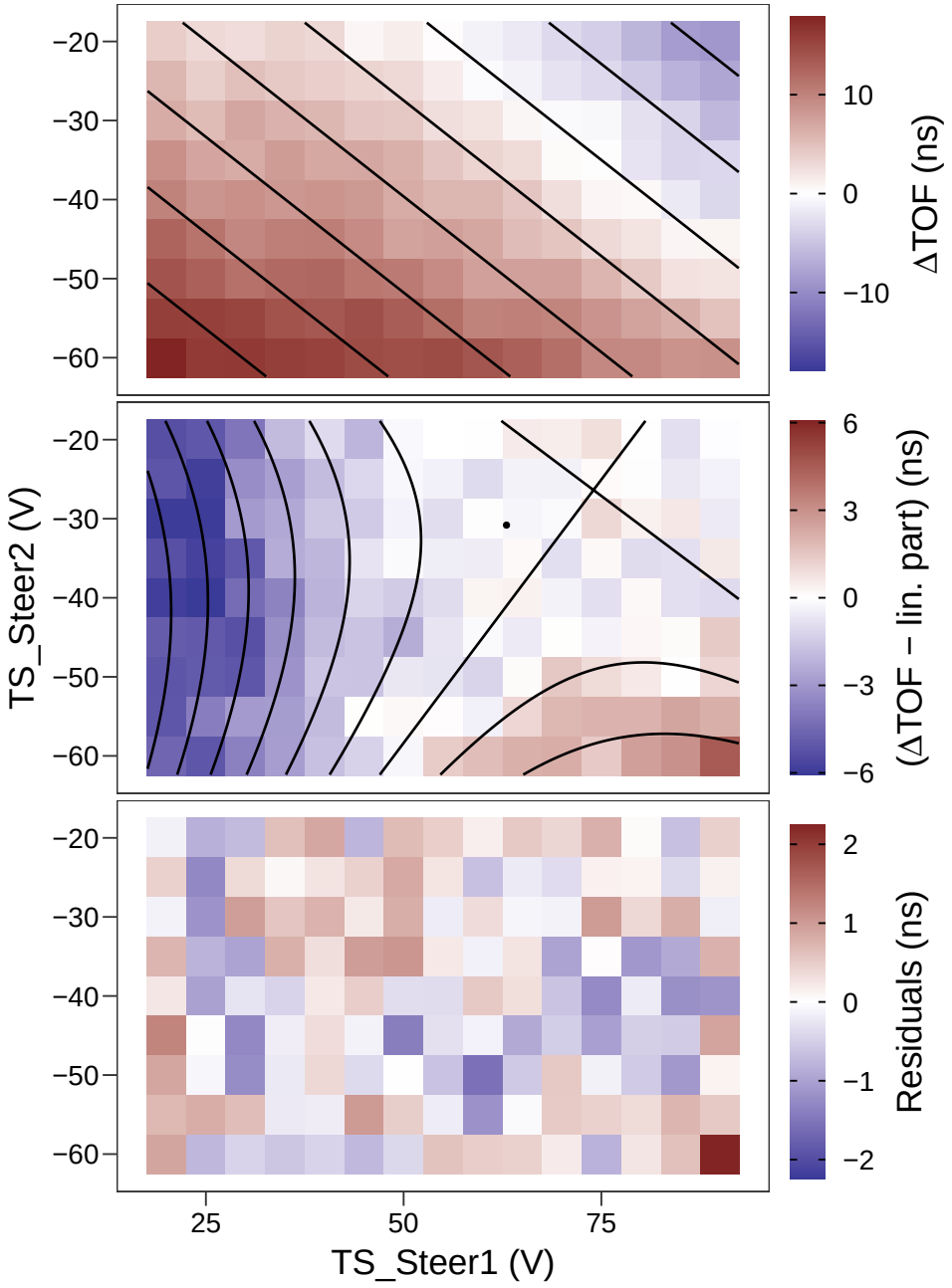

Figure B.2: TOF shift *vs* TS steerer voltages. The top panel shows the measured TOF shift and contour lines of the linear part of $f_{\text{lin.+qp}}$, eq. (B.6), after fitting the full function to the data. The middle panel shows the TOF shift with the fitted linear part subtracted and contour lines of the quadrupolar part of $f_{\text{lin.+qp}}$. The black dot indicates the optimum steerer voltages found with the merit function Q, *i. e.* using count rates. The bottom panel shows the residuals of the complete fit. Note that the color scales are adjusted per panel, as the effects have different magnitudes.

Appendix

Appendix C

MAc Data Recording and Subsequent Analysis

For the beam alignment, the new and improved voltage optimizer of the software MAc [Bergmann, thesis in preparation] was used. Up to three parameters were iterated in nested loops and parameters and observables (Counts, Peak position and width) were written to ASCII files. The files were read and brought into a format for easier handling in the software package R [R Core Team, 2021] using packages from the tidyverse [Wickham *et al.*, 2019]. Fits to model functions were performed using least squares minimization with the Levenberg-Marquard algorithm [Moré, 1978] in from the minpack.lm package [Elzhov *et al.*, 2016], or in the case of the "linear + rotated quadrupole" model $f_{\text{lin.+qp}}$ (eq. (B.6), Fig. B.2) least squares were minimized with the Nelder-Mead algorithm from base R after fitting the data first with a linear model and the residuals with a non-rotated quadrupole to obtain starting values. This was necessary since a direct fit using a Levenberg-Marquard algorithm resulted in errors.

The results of the analysis after sorting and combining the different measurement point were presented earlier, here the data is shown as seen by the user in MAc. Fig. C.1 shows the trap system steerer scan with turning the quadrupole potential on and off, this is the underlying data for figures 3.2 and B.2. Fig. C.2 shows the MRS steerer scan, this is the underlying data for Fig. 3.3.

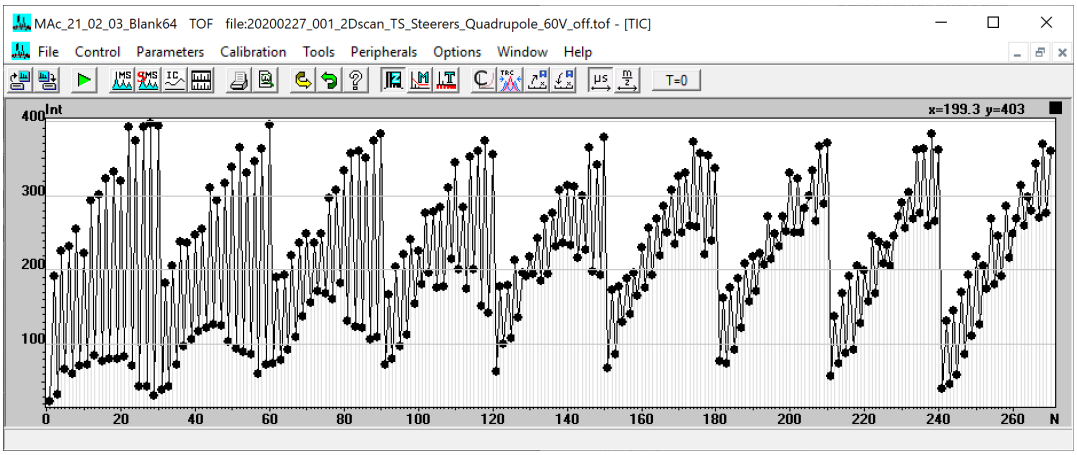

Figure C.1: Total ion count as recorded by MAc when iterating over both trap system steerers and the applied quadrupole voltage, the latter changing in the innermost loop between on and off. The difference between adjacent measurements is due to the effect of the quadrupole potential and one can see that there are regions where this is more and where this is less pronounced. The different blocks starting each 30 measurements are due to the change of the steering voltage in the middle loop, which was iterated over 30 equidistant values leading to the slowly varying counts. There are 9 such blocks due to the change of the second steering voltage in the outermost loop, iterated over 9 equidistant values and leading to the slow change of the pattern from block to block. There were in total 270 spectra acquired for 135 different combinations of steering voltages.

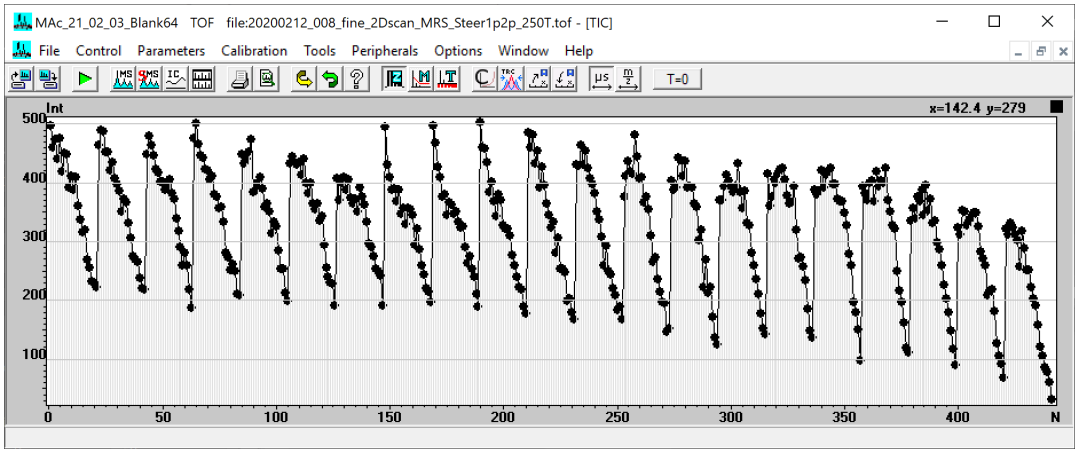

Figure C.2: Total ion count as recorded by MAc when iterating over both MRS steerers. The different blocks starting each 21 measurements are due to the change of the steering voltage in the inner loop, which was iterated over 21 equidistant values leading to the slowly varying counts. There are 21 such blocks due to the change of the second steering voltage in the outer loop, iterated over 21 equidistant values and leading to the slow change of the pattern from block to block. There were in total 441 spectra for different steering voltage combinations acquired.

Eigenständigkeitserklärung

Ich habe die vorgelegte Dissertation selbstständig und ohne unerlaubte fremde Hilfe und nur mit den Hilfen angefertigt, die ich in der Dissertation angegeben habe. Alle Textstellen, die wörtlich oder sinngemäß aus veröffentlichten Schriften entnommen sind, und alle Angaben, die auf mündlichen Auskünften beruhen, sind als solche kenntlich gemacht. Ich stimme einer evtl. Überprüfung meiner Dissertation durch eine Antiplagiat-Software zu. Bei den von mir durchgeführten und in der Dissertation erwähnten Untersuchungen habe ich die Grundsätze guter wissenschaftlicher Praxis, wie sie in der „Satzung der Justus-Liebig-Universität Gießen zur Sicherung guter wissenschaftlicher Praxis“ niedergelegt sind, eingehalten.

Darmstadt, 01. Juni 2023

Sönke Beck